Stratospheric aerosol extinction profile retrievals from SCIAMACHY limb-scatter observations

Florian Ernst

Universität Bremen

Stratospheric aerosol extinction profile retrievals from SCIAMACHY limb-scatter observations

Vom Fachbereich für Physik und Elektrotechnik
der Universität Bremen

zur Erlangung des akademischen Grades eines

Doktor der Naturwissenschaften (Dr. rer. nat.)

genehmigte Dissertation

von

Dipl. Met. Florian Ernst

aus Herne

1. Gutachter:	Prof. Dr. John P. Burrows
2. Gutachter:	Prof. Dr. Otto Schrems

Eingereicht am:	07.10.2013
Tag des Promotionskolloquiums:	26.11.2013

Abstract

This dissertation presents a method for retrieving stratospheric aerosol extinction profiles from a global satellite data set. Ten years of limb radiance measurements with the instrument SCanning Imaging Absorption spectroMeter for Atmospheric CHartographY (SCIAMACHY) onboard the European environmental research satellite Envisat provides the unique opportunity to derive a stratospheric aerosol extinction data set over a long time period (2002–2012) with a good global coverage on a daily basis.

Stratospheric aerosols have a significant impact on climate but the determination is still subject to large uncertainties. Consisting mainly of sulfuric acid droplets they directly influence the radiative balance of the earth, play an important role in cloud formation and interact with atmospheric chemistry, in particular with ozone. To improve our understanding of climate relevant processes an accurate determination of stratospheric aerosol properties is crucial. Solar occultation measurements traditionally used for the determination of stratospheric aerosol extinction profiles are very accurate, but limited in global coverage. The limb-scatter technique used in this work measures sunlight scattered by the Earth's atmosphere and combines a high vertical resolution with a near-global coverage on a daily basis.

Deriving stratospheric aerosol extinction from limb radiance spectra requires complicated radiative transfer calculations. In this work the sophisticated radiative transfer model and retrieval code SCIATRAN 3.1 is used to implement an algorithm based on a color-index approach combining normalized limb radiance spectra at 470 and 750 nm to retrieve aerosol extinction profiles between 12 and 35 km altitude. Detailed sensitivity studies are performed for the first version V1.0 of the retrieval

containing a Henyey-Greenstein approximation of the phase function. These sensitivity studies revealed that this simplification is not suitable for the retrieval of stratospheric aerosol extinction profiles from SCIAMACHY limb spectra. As a consequence, a Mie phase function for typical background aerosols is implemented in retrieval version V1.1. The sensitivity studies for this version showed that under typical atmospheric conditions the largest source for errors are uncertainties in the knowledge of neutral density and tropospheric clouds with errors of up to 15 % and 9 %, respectively, in the southern hemisphere. Other tested parameters are ground albedo (8 % error at most), a priori profile (7 %), tangent height registration (6 %), and ozone (<1 %).

Comparisons of the results of the retrieval versions V1.0 and V1.1 with co-located measurements of the solar occultation instrument SAGE II confirmed the findings of the sensitivity studies. While version V1.0 shows large interhemispheric differences and a bad agreement with both SAGE II data set versions used (V6.2 and V7.0), particularly in the southern hemisphere, the results of version V1.1 using the Mie phase function show very good globally averaged agreement with SAGE II V7.0 measurements within 10 % above 15 km. First results on the global morphology of stratospheric aerosols retrieved from SCIAMACHY with retrieval version V1.1 at three pressure levels are consistent with the current knowledge of stratospheric dynamics. The global aerosol extinction morphology at 70 hPa shows clear evidence for a stratospheric impact of multiple volcanic eruptions and a pyroconvective event between 2005 and 2011.

The SCIAMACHY stratospheric aerosol data set derived in this work is capable of reducing the uncertainties in the determination of climate relevant parameters and has the potential to be highly valuable as input data for global circulation models. It spans a period of time without volcanic disturbances form 2002–2005 as well as a volcanically highly active phase from 2005–2012 and can serve as a foundation for climatological interpretation with respect to both stratospheric background conditions and the volcanic impact.

Publications

Conference proceedings

Ernst, F., von Savigny, C., Rozanov, A., Rozanov, V., Bovensmann, H., and Burrows, J. P.: Retrieval of stratospheric aerosol distributions from SCIAMACHY limb measurements: first steps and methodology, Proceedings Atmospheric Science Conference, Barcelona, Spain, 7–11 September 2009, ESA Special Publication SP-676, 2009.

Conference contributions

Ernst, F., von Savigny, C., Rozanov, A., Rozanov, V., Eichmann, K.-U., Brinkhoff, L. A., Bovensmann, H., Burrows, J. P.: Global stratospheric aerosol extinction profile retrievals from SCIAMACHY limb radiance: algorithm description and validation, 7th International Atmospheric Limb Conference, 17–19 June 2013, Bremen, Germany, 2013.

Ernst, F., von Savigny, C., Rozanov, A., Rozanov, V., Eichmann, K.-U., Brinkhoff, L. A., Bovensmann, H., Burrows, J. P.: Stratospheric aerosol extinction profile retrievals from SCIAMACHY limb-scatter observations, 39th Scientific Assembly of the Committee on Space Research, 14–22 July 2012, Mysore, India, 2012.

Ernst, F., von Savigny, C., Rozanov, A., Rozanov, V., Bovensmann, H., Burrows, J. P.: Stratospheric aerosol extinction profile retrievals from SCIAMACHY limb-scatter observations, European Geoscience Union General Assembly, 22–27 April

2012, Vienna, Austria, 2012.

Ernst, F., von Savigny, C., Rozanov, A., Rozanov, V., Bovensmann, H., Burrows, J. P.: Retrieval of stratospheric aerosol distributions from SCIAMACHY limb measurements: methodology, sensitivity studies and results, European Geoscience Union General Assembly, 03–08 April 2011, Vienna, Austria, 2011.

Ernst, F., von Savigny, C., Rozanov, A., Rozanov, V., Bovensmann, H., Burrows, J. P.: Retrieval of stratospheric aerosol distributions from SCIAMACHY limb measurements: first steps, methodology and first results, 38th Assembly of the Committee on Space Research, 18–25 July 2010, Bremen, Germany, 2010.

Ernst, F., von Savigny, C., Rozanov, A., Rozanov, V., Bovensmann, H., Burrows, J. P.: Retrieval of stratospheric aerosol distributions from SCIAMACHY limb measurements: methodology, sensitivity studies and first results, European Geoscience Union General Assembly, 02–07 May 2010, Vienna, Austria, 2010.

Ernst, F., von Savigny, C., Rozanov, A., Rozanov, V., Bovensmann, H., Burrows, J. P.: Retrieval of stratospheric aerosol distributions from SCIAMACHY limb measurements: methodology and first results, DPG Spring Meeting of the Section AMOP and the Divisions Environmental Physics and Physics Education, 08–12 March 2010, Hanover, Germany, 2010.

Ernst, F., von Savigny, C., Rozanov, A., Rozanov, V., Bovensmann, H., Burrows, J. P.: Retrieval of stratospheric aerosol distributions from SCIAMACHY limb measurements: first steps and methodology, 5th Atmospheric Limb Conference, 16–19 November 2009, Helsinki, Finland, 2009.

Contents

Motivation and objectives

Stratospheric aerosols play an important role in the global climate system as they significantly influence the radiative balance of the Earth and interact in stratospheric chemistry. The thin haze consisting mainly of sulfate droplets scatters solar radiation and increases the planetary albedo indirectly by influencing the cloud formation in the upper troposphere. These effects combined lead to a cooling effect of different magnitude under undisturbed background conditions and periods of volcanically enhanced aerosol load, the two generally distinguishable stratospheric states with respect to aerosols.

The eruption of Mount Pinatubo in 1991 demonstrated impressively the cooling potential of stratospheric sulfate aerosols. The mean global temperature decreased by multiple tenths of a degree for several months after the eruption. But even if the cooling effect is smaller under non-volcanic conditions, it is not negligible.

The anthropogenic influence on stratospheric aerosols – which are an Essential Climate Variable according to the Global Climate Observing System (GCOS) – is very sparsely investigated and yet not well understood. It is expected that a future increase in anthropogenic emission of aerosol source gases like SO_2 will significantly reduce the man-made global warming effect caused by the emission of greenhouse gases, but the valuation of this dampening effect underlies large uncertainties (IPCC, 2007)

In this context, even intentional active human intervention in the Earth's climate system is considered: geoengineering by injection of sulfur compounds into the

stratosphere is a standard approach in solar radiation management (e.g., Crutzen, 2006).

Furthermore, stratospheric aerosols play an important role in stratospheric chemistry, especially ozone depletion, leading to an effect in an atmospheric parameter which is essential for human health and life on earth in general.

Continuous global observations of stratospheric aerosols are essential for monitoring the spatial distribution of volcanic aerosols with time as well as the long-term variation of stratospheric aerosols in general. These observations can only be provided by satellite measurements.

The observation technique traditionally used to measure stratospheric aerosol extinction profiles is solar occultation. Solar occultation observations provide accurate aerosol extinction profiles typically with high vertical resolution at multiple wavelengths, and the spectral dependence of the extinction coefficients allows inferring information on the aerosol particle size. The disadvantage of solar occultation measurements is that the number of occultations is limited to one sunrise and one sunset observation per orbit at most. Moreover, the latitudes of these observations change only slowly with time.

A new generation of instruments employ limb observations of the scattered solar radiation to retrieve vertical profiles of trace gas constituents and stratospheric aerosols. This technique combines high vertical resolution with near-global coverage, which makes it well suited for global atmospheric model assimilation, but requires sophisticated radiative transfer modelling to perform the retrieval. The results can be validated with more accurate, but sparser occultation data sets.

SCIAMACHY, the Scanning Imaging Absorption SpectroMeter for Atmospheric CHartography on ESA's Envisat spacecraft is one such instrument employing the limb-scatter observation geometry. It provided broadband limb radiance measurements from 2002–2012 covering a period of undisturbed background stratospheric aerosol

conditions in the first years of its lifetime and several volcanic eruptions with stratospheric impact from 2005 onwards. Thus, its comprehensive data set offers the rare possibility to investigate stratospheric aerosols under changing aerosol loads.

Goal of the work presented in this dissertation is to employ limb-scatter measurements with the SCIAMACHY instrument to retrieve stratospheric aerosol extinction profiles that form a valuable data set with global coverage on a daily basis. This data set shall have the potential to serve as input data for global circulation models and as a foundation for climatological interpretation with respect to natural variability under background conditions and in volcanically influenced periods as well as to potential anthropogenic impact in the context of climate change.

Outline

The thesis is divided into three parts.

Part I provides fundamental background information on the physical properties of stratospheric aerosols and their role in the climate system as well as a short history of their investigation and an overview of common reseach methods. The Mie theory that physically describes the scattering of light by sulfate aerosol particles is presented. Furthermore, it gives a description of the SCIAMACHY instrument and provides an insight into the limb-scatter measurement technique.

In Part II, the non-linear inverse method and the two versions V1.0 and V1.1 of the retrieval algorithm applied in this work to gain stratospheric aerosol extinction profiles from SCIAMACHY limb radiances are explained in detail. The forward model and retrieval code SCIATRAN is introduced as the tool which puts the retrieval method into practice. This part concludes with sensitivity studies with respect to various parameters.

In Part III the results of the two retrieval versions are presented and validated

with a highly accurate stratospheric aerosol extinction data set. Time-latitude morphologies of the complete SCIAMACHY aerosol extinction data set V1.1 are presented and discussed. The thesis closes with the summary and suggestions for future investigations.

Part I

Fundamentals

1 Stratospheric aerosols

1.1 From first detection to satellite measurements

The history of stratospheric aerosol observations began in August 1883 with the explosion of the small Indonesian island Krakatoa in a massive volcanic eruption. Nine days later, Sereno E. Bishop discovered in Honolulu/Hawaii what he described as a ”faint halo” around the sun, the first documented evidence of stratospheric aerosols, subsequently named ”Bishop’s ring” after him (Bishop, 1884). In the years following the eruption, exceptionally red and glowing twilights were observed all over the world, lasting long after sunset. These observations were correctly associated with particles in the upper atmosphere transported on a global scale following the eruption (e.g., Aitken, 1884, Symons et al., 1888).

In 1902, Léon Teisserenc de Bort and Richard Aßmann simultaneously used the newly developed technique of unmanned instrumented ballons to discover a region in the atmosphere with zero lapse rate, known today as the tropopause. Teisserenc de Bort suggested that the atmosphere was divided into two layers and named them ”troposphere” and ”stratosphere”.

The experience made with Krakatoa and following major volcanic eruptions made obvious that volcanoes have a large impact on the stratospheric aerosol loading with the potential to influence number concentration and composition for years after the eruption (Deshler et al., 2006). The period from 1883 to present was dominated by eight major volcanic eruptions (see Table 1.2), overall roughly 50

had a documented stratospheric impact with partly long time periods between the eruptions (Sato et al., 1993, Stothers, 1996, Deshler et al., 2006, Yang et al., 2010).

In one of these gaps, in 1959 – almost 30 years after the last significant volcanic eruption, the Quizapo in 1932 (Stothers, 1996) – Junge et al. (1961) performed the first direct proof of the existence of stratospheric aerosols by performing balloon-borne in-situ measurements of vertical concentration profiles in three aerosol size categories up to an altitude of 30 km. They found that smaller particles of radii between 0.01 and 0.1 μm decreased in concentration from the tropopause to nearly zero at 20 km, whereas larger particles (0.1 – 1.0 μm) formed a maximum at about 20 km. The chemical analysis of the larger particles suggested hygroscopic behaviour with sulfur as the main constituent, a finding that was confirmed by Rosen (1971) by determining the boiling point of stratospheric aerosols, inferring on a composition of 75 % H_2SO_4 and 25 % H_2O. Junge et al. (1961) concluded "tentatively" and basically correctly that the small particles were of tropospheric origin, while the larger particles were formed in the stratosphere by oxidation of sulfuric source gases. A third mode of less hygroscopic particles larger than 1.0 μm, which was found to have a very short lifetime, low frequency of occurrence, and high fluctuation in time, was assigned to meteoric dust particles. Subsequent balloon- and aircraft-borne measurements confirmed the presence of a stable and world-wide stratospheric sulfuric aerosol layer (Chagnon and Junge, 1961, Junge and Manson, 1961). These sulfate aerosols of obvious non-volcanic origin – already hypothized by Gruner and Kleinert (1927) as a "disturbance layer" between 20 and and 30 km altitude responsible for purple light in the western sky after sunset – form the background aerosol level with the so-called Junge Layer at about 20 km.

In the early 1970s, the first long-term measurements to investigate the stratospheric background aerosol layer and the role of volcanic eruptions were established. Balloon borne Optical Particle Counters (OPC) delivered important information

about microphysical properties of stratospheric aerosols above Laramie, Wyoming, USA, with growing accuracy and versatility from 1971 to present (e.g., Hofmann et al., 1975, Deshler, 2003). The results of these localized long-term in-situ measurements are used in this work as the major source for aerosol micropysical parameters.

The first operational ground-based lidar (LIght Detection And Ranging) routine measurements for long-term stratospheric aerosol monitoring started also in the early 70s in São José dos Campos, Brazil, and were subsequently extended to the Network for the Detection of Stratospheric Change (NDSC) consisting of eight lidar stations between 79°N and 78°S which provide a long-term data set of vertical profiles of aerosol extinction and aerosol backscatter with a high operation rate (Ferrare et al., 1998, Hamill et al., 2006).

The beginning of the satellite era in the late 1970s opened up new possibilities for measuring stratospheric aerosols. Although in general with lower accuracy and lower spatial resolution than in-situ or lidar measurements, satellite measurements provide the possibility to observe stratospheric aerosols continuously on a global scale, which is essential for monitoring the spatial distribution of volcanic aerosols with time as well as the long-term variation of stratospheric aerosols in general.

The first space-borne instrument focusing on stratospheric aerosols was the Stratospheric Aerosol Measurement (SAM) II, which was in orbit from 1978–1993 onboard the Nimbus-7 spacecraft (Pepin et al., 1977, McCormick et al., 1979). Together with three following missions, the Stratospheric Aerosol and Gas Experiment (SAGE, 1979–1981), SAGE II (1984–2005), and SAGE III (2002–2006), it formed the SAGE series of NASA instruments that have produced comparable global measurements of stratospheric aerosol extinction in the visible and near infrared continously since 1978 (McCormick et al., 1979, Russell and McCormick, 1989, Thomason and Taha, 2003, Hamill et al., 2006). This set of instruments used the solar occultation technique to measure aerosol extinction at one (1000 nm, SAM II) to nine (386–1545 nm,

SAGE III) wavelengths with an uninterrupted combined aerosol extinction data set near 1000 nm from October 1978 to March 2006. Until the termination of the SAGE III mission in 2006, the solar occultation technique was the common measurement geometry for satellite-based instruments focused on stratospheric aerosols. It measures solar radiation at the above-mentioned discrete wavelengths transmitted through the atmosphere looking directly into the rising or the setting sun, each once per orbit. At each observation, measurements are performed at successive tangent height steps at altitudes from at least 10–30 kilometers (SAM II), giving a height profile of the transmission and subsequently the aerosol extinction (e.g., Chu et al., 1989). Because of the advantages of this technique – accurate aerosol extinction profiles typically with high vertical resolution at multiple wavelengths, and the spectral dependence of the extinction coefficients allows inferring information on the aerosol particle size (Lenoble et al., 1984, Brogniez et al., 1992, Brogniez and Lenoble, 1988) – and the outstanding duration and quality of the combined aerosol extinction data set, the aerosol extinction derived from the SAGE series and particularly SAGE II is generally considered to be one of the stratospheric aerosol data sets with the highest accuracy. For this reason, the SAGE II data set is used for comparisons with the SCIAMACHY results in this work.

Currently, the MAESTRO (Measurements of Aerosol Extinction in the Stratosphere and Troposphere Retrieved by Occultation) instrument measures the vertical distribution of aerosols. It was launched aboard the satellite SCISAT-1 in 2003 and consists of a UV-VIS-NIR spectrophotometer that measures transmitted sunlight in the 285–1030 nm spectral region (McElroy et al., 2007).

Other instruments using the sun occultation technique were the HALOE (HALogen Occultation Experiment) instrument and the POAM (Polar Ozone and Aerosol Measurement) instrument series. HALOE operated from 1991–2005 onboard the Upper Atmosphere Research Satellite (UARS), measuring aerosol extinction at four

wavelengths in the infrared (Russell et al., 1993). POAM II and III were operating from 1993–1996 and 1998–2005 onboard the SPOT-3 and SPOT-4 satellites, repectively, obtaining aerosol extinction in the latitude bands 54–71°N and 63–88°S at five wavelengths in the visible/near infrared (e.g., Glaccum et al., 1996, Lumpe, 2002, Lucke et al., 1999).

The disadvantage of solar occultation measurements is that the number of occultations is limited to one sunrise and one sunset observation per orbit at most. Moreover, the latitudes of these observations change only slowly with time. With the demise of SAGE III in 2006, the era of sun occultation instruments came to a preliminary end. With the installation of a nearly exact replica of SAGE III on the International Space Station (ISS) in 2014 only one further mission is planned. Newer techniques have to continue the space-based observations of stratospheric aerosol.

Stellar occultation, e.g., by GOMOS (Global Ozone Monitoring by Occultation of Stars) onboard the European satellite Envisat (Bertaux et al., 1991, Vanhellemont et al., 2005) can also be used to measure multi-spectral aerosol extinction profiles providing significantly enhanced geographical coverage, but with a much lower signal-to-noise ratio due to using transmitted starlight instead of sunlight for the determination of the stratospheric aerosol extinction.

The american-french satellite CALIPSO (Cloud-Aerosol Lidar and Infrared Pathfinder Satellite Observations) measures the stratosheric aerosol layer since April 2006 with a combination of the lidar instrument CALIOP (Cloud-Aerosol Lidar with Orthogonal Polarization), the Imaging Infrared Radiometer (IIR), and the Wide Field Camera (WFC) (e.g., Winker et al., 2007, Vernier et al., 2009).

A new generation of instruments employ limb-scatter observations (see Chapter 4) to retrieve vertical profiles of trace constituents and stratospheric aerosols. Using scattered solar radiation, this technique is not dependent on a direct view into the

sun and thus is able to combine a high vertical resolution with near-global coverage, but requires sophisticated radiative transfer modelling to perform the retrieval.

Until 2001 only very few studies employed limb radiance measurements to infer stratospheric aerosol extinction coefficients or size parameters, none of them with the above-mentioned advantages of space-based observations. Cunnold et al. (1973) used photometer measurements of limb-scattered sunlight made from the X-15 aircraft at six spectral intervals to infer aerosol extinction profiles with an optimal estimation scheme. Ackerman et al. (1981) used balloon-borne photographic observations of the azimuthal variation of limb radiances to establish the aerosol phase function. McLinden et al. (1999) employed profiles of limb radiance and the degree of linear polarization measured with the CPFM (Composition and Photodissociative Flux Measurement) instrument flown aboard NASA's ER-2 plane to retrieve vertical profiles of stratospheric aerosol number density and size parameters.

In 2001, the first satellite-based limb-scatter instrument was launched, the Optical Spectrograph and Infrared Imaging System (OSIRIS) (Llewellyn et al., 2004) on the Swedish/Canadian/Finnish/French Odin satellite (Murtagh et al., 2002). It was operative in a sun-synchronous orbit at an altitude near 600 km from February 2001 to date, measuring scattered sunlight in the wavelength region 280–810 nm at latitudes from 82°N to 82°S. Bourassa et al. (2007, 2008, 2012) retrieved stratospheric aerosol properties from OSIRIS radiance profiles.

SCIAMACHY, the Scanning Imaging Absorption SpectroMeter for Atmospheric CHartography (Burrows et al. (1995), Bovensmann et al. (1999), and references therein) on ESA's Envisat spacecraft orbited the earth from in roughly 800 km altitude from March 2002 to the sudden communication loss in April 2012. SCIAMACHY was one of only a few instruments performing limb measurements in the UV-VIS-NIR spectral region (Noël et al., 2002). Two wavelengths of its broadband limb radiance spectra are used for the aerosol extinction retrieval in this work.

Onboard the same satellite, GOMOS – primarily a stellar occultation instrument – is also capable of performing limb-scatter measurements on the dayside of each orbit (Kyrölä et al., 2004, Taha et al., 2008).

The limb sensor of the recently launched Ozone Mapping/Profiler Suite (OMPS) aboard NPP (Suomi National Polar-orbiting Partnership) (Lee et al., 2010) measures the along-track limb-scattered solar radiance in the spectral range of 290 to 1000 nm.

Table 1.1 gives an overview of the instruments used for stratospheric aerosol measurements. The Chapters 3 and 4 provide detailed information about the instrument SCIAMACHY and the limb-scatter technique.

Instrument	Satellite	Mission duration	Geographical coverage	Wavelengths [nm]	Orbit	Observation geometry
SAM II	Nimbus-7	1978–1993	64–83°N, 64–83°S	1000	sun-synch.	Sun occultation
SAGE I	AEM-B	1979–1981	80°N–80°S	4 between 385–1000	non-sun-synch.	Sun occultation
SAGE II	ERBS	1984–2005	80°N–80°S	7 between 386–1020	non-sun-synch.	Sun occultation
SAGE III	Meteor-3M	2002–2006	48–80°N, 26–60°S	9 between 386–1545	sun-synch.	Sun/Moon occultation
HALOE	UARS	1991–2005	80°N–80°S	8 between 2450–10040	non-sun-synch.	Sun occultation
POAM II	SPOT-3	1993–1996	54–71°N, 63–88°S	9 between 352–1060	sun-synch.	Sun occultation
POAM III	SPOT-4	1998–2005	54–71°N, 63–88°S	9 between 354–1020	sun-synch.	Sun occultation
MAESTRO	SCISAT-1	2003–present	90°N–90°S	285–1030	non-sun-synch.	Sun occultation
GOMOS	Envisat	2002–2012	90°N–90°S	248–690, 750–776, 916–956	sun-synch.	Stellar occultation/limb-scatter
OSIRIS	Odin	2001–present	82°N–82°S	280–810	sun-synch.	Limb-scatter
OMPS	NPP	2011–present	90°N–90°S	290–1000	sun-synch.	Limb-scatter
SCIAMACHY	Envisat	2002–2012	≈85°N–85°S	214–2386	sun-synch.	Sun+moon occ./Limb-scatter
CALIOP	CALIPSO	2006–present	82°N–82°S	532, 1064	sun-synch.	Lidar

Table 1.1: Overview of satellite instruments employed for measuring stratospheric aerosols.

1.2 Lifecycle

1.2.1 Background stratospheric aerosols

Following Hamill et al. (1997), the lifecycle of stratospheric background aerosols covers three main stages: particle formation from source gases, development of a size distribution trough transport and mixing, and removal from the stratosphere.

Formation:

From the first direct measurements of stratospheric aerosols, Junge et al. (1961) concluded that sulfur was the main constituent of the collected liquid droplets, a finding that Rosen (1971) confirmed and extended by means of boiling point determinations which suggested a composition of 75 % sulfuric acid and 25 % water. Since no sources of sulfur exist in the stratosphere, stratospheric sulfate aerosols must have their origin in the troposphere.

The tropical upper troposphere/lower stratosphere region plays a key role in the formation of stratospheric sulfate aerosols because convection in the intertropical convergence zone (Goodman et al., 1982, Yue and Deepak, 1984) and slow diabatic ascent into the tropical stratosphere determined dynamically by extratropical wave-driven pumping (Holton et al., 1995) turned out to be the main transport processes of source gases and particles into the lower stratosphere. Studies by Brock et al. (1995) showed that new particle formation takes place in this region.

Crutzen (1976) suggested tropospheric carbonyl sulfide (OCS) to be the source gas for stratospheric sulfate particles, an assumption that turned out to be correct but not sufficient. Model calculations by, for example, Weisenstein and Bekki (2006) and Notholt and Bingemer (2006) showed that the contributions of SO_2 and OCS to the stratospheric sulfur content are of the same order of magnitude. The total sulfur emission at the earth's surface – source for stratospheric sulfate aerosols – is on the

order of 100 Tg/year (Carslaw and Kärcher, 2006), dominated by anthropogenic sulfur dioxide (SO_2) emissions in the industrial period (Carslaw and Kärcher, 2006). Due to the short atmospheric lifetime of SO_2 (10–20 days), its role in stratospheric aerosol formation is relatively small compared to the amount generated at the earth's surface. In contrast, OCS – generated mainly by non-anthropogenic marine processes (Kettle et al., 2002) – contributes only a small part of the total sulfur emission, but its long tropospheric lifetime of two years (Khalil and Rasmussen, 1984) makes it a significant source for the formation of sulfate aerosols in the upper troposphere/lower stratosphere region. Molecules of these two major source gases are – along with other, minor sulfuric precursor gases as dimethyl sulfide (CH_3SCH_3), carbon disulfide (CS_2), or hydrogen sulfide (H_2S) – transported into the tropical tropopause region in deep convective clouds (Chatfield and Crutzen, 1984) and by lifting of air masses in warm conveyor belts (Eckhardt et al., 2004).

There the source gases are photolysed and/or oxidized to H_2SO_4, the direct gaseous precursor of liquid sulfate aerosol droplets. Since the tropospheric lifetime of H_2SO_4 is on the order of minutes, the ultraviolet photolysis of OCS described by Crutzen (1976) and the in-situ oxidation of SO_2 and OCS are the main processes generating H_2SO_4 in the stratosphere (Notholt and Bingemer, 2006). Below 25 km, SO_2 is the dominant source gas, above 25 km OCS (Deshler, 2008).

For the formation of liquid sulfuric acid droplets from gas phase H_2SO_4, condensation nuclei must be available. Brock et al. (1995) showed by atmospheric measurements and numerical calculations that homogeneous nucleation from gas phase H_2SO_4 and H_2O molecules in the tropical tropopause region can provide these nuclei. Hunten et al. (1980) and Cziczo et al. (2001) found particles of meteoric, Turco et al. (1979) of tropospheric origin in the upper and lower stratoshere, respectively. In-situ measurements of the chemical composition of individual lower stratospheric aerosol particles by Murphy (1998) indicated particles of pure H_2SO_4/H_2O and oth-

ers containing small amounts of meteoric material or organic material, implicating a mixture of the three sources for condensation nuclei.

There is evidence that H_2SO_4 particle formation in the upper troposphere followed by transport across the tropical tropopause by overshooting convection provides a source equivalent to the sum of the precursor gases entering the stratosphere in gas phase (Deshler, 2008, Weisenstein and Bekki, 2006). Sensitivity analysis for SO_2 and sulfate inputs by Notholt and Bingemer (2006) and in-situ aircraft measurements of sulfate particles in the tropical tropopause by Jonsson et al. (1995) fortify this finding.

The suspicion that the increasing aircraft exhaust could have a significant impact on stratospheric aerosol formation could not be confirmed at this point in time. Several publications of in-situ measurements and model calculations (e.g., Arnold et al., 1998, Kjellstrom et al., 1999) were reviewed by Kärcher (1999), drawing the conclusion that even in the North Atlantic flight corridor north of 40°N the flight traffic induced contribution to the stratospheric sulfate mass is only about 1 % (Deshler, 2008). Long-time trend analysis of stratospheric background aerosols by Deshler et al. (2006) showed no positive trend in the last 40 years despite the increase of air traffic in this time period.

Transport and development of a size distribution:

Following model calculations of Hamill et al. (1997), the process of nucleation is able to produce only very small particles with radii around several nanometers. To grow to particle sizes found by in-situ measurements, other processes are necessary. Subsequent to the initial formation, condensation of stratospheric H_2SO_4 and water molecules around the condensation nuclei occurs, followed by coagulation with surrounding newly formed or larger aged particles. These processes lead to a sulfuric acid solution with a relatively constant proportion of 75 % H_2SO_4 and 25 %

water. Since due to the low vapor pressure of H_2SO_4 each free molecule is quickly caught by an existing particle which then condenses water and rising/shrinking temperature leads to release/uptake of water. The exact composition of the two constituents depends on the temperature and the availability of gas phase H_2SO_4 (Deshler, 2008). Yue et al. (1994) gave an overview of the latitudinal, seasonal, and height dependence of the stratospheric aerosol acidity and the resulting refraction index derived from SAGE II satellite measurements.

While the the zonal transport of aerosols generated in the tropical tropopause region happens rapidly with the mean stratospheric winds (depending on the phase of the quasi-biennial oscillation (QBO), see for example Trepte and Hitchman (1992)), meridional transport is limited to large-scale stirring and mixing (Carslaw and Kärcher (2006) citing Trepte and Hitchman (1992)). Following Trepte and Hitchman (1992), who interpreted SAGE I/II observations of stratospheric aerosols from 1979–1981 and 1984–1991 by means of a model of the QBO meridional circulation and equatorial wind observations, meridional aerosol transport from the tropics is behaving differently in different layers of the lower stratosphere. Within a few kilometers above the tropopause, poleward transport to the mid-latitudes happens relatively unhindered primarily to the winter hemisphere and preferably during QBO westerly shear (”westerly shear” – not to be confused with ”westerly phase” – means a strong gradient in the zonal stratospheric wind with a shift of the wind direction form easterly to westerly with rising altitude). Above approximately 20 km the meridional transport is blocked by the dynamics driving the QBO, leading to a pronounced maximum in the tropics and a strong boundary between 15° and 30° of each hemisphere (see also Plumb (1996)). Upper layer outflow from this reservoir is steered by the Brewer-Dobson circulation, occuring more readily during QBO easterly shear. Additionally, Trepte and Hitchman (1992) found that the altitude of the particle number density maximum – the Junge layer – is shifted by

the QBO, to a maximum altitude of 28–30 km, during an easterly QBO shear.

During the poleward transport, condensation of gaseous H_2SO_4 and H_2O and coagulation with fresh and aged aerosol droplets continue. Simultaneously, gravitational settling moves the larger particles closer to the tropopause (Deshler, 2008).

The combination of these mechanisms finally leads to a quasi-steady background aerosol distribution with a pronounced reservoir in the tropical lower stratosphere with relatively slow meridional transport and a particle size distribution (PSD) confirmed by measurements by Deshler (2003) and others (see below). The bottom of the layer is the troposphere, the top at approximately 35 km where sulfate particles evaporate completely due to high temperatures and low partial pressure of H_2SO_4 and H_2O (Carslaw and Kärcher, 2006).

Removal:

Following Holton et al. (1995), the removal of aerosols from the stratosphere is dominated by large-scale dynamics, not by local events near the tropopause. Very tightly summarized, the propagation of small- and large-scale tropospheric waves into the stratosphere followed by their dissipation generates a predominantly and persistently wave-induced westward force which in the extra-tropics leads to a poleward mass flow induced by the Coriolis force. This poleward-pushed air is forced downward by mass continuity and the general behaviour of the extratropical response to the zonal force, the lower layers entering the troposphere. As mentioned above, depending on the QBO phase the peak activity occurs in the winter hemisphere (Trepte and Hitchman, 1992). The mean stratospheric residence time with respect to this removal mechanism is approximately two years.

Furthermore, stratospheric air masses enter the troposphere diabatically through tropopause folds and through subsidence in the polar vortex during winter and spring (Carslaw and Kärcher, 2006), but these are much slower with corresponding

residence times of approximately eight years for both processes (Hamill et al., 1997).

Additionally, stratospheric aerosols serve as condensation nuclei for polar stratospheric clouds (PSCs) during polar winter and are transported into the troposphere with the sedimentation of the relatively large PSC particles (Carslaw and Kärcher, 2006).

Beside the role in PSC sedimentation, gravitational settling contributes only incirectly to the removal of stratospheric aerosols by moving particles closer to the tropopause where they can be removed by the above-mentioned processes which are rapid compared with gravitational settling (Deshler, 2008).

Once in the troposphere, sulfate aerosols are depleted rapidly as condensation nuclei for cirrus clouds and – being highly reactive – by tropospheric chemistry.

In summary, the vast majority of stratospheric background aerosols are liquid droplets of sulfuric acid droplets which are mainly formed in the tropical tropopause region by nucleation of H_2SO_4 molecules oxidized from the dominant source gases OCS and SO_2, followed by coagulation with existing or newly formed particles and condensation of gas phase H_2SO_4 and water. Meridional transport is slow, leading to a tropical reservoir and a stratospheric lifetime of approximately two years before being removed to the troposphere predominantly by large-scale dynamical processes.

1.2.2 Volcanic perturbations

In contrast to the days of the early measurements by Junge and others, the era of space-based aerosol measurements have been dominated by several major volcanic eruptions. Volcanic eruptions can have a large impact on stratospheric aerosols by injecting large amounts of gas and ash into the stratosphere.

Since large particles as soot and ash are removed from the stratosphere by gravity within days, the gaseous constituents of the eruption column – first of all SO_2 – have

by far the strongest influence on the stratospheric aerosol constitution by providing source material for the formation and growth process described above. After the volcanic eruption of El Chichón in 1982, Hofmann and Rosen (1984) found that volcano-induced stratospheric aerosols consist of droplets of 75 % sulfuric acid and 25 % water as well. Deshler et al. (1992) and Sheridan et al. (1992) comfirmed that finding after the eruption of Mount Pinatubo in 1991, the eruption with the strongest stratospheric impact since the beginning of stratospheric aerosol measurements in the early 1960s. In general, the formation, transformation, and removal mechanisms from gaseous precursors to sulfate droplets are similar to those for background aerosol discussed above, but the resulting PSD differs significantly (see Section 1.4).

Two factors are crucial in determining the potential of a volcanic eruption to affect the stratospheric aerosol composition significantly and for a longer period: the eruption must release a large amount of sulfur and must be powerful enough for the eruption column to reach the stratosphere. The Volcanic Explosivity Index (VEI) developed by Newhall and Self (1982) is a measure for the strength of a volcanic eruption and – particularly important with respect to this work – the maximum altitude of the column. A VEI of 3, 4, or 5+ means the column reaches a maximum altitude of 3–15 km, 10–25 km, or >25 km, respectively. Despite the fact that extratropical volcanos with VEI 3 are potentially able to reach the lower stratosphere, the focus here lies on volcanos with VEI 4+.

Table 1.2 lists the eight major eruptions mentioned in Section 1.1 that strongly impacted the stratosphere since 1883. Four are falling in the period after the long gap in which Junge performed the first in-situ measurements (Sato et al., 1993, Stothers, 1996). Three of these are assigned a VEI of 5+, i.e. the eruptions of Agung (1963, 8°S), El Chichón (1982, 17°N), and Mt. Pinatubo (1991, 15°N). The eruption of Fuego (1974, 15°N), even though with a VEI of only 4, strongly influenced the stratosphere by injecting 3–6 Tg of aerosols, but was limited primarily to altitudes

Name	Year	Latitude	Longitude	VEI	SO_2 [Tg]	Aerosol [Tg]
Krakatau	1883	6°S	105°E	6		44
Unidentified	1890	?	?	?		6–24
Santa Maria	1902	15°N	92°W	6		30
Katmai/Novarupta	1912	58°N	155°W	6	5	11–30
Agung	1963	8°S	116°E	5	10	16–30
Fuego	1974	15°N	91°W	4		3–6
El Chichón	1982	17°N	93°W	5	8	12
Mt. Pinatubo	1991	15°N	120°E	6	17–20	30

Table 1.2: Names, dates, locations, Volcanic Explosivity Index (VEI), SO_2 and aerosol loading (if available) of volcanic eruptions with strong stratospheric impact since the first detection of stratospheric aerosols.

below 20 km (Deshler, 2008). An additional two eruptions in this period had a VEI of 5 without significantly affecting the stratospheric aerosol layer. The Mount St. Helens (1980, 46°N) ejected a large amount of silicates and other large particles, but only a small amount of sulfur gases (<1 Tg), thus the impact was small and short-lasting (Robock, 1981). The Cerro Hudson (1992, 46°S) released more than 3 Tg SO_2, but got lost in the Mt. Pinatubo eruption with ∼30 Tg a few months earlier.

Figure 1.1 shows the 1970–2007 history of stratospheric aerosols from five lidar and in-situ measurement sites at tropical or mid-latitudes (Deshler, 2008). The eruptions of Fuego, El Chichón, and Mt. Pinatubo and their long lasting stratospheric impact with an e-folding time of 0.8–1.5 years are clearly visible at all measurement sites, the Fuego due to its VEI of 4 predominantly between 15–20 km (bottom panel). The 1980 Mount St. Helens eruption is displayed only by a sharp peak at Laramie, Wyoming, USA in the vicinity of the eruption (bottom two panels). The Cerro Hudson (1992) vanishes in the dominating Mt. Pinatubo (1991) signal.

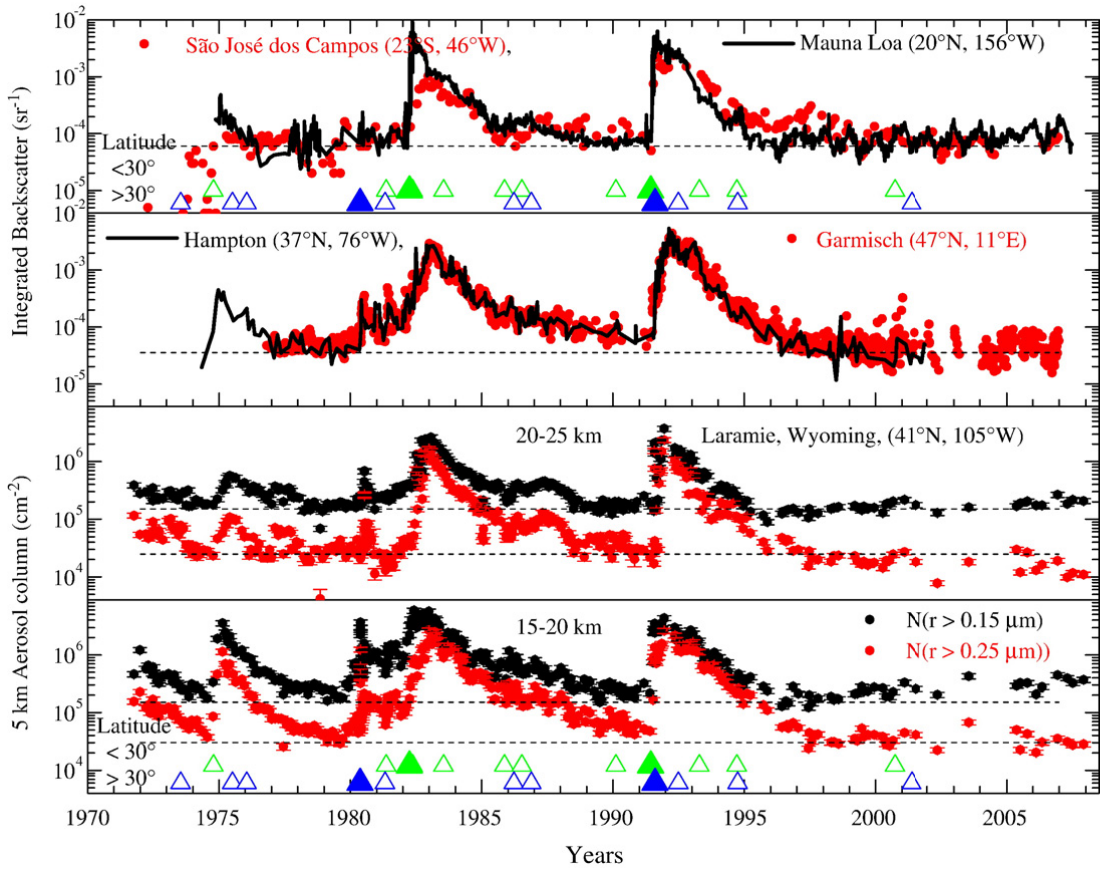

Figure 1.1: History of stratospheric aerosols from 1970–2007 as integrated backscatter above the tropopause from two tropical (first panel) and two mid-latitude (second panel) lidar sites and the integral columns of number between 20–25 km (third panel) and 15–20 km (fourth panel) from in-situ balloon measurements at Laramie, Wyoming, USA. The green and blue triangles represent volcanic eruptions with VEI 4 (open triangle) and 5+ (closed triangle) at latitudes <30° and >30°, respectively (figure from Deshler (2008)).

Since the source gas output of volcanic eruptions in the tropics contributes directly to the tropical reservoir as the source region of the stratospheric aerosol cycle, it is assumed that these volcanos have a stronger impact on the global stratospheric aerosol distribution than comparable volcanic eruptions at high latitudes. Satellite observations by Bourassa et al. (2010) and model calculations by Kravitz et al. (2010) concerning the stratospheric impact of the high latitude volcanos Kasatochi

and Okmok in 2008 fortify this assumption. Note that all four eruptions with significant stratospheric impact mentioned above happened in the tropics.

Next to the relatively sporadic strong volcanic eruptions ejecting source gases directly into the stratosphere (depending on the tropopause height and thus the latitude), the larger number of weaker eruptions not reaching the stratosphere have a significant combined impact on the stratospheric aerosol formation by increasing the source gas concentration in the upper troposphere (Thornton et al., 1999). In particular, such volcanic entry of source gases in the tropical upper troposphere can add noticeably to the stratospheric aerosol formation. Vernier et al. (2011) investigated the influence of such minor eruptions in the tropics from 2000–2009.

However, the – from a stratospheric point of view – volcanically quiescent period from the decay of the Mt. Pinatubo influence in the mid 1990s to the eruption of Manam in January 2005 offers the unique chance to investigate stratospheric aerosol properties without a direct volcanic insertion into the stratosphere within almost three years of the SCIAMACHY data set. In the last seven years of its lifetime, SCIAMACHY witnessed a set of volcanic eruptions with direct stratospheric impact.

Recent studies by, for example, Fromm et al. (2000) and Siddaway and Petelina (2011) demonstrated that a combination of extreme heat energy release and convection named ”pyroconvection” or ”pyrocumulonimbus” can have a similar effect as large volcanos influencing the stratospheric aerosol loading by explosively accelerating smoke material from biomass burning to enable the penetration of the tropopause.

1.3 Influence on global climate and stratospheric chemistry

Stratospheric aerosols are of great importance to both the atmosphere's radiative balance and stratospheric chemistry. Depending on the effective radius of the sulfate droplets, they can have a *direct* positive or negative radiative forcing effect (Lacis et al., 1992). Sulfate aerosols are efficient scatterers and weak absorbers at solar wavelengths, but absorb the thermal infrared radiation coming from the surface. Microphysical properties – mainly the droplet size defined by the effective radius r_{eff} (see Section 1.4) – decide which effect dominates. Particles with $r_{eff} < 2\,\mu m$ predominantly scatter the incoming solar radiation and therefore cool the planet by increasing the planetary albedo. For particles with $r_{eff} > 2\,\mu m$, absorption and re-emission of thermal IR radiation from below the tropopause dominates, thus large aerosol droplets contribute to the greenhouse effect warming the atmosphere. While the direct effect of background aerosols is rather small it has a significant impact on the Earth's radiation balance after strong volcanic eruptions (McCormick et al., 1995, Self et al., 1997). Even in times of a strong volcanic aerosol loading with large particle radii, the cooling effect dominates since the effective radius stays well below the critical value (Lacis et al., 1992, Valero and Pilewskie, 1992). For example, after the eruption of the Mt. Pinatubo on June 15th, 1991, Stowe et al. (1992) calculated from measured aerosol optical depths a decrease of the globally averaged net radiation at the top of the atmosphere by about $2.5\,W/m^2$ in late 1991, translating into a global cooling of 0.5 to 0.7°C. Values on this order were confirmed by northern hemisphere temperature records by Dutton and Christy (1992) and model calculations by Hansen et al. (1992). In the stratosphere, increased absorption led to significantly higher temperatures of up to 4 Kelvin at altitudes and locations where the Mt. Pinatubo eruption produced the highest stratospheric concentrations

of aerosols (Labitzke and McCormick, 1992).

Furthermore, stratospheric aerosols can *indirectly* affect the Earth's radiation budget. Aerosol particles descended through the tropopause in tropopause folds or by sedimentation can act as condensation nuclei of upper level clouds, leading with the same liquid or ice water content to more hydrometeors in the cloud with smaller effective radii. This leads to a higher albedo and thus a negative contribution to the radiative balance. Based on the work of Charlson et al. (1992), Minnis et al. (1993) investigated this effect after the Mt. Pinatubo eruption, Le Treut et al. (1998) confirmed their findings by means of model calculations.

Even though above described climate impacts are assumed to be small under background conditions, Solomon et al. (2011) concluded from several independent aerosol data sets and satellite data a negative radiative forcing of $-0.1\,\mathrm{W/m^2}$ between 1960–1990 and 2000–2010, respectively, due to an increase in the stratospheric background aerosol level during these periods.

Stratospheric aerosols also play an important role in the chemical balance of the stratosphere, particularly regarding ozone. Inside the polar vortex, sulfuric acid aerosols act as condensation nuclei in the formation of polar stratospheric clouds and participate in the halogen activation facilitating the heterogeneous chemistry that leads to the formation of the ozone hole in Antarctic spring, and to partly significant chemical ozone losses in the northern hemisphere lower polar stratosphere during Arctic spring (Solomon (1999), and references therein). Outside the polar vortices stratospheric sulfate aerosols can also lead to chlorine activation as a precondition for ozone destruction (Erle et al., 1998, Hanson and Ravishankara, 1995, Solomon et al., 1993). Catalytic heterogeneous processes on the particle surface convert stable chlorine reservoirs such as hydrogen chloride (HCl) and chlorine nitrate ($ClONO_2$) into photochemically active chlorine species as Cl_2, $ClNO_2$, and HOCl (Self et al., 1997). The mechanisms described above – inside and outside the polar

vortex – are more effective during periods of high volcanic aerosol load. Another mechanism particularly effective under background conditions was found during the period of high stratospheric aerosol loading after the major eruptions of El Chichón and Mt. Pinatubo (e.g., Johnston et al., 1992), i.e., the depletion of stratospheric NO_2 by the hydrolysis of N_2O_5 (e.g., Mozurkewich and Calvert, 1988). Fahey et al. (1993) showed the anticorrelation of the aerosol surface area and the NO_x/NO_y ratio, a measure for the ozone destruction potential of the reactive nitrogen reservoir (NO_y). Conversely, the low aerosol load of the background level causes high NO_x concentrations, leading to ozone loss from the nitrogen catalytic cycle (Crutzen, 1970). Since the hydrolysis of N_2O_5 saturates as aerosol surface area increases above 5–10 $\mu m^2/cm^3$, this mechanism gains in importance when the stratospheric aerosol loading is low (Carslaw and Kärcher, 2006, Prather, 1992). Additionally, two other chemical compounds interacting with ozone, ClO_x and HO_x, are affected by changes in NO_x (Solomon et al., 1996).

1.4 Aerosol microphysics

The combination of the processes described in Sections 1.2.1 and 1.2.2 – nucleation, coagulation, condensation, transport, mixing, gravitational settling, and removal to the tropopause – result in a lognormal particle size distribution of liquid sulfate aerosol droplets in the stratosphere (Davies, 1974). A lognormal distribution is a distribution of a variable whose logarithm is normally distributed. Two parameters, r_g and σ_g, describe a lognormal size distribution of aerosol particles with a total number density N (Hansen and Travis, 1974):

$$n(r) = \frac{N}{\sqrt{2\pi}\,\sigma_g\,r}\,\exp\left[-\frac{(\ln r - \ln r_g)^2}{2\sigma_g^2}\right] \tag{1.1}$$

where the *median radius* $r_g = e^{\mu}$ is the geometric mean of the lognormal distribution and σ_g is the standard deviation of the logarithm of the particle radii (normally distributed). μ denotes the arithmetic mean of the logarithm of the radii. The median radius can be understood as the radius which divides the distribution into a higher and a lower half with respect to the total particle number. The standard deviation σ of the lognormal distribution, often called *spread* or *distribution width* (for example in Deshler (2003)), often replaces σ_g, with $\sigma_g = \ln(\sigma)$. Another parameter often found in literature is the *mode radius* $r_M = e^{\mu-\sigma^2}$, the radius corresponding to the global maximum of the PSD. Multimodal PSDs are typically defined either by the mode radii or the median radii of the different modes. Figure 1.2 shows the median and mode radii of two PSDs together with the arithmetic *mean radii* $\bar{r} = e^{\mu+\sigma^2/2}$ of the lognormal distributions.

After analysing in-situ measured stratospheric aerosols of different sizes for 30 years (1971–2001) at altitudes up to 30 km above Laramie, Wyoming (41°N), Deshler (2003) suggested a bimodal lognormal size distribution for the aerosol particle sizes with one mode characteristic for the smaller background aerosols and the second mode for large volcanically induced aerosols with a changing influence depending on spatial and temporal distance to the last volcanic eruption with stratospheric impact. Typical values for the median radius of background aerosols are around 0.1 µm with $\sigma \approx 1.5$ and a number density N of 5–10 cm^{-3} (Carslaw and Kärcher, 2006, Deshler, 2003). The larger particle mode is very narrow under background conditions, around $r_g \approx 0.4$ µm with $\sigma \approx 1.1$ and $N \approx 0.1$ cm^{-3} at 20 km. While the number density of the small mode is relatively constant in altitudes up to 30–35 km, the one of the larger mode drops sharply with rising altitude, to $N \approx 0.01$ cm^{-3} above 25 km (Carslaw and Kärcher, 2006).

Strong volcanic eruptions can increase the mean particle size and the concentra-

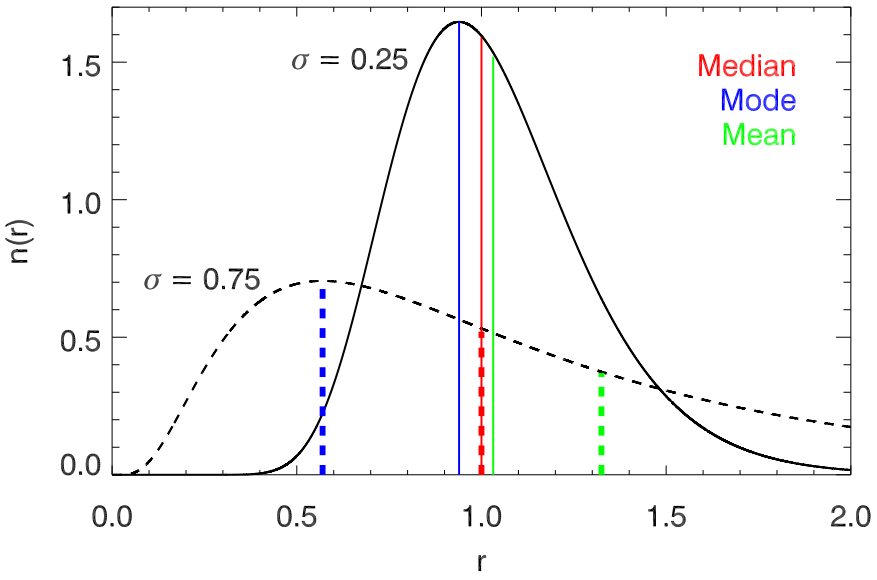

Figure 1.2: Two particle size distributions (PSDs) for N = 1 with the same median radius $r_g = 1$ (red) (both in arbitrary units) and distribution widths of 0.25 (solid curve) and 0.75 (dashed curve). Blue and green lines show the corresponding mode radii and mean radii, respectively.

tion dramatically. Figure 1.3 shows the altitude profiles of the median radii and the number densities for the two size modes above Laramie, Wyoming, USA (41°N), averaged over the three years following the Mt. Pinatubo eruption, 1992–1995, and the years 1995–2003 representing background conditions (Deshler, 2003, 2008).

During volcanic conditions, the number density of particles in the large mode is with $N \approx 1\,\mathrm{cm}^{-3}$ at altitudes around 20 km a factor 10 greater than during non-volcanic conditions while the median radius remains approximately constant. The median radius of the small mode increases be about a factor of 2, particularly below 25 km, while the number density remains more or less constant. With respect to the background conditions, volcanic eruptions seem to enlarge the particles of the small mode and increase the particle numbers of the large mode. Note that these values are 3-year/8-year means starting in 1992 and 1995, respectively, for a place at 41°N

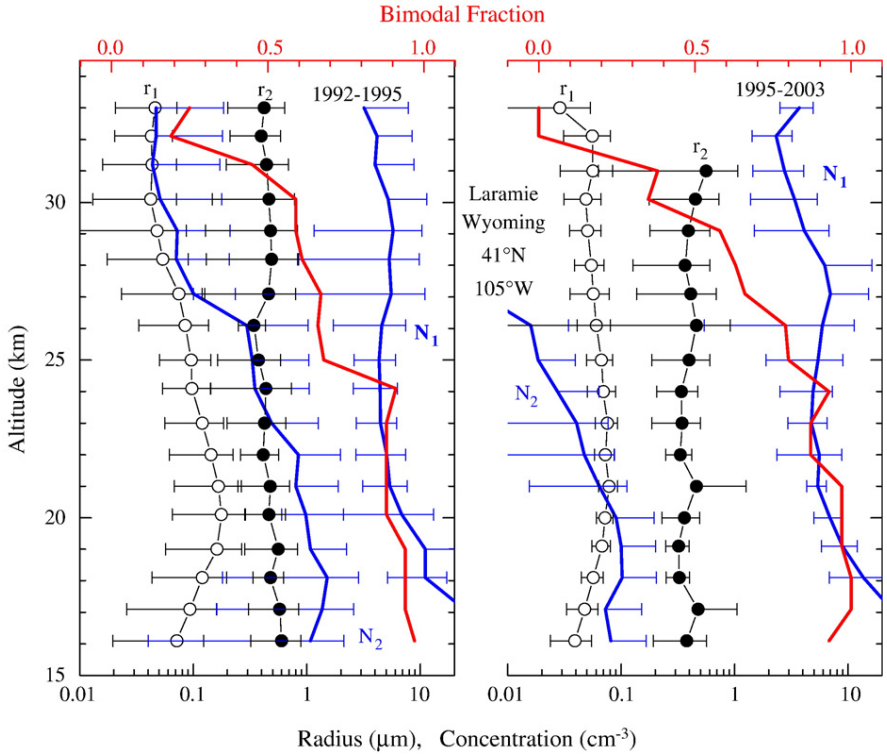

Figure 1.3: Altitude profiles of the median radii and the number densities for the two size modes of a bimodal lognormal particle size distribution fit to balloon measurements above Laramie, Wyoming, USA (41°N) averaged from 1992–1995 (left panel) and from 1995–2003 (right panel) (Deshler, 2003). The white (black) data points with standard deviations show the median radius r_1 (r_2) of the small (large) size mode, the corresponding number density is shown in blue with standard deviations, labelled N_1 (N_2). The fraction of measurements which were bimodal is displayed by the red lines with the scale at the top (figure from Deshler (2008)).

in North America, while the Mt. Pinatubo eruption took place in June 1991 at 14°N on the Philippines, more than 12,000 km away. Thus, these values represent a global impact of volcanic sulfur entry into the stratosphere. In single measurements closer in space and/or time to the eruption, the difference with respect to the background level can be much larger.

Figure 1.4 displays the bimodal lognormal PSDs for r_1, r_2, σ_1, σ_2, N_1, and N_2 fitted to two single measurements one year and 15 years after the Mt. Pinatubo eruption

above Laramie (after Deshler (2008)). One year after Mt. Pinatubo (left panel), r_1 is relatively large and the large particle mode is clearly visible. 15 years after the eruption (right panel), the median radius of the now dominating small particle mode decreased by a factor of 2 while the large mode is very weak. Since the picture in the right panel is representative for background distributions as of about six years after Mt. Pinatubo (Deshler, 2008), a monomodal PSD with $r_g = 0.11$ µm and $\sigma = 1.37$ neglecting the large particle mode is used to calculate the scattering phase function of stratospheric background aerosols used for the retrieval later in this work. In the following section we will explain how to derive the phase function, the extinction coefficient and other important properties of sulfate particles whose size is distributed lognormally.

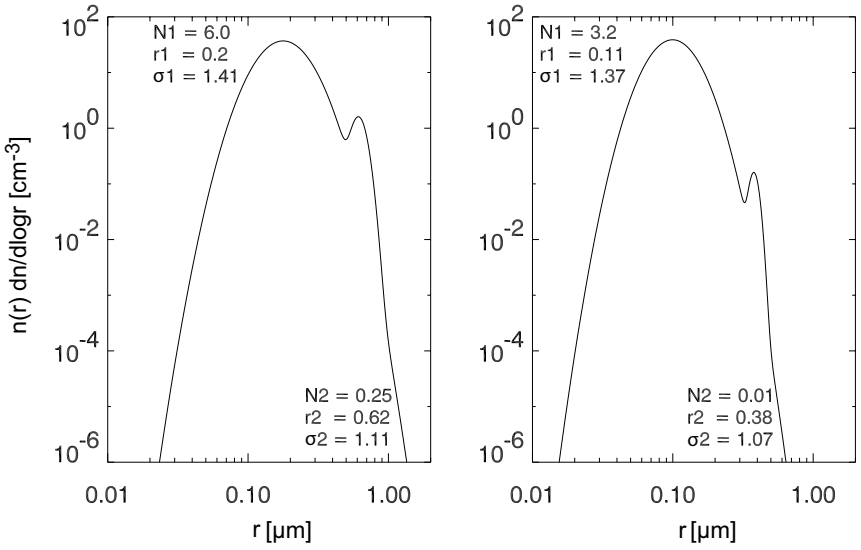

Figure 1.4: Particle size distributions derived from in-situ measurements from 24 June 1992 (left panel) and 06 May 2006 (right panel) above Laramie, Wyoming, USA (Deshler, 2003). r1 and r2 [µm] are the median radii of the small and the large size mode of the bimodal lognormal distribution, σ1 and σ2 (N1 and N2 [cm^{-3}]) the corresponding distribution widths (number densitities).

2 Mie theory

Since sulfuric acid droplets can be treated as homogeneous spherical particles and the radii – represented in size distributions by the effective radius

$$r_{\text{eff}} = r_{\text{g}} \exp\left(\frac{5}{2}\ln^2 \sigma_{\text{g}}\right) \tag{2.1}$$

– are on the same order as the wavelengths of the radiation measured by SCIAMACHY, it is suitable to use the Mie theory to describe the scattering by stratospheric sulfate aerosols (Mie, 1908). The Mie theory provides the exact solution of Maxwell's equations for the scattering of a plane electromagnetic (EM) wave of arbitrary wavelength by a spherical particle of arbitrary size. The particle has to be isotropic (optical properties are independent of the direction of the incoming light), homogeneous (characterized by a single complex refractive index at a given wavelength), and dielectric (non-conductive, and electrically polarizable). Stratospheric sulfate aerosols fulfill all these requirements. Although the Mie theory delivers the EM field at all points in and outside the particle, we focus on the far-field zone (i.e, the distance to the particle is much larger than the wavelength) as a suitable application for most atmospheric problems including measuring limb-scattered solar radiation. From this far-field solution, the desired parameters – scattering matrix (and the resulting phase function), cross-sections, extinction/scattering coefficients, and asymmetry parameter – are derived. We will restrict ourselves to a brief outline of the essential aspects since a complete formal solution would go beyond the scope of this thesis. The detailed theory can be found in standard works dealing with light

scattering, the following description is based mainly on Bohren and Huffman (1983). Under the above-mentioned conditions, Maxwell's equations can be converted to

$$\nabla \times \mathbf{H} = \epsilon \frac{\partial \mathbf{E}}{\partial t} \tag{2.2}$$

$$\nabla \times \mathbf{E} = -\mu \frac{\partial \mathbf{H}}{\partial t} \tag{2.3}$$

$$\nabla \cdot \mathbf{E} = 0 \tag{2.4}$$

$$\nabla \cdot \mathbf{H} = 0 \tag{2.5}$$

with **E** being the electric field vector, **H** the magnetic field vector, ϵ the dielectric constant, and μ the magnetic permeability. From these one can derive the vector wave equation for **E** and **H**

$$\nabla^2 \mathbf{E} = \epsilon\mu \frac{\partial^2 \mathbf{E}}{\partial t^2} \tag{2.6}$$

$$\nabla^2 \mathbf{H} = \epsilon\mu \frac{\partial^2 \mathbf{H}}{\partial t^2} \tag{2.7}$$

Due to the spherical particle shape, a transformation in spherical coordinates enables an analytical solution of the wave equations by applying the boundary condition that the tangential components of **E** and **H** must be continuous across the spherical surface of the particle. In the far-field zone, the Mie theory gives the solution of the vector wave equation for the scattered light $\mathbf{E}^s$ (propagating in direction z) in terms of the incident light $\mathbf{E}^0$:

$$\begin{pmatrix} E_{\parallel}^{s} \\ E_{\perp}^{s} \end{pmatrix} = \frac{\exp(-ikR+ikz)}{ikR} \begin{pmatrix} S_2 & S_3 \\ S_4 & S_1 \end{pmatrix} \begin{pmatrix} E_{\parallel}^{0} \\ E_{\perp}^{0} \end{pmatrix} \tag{2.8}$$

where $\parallel$ and $\perp$ denote the component polarized parallel and perpendicular to the scattering plane, respectively. $k = 2\pi/\lambda$ is the circular wavenumber and R the distance to the center of the scattering particle.

$\mathbf{S} = \begin{pmatrix} S_2 & S_3 \\ S_4 & S_1 \end{pmatrix}$ is the *amplitude scattering matrix* consisting of four angle-dependent *scattering functions* with $S_3(\Theta) = S_4(\Theta) = 0$ for spherical particles. The two non-zero scattering functions are expressed by infinite series

$$S_1 = \sum_{n=1}^{\infty} \frac{2n+1}{n(n+1)} (a_n \pi_n \cos\Theta + b_n \tau_n \cos\Theta) \tag{2.9}$$

$$S_2 = \sum_{n=1}^{\infty} \frac{2n+1}{n(n+1)} (b_n \pi_n \cos\Theta + a_n \tau_n \cos\Theta) \tag{2.10}$$

where the *Mie coefficients* a_n and b_n are

$$a_n(x,y) = \frac{\psi_n'(y)\psi_n(x) - m\psi_n(y)\psi_n'(x)}{\psi_n'(y)\xi_n(x) - m\psi_n(y)\xi_n'(x)} \tag{2.11}$$

$$b_n(x,y) = \frac{m\psi_n'(y)\psi_n(x) - \psi_n(y)\psi_n'(x)}{m\psi_n'(y)\xi_n(x) - \psi_n(y)\xi_n'(x)} \tag{2.12}$$

The prime denotes differentiation with respect to x, with $x = 2\pi r/\lambda$ being the *size parameter*, a measure for the relation between the particle size and the wavelength of the incoming light. $y = x \cdot m$ with m as the complex refractive index of the particle. ψ_n and ξ_n are related to a spherical Bessel and Hankel function, respectively. π_n

and τ_n in Equations (2.9) and (2.10) are the *Mie angular functions*

$$\pi_n(\cos\Theta) = \frac{1}{\sin\Theta} P_n(\cos\Theta) \tag{2.13}$$

$$\tau_n(\cos\Theta) = \frac{d}{\partial\Theta} P_n(\cos\Theta) \tag{2.14}$$

with P_n as the associated Legendre polynomials of the first kind.

From the Mie coefficients a and b one can derive the extinction, scattering, and absorption cross-sections

$$\sigma_e = \frac{2\pi}{k^2} \sum_{n=1}^{\infty} (2n+1)\,\mathrm{Re}(a_n + b_n) \tag{2.15}$$

$$\sigma_s = \frac{2\pi}{k^2} \sum_{n=1}^{\infty} (2n+1)(|a_n|^2 + |b_n|^2) \tag{2.16}$$

$$\sigma_a = \sigma_e - \sigma_s \tag{2.17}$$

Additionally, from the scattering functions $S_1(\Theta)$ and $S_2(\Theta)$ the Mie scattering matrix and – particularly important in the context of the thesis – the Mie phase function can be calculated. The *Stokes vector* is a set of four values – the Stokes parameters I, Q, U, and V – introduced by George Gabriel Stokes in 1852 to describe the polarization state of electromagnetic radiation. I describes the total intensity, Q and U the two components of linear polarization, and V the circular polarization. Expressed by the time averages (identified by $\langle\,\rangle$) of the parallel and perpendicular components of the electric field vector $\mathbf{E}$, the Stokes parameters can be written as

$$I = \langle E_{\parallel} E_{\parallel}^{*} + E_{\perp} E_{\perp}^{*} \rangle \tag{2.18}$$

$$Q = \langle E_{\parallel} E_{\parallel}^{*} - E_{\perp} E_{\perp}^{*} \rangle \tag{2.19}$$

$$U = \langle E_{\parallel} E_{\perp}^{*} + E_{\perp} E_{\parallel}^{*} \rangle \tag{2.20}$$

$$V = i\langle E_{\parallel} E_{\perp}^{*} - E_{\perp} E_{\parallel}^{*} \rangle \tag{2.21}$$

Let (I_0, Q_0, U_0, V_0) and (I_s, Q_s, U_s, V_s) be the Stokes vectors of the incoming and scattered radiation, respectively. Then

$$\begin{pmatrix} I_s \\ Q_s \\ U_s \\ V_s \end{pmatrix} = \frac{\sigma_s}{4\pi R^2} \mathbf{P} \begin{pmatrix} I_0 \\ Q_0 \\ U_0 \\ V_0 \end{pmatrix} \tag{2.22}$$

where

$$\mathbf{P} = \begin{pmatrix} P_{1,1} & P_{1,2} & 0 & 0 \\ P_{1,2} & P_{1,1} & 0 & 0 \\ 0 & 0 & P_{3,3} & P_{3,4} \\ 0 & 0 & -P_{3,4} & P_{3,3} \end{pmatrix} \tag{2.23}$$

is the Mie *scattering matrix* for spherical scatterers. Each of the four independent elements of $\mathbf{P}$ can be expressed by the scattering functions $S_1(\Theta)$ and $S_2(\Theta)$:

$$P_{1,1} = \frac{2\pi}{k^2\sigma_s}(S_1S_1^* + S_2S_2^*) \tag{2.24}$$

$$P_{1,2} = \frac{2\pi}{k^2\sigma_s}(S_2S_2^* - S_1S_1^*) \tag{2.25}$$

$$P_{3,3} = \frac{2\pi}{k^2\sigma_s}(S_2S_1^* + S_1S_2^*) \tag{2.26}$$

$$P_{3,4} = \frac{2\pi}{k^2\sigma_s}(S_2S_1^* - S_1S_2^*) \tag{2.27}$$

The star denotes the complex conjugate. $P_{1,1}$ – later simply denoted as $P(\Theta)$ – is the *phase function*, a very important quantity in this work. Another quantity used in this work for the retrieval of stratospheric aerosol extinction profiles is the *asymmetry parameter*, defined as the first moment of the phase function $P_{1,1}$,

$$\begin{aligned} g &= \int_{4\pi} P_{1,1}(\Theta)\cos\Theta \mathrm{d}\Omega \\ &= 2\sum_{n=1}^{\infty}\left[\frac{n(n+2)}{n+1}\mathrm{Re}(a_n a_{n+1}^* + b_n b_{n+1}^*) + \frac{2n+1}{n(n+1)}\mathrm{Re}(a_n + b_n^*)\right] \end{aligned} \tag{2.28}$$

which is a qualitative indication of the main direction of scattering. $g = 1$ means totally forward scattering, $g = 0$ corresponds to equal forward and backward scattering, and $g = -1$ to all backward scattering.

As explained in the previous Section 1.4, an air parcel in the atmosphere rarely contains aerosols with a single radius, but particles of various sizes whose radii are typically distributed lognormally. Thus, the results from the Mie theory have to be applied to such particle ensembles.

Given a particle size distribution *n(r)*, the averaged extinction cross-section $\bar{\sigma}_e$

within a radius interval $[r_{min}, r_{max}]$ is

$$\bar{\sigma}_e = \frac{\int_{r_{min}}^{r_{max}} \sigma_e(r)\, n(r)\, \mathrm{d}r}{\int_{r_{min}}^{r_{max}} n(r)\, \mathrm{d}r} \tag{2.29}$$

Multiplication with the total particle number $N = \int_{r_{min}}^{r_{max}} n(r)\, \mathrm{d}r$ gives the volume *extinction coefficient* β_e. The averaged scattering and absorption cross-sections and volume coefficients are calculated in the same way.

Similarly, the averaged scattering matrix elements are

$$\bar{P}_{i,j}(\Theta) = \frac{\int_{r_{min}}^{r_{max}} P_{i,j}(\Theta, r)\, n(r)\, \mathrm{d}r}{\int_{r_{min}}^{r_{max}} n(r)\, \mathrm{d}r} \tag{2.30}$$

with the phase function

$$\bar{P}(\Theta) = \frac{2\pi}{k^2 \beta_s} \int_{r_{min}}^{r_{max}} \left[S_1 S_1^* + S_2 S_2^* \right] n(r)\, \mathrm{d}r \tag{2.31}$$

The *single scattering albedo*

$$\omega_0 = \frac{\beta_s}{\beta_e} = \frac{\beta_s}{\beta_s + \beta_a} \tag{2.32}$$

gives the fraction of light which is scattered and absorbed in a single scattering event. A value of 1 would mean that no absorption takes place in the particle.

Figure 2.1 shows the Mie phase functions for the two particle size modes r_1/σ_1

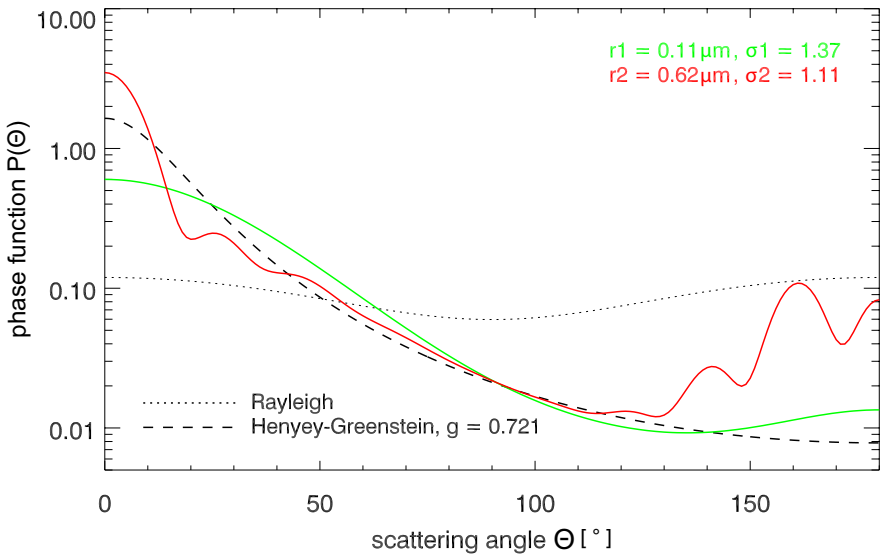

Figure 2.1: Mie phase functions for $\lambda = 450\,\mathrm{nm}$ and median radii of 0.11 µm (green) and 0.62 µm (red) with a distribution width of 1.37 and 1.11, respectively. The dashed curve shows the Henyey-Greenstein approximation with an asymmetry parameter of 0.712, the dotted curve the Rayleigh phase function. All phase functions are normalized to 1.

for the background case (right panel of Figure 1.4) and r_2/σ_2 for the volcanic influence (left panel of Figure 1.4), assumed to be separated from each other in two monomodal lognormal particle size distributions. The Mie phase function depends strongly on the PSD in such a way that a larger median radius generates a larger forward and backward scattering peak, while a broader distribution width smoothes the curve and removes the fine structures seen in the red curve. As a result, the Mie phase functions for the small background and the large volcanic particle mode differ drastically. The dashed curve shows a parameterization introduced by Henyey and Greenstein (1941), which is often used to simplify complicated Mie phase functions and which is given by:

$$P(\Theta) = \frac{1}{4\pi} \frac{(1-g^2)}{(1+g^2-2\,g\,\cos\,\Theta)^{3/2}} \tag{2.33}$$

where g is the asymmetry parameter derived in Equation (2). In this case, g is 0.712 because this is a typical value for stratospheric aerosols which is used later in this work (see Sections 6.1.1, 7.1, and 8.1).

The dotted curve shows the Rayleigh phase function which is a limiting case of the Mie phase function for scattering by particles much smaller than the wavelength of the incoming light (size parameter $x \ll 1$), such as air or trace gas molecules with respect to visible sunlight. The Rayleigh pase function is

$$P(\Theta) = \frac{3}{4}(1 + \cos^2 \Theta). \tag{2.34}$$

Mie phase functions in general have a strong forward scattering peak which is more pronounced for larger particles, while the Rayleigh phase function is much more isotropic. The Henyey-Greenstein approximation (in this thesis often abbreviated with “HG”) gives a rough estimate of the Mie phase function, but is not capable to reproduce finer structures, especially in the backscattering part of the phase function.

Note that the scattering cross-sections (Equation (2.16)) is dependent from the wavenumber k and the size parameter x and thus from the wavelength λ. This wavelength dependence can be expessed by the simple equation

$$\sigma_s(\lambda) = const \cdot \lambda^{-\alpha} \tag{2.35}$$

where α denotes the *Ångstrøm exponent*. While a typical value for the scattering of visible light by stratospheric sulfate droplets is $\alpha = 1.5$, the Ångstrøm exponent for Rayleigh scattering is $\alpha = 4$. One task of the algorithm used in this work is to distinguish between radiation Rayleigh-scattered by gas molecules and radiation Mie-scattered by spherical aerosol particles.

3 SCIAMACHY on Envisat

3.1 The satellite Envisat

On 01 March 2002, the European environmental research satellite Envisat was launched by the European Space Agency (ESA) on an Ariane-5 rocket from the Guiana Space Centre near Kourou in French Guiana. It was injected into a sun-synchronous polar orbit at a mean altitude of 799,8 km with a descending node equator crossing time of 10:00 local time and an inclination of 98.55°. The satellite orbits the Earth in 100.6 minutes with a repeat cycle of 35 days, leading to $14\ ^{11}/_{35}$ orbits per day and 501 orbits in one repeat cycle. With a mass of 8140 kg – including 314 kg of fuel and a payload mass of 2050 kg – and dimensions of 26 m x 10 m x 5 m it was the largest civilian Earth observation satellite ever put into space. The combination of 10 instruments onboard Envisat made it Europe's most ambitious Earth observation mission. These instruments are the Advanced Synthetic Aperture Radar (ASAR), the Radar Altimeter 2 (RA-2), the MicroWave Radiometer (MWR), the Doppler Orbitography and Radiopositioning Integrated by Satellite (DORIS), the MEdium Resolution Imaging Spectrometer (MERIS), the Advanced Along Track Scanning Radiometer (AATSR), the Global Ozone Monitoring by Occultation of Stars (GOMOS), the Michelson Interferometer for Passive Atmospheric Sounding (MIPAS), the Laser RetroReflector (LRR), and the SCanning Imaging Absorption spectroMeter for Atmospheric CHartographY (SCIAMACHY), which is used in this study. With GOMOS and MIPAS, SCIAMACHY forms the atmospheric chemistry mission. Figure

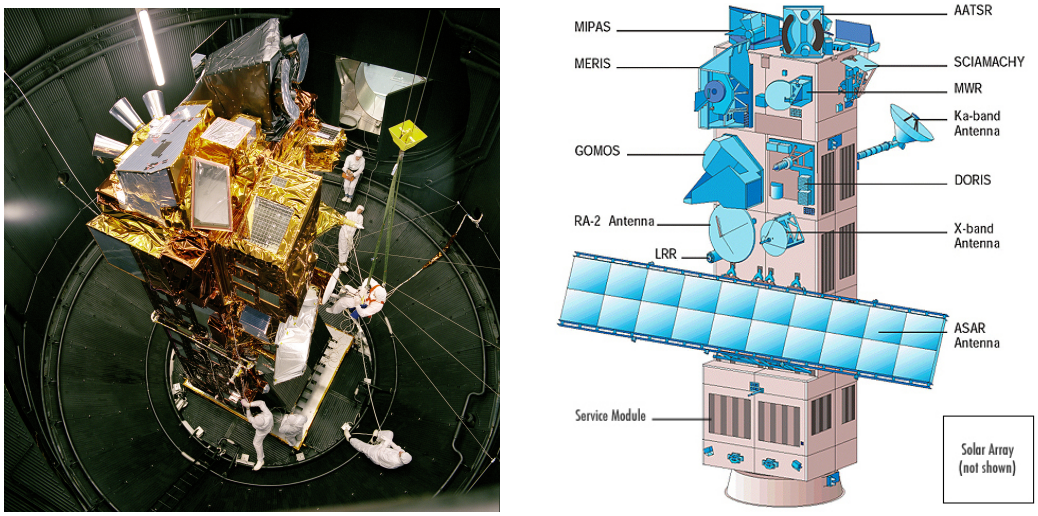

Figure 3.1: Envisat in ESTEC's (European Space Research and Technology Centre) test facility (left) and its instruments (right) (courtesy: ESA).

3.1 shows a situation during the test phase of the satellite (left panel) and a sketch of Envisat with the positions of the instruments (right panel). The Envisat mission abruptly ended on 08 April 2012 as a consequence of a major spacecraft failure of unknown origin. ESA formally announced the end of Envisat's mission on 09 May 2012.

3.2 The SCIAMACHY instrument

SCIAMACHY (greek $\sigma\kappa\iota\alpha\mu\alpha\chi\eta$, analogously "fighting shadows") was a double monochromator comprising a dispersing prism and grating spectrometers observing the 214–2386 nm spectral range in 8 spectral channels passively measuring radiation transmitted through, scattered by and/or reflected by the atmosphere or the earth's surface. It was a joined German-Dutch-Belgian contribution to Envisat. To achieve the manifold mission objectives – improving the knowledge of the atmosphere in general and its response to natural and anthropogenic activity and the related

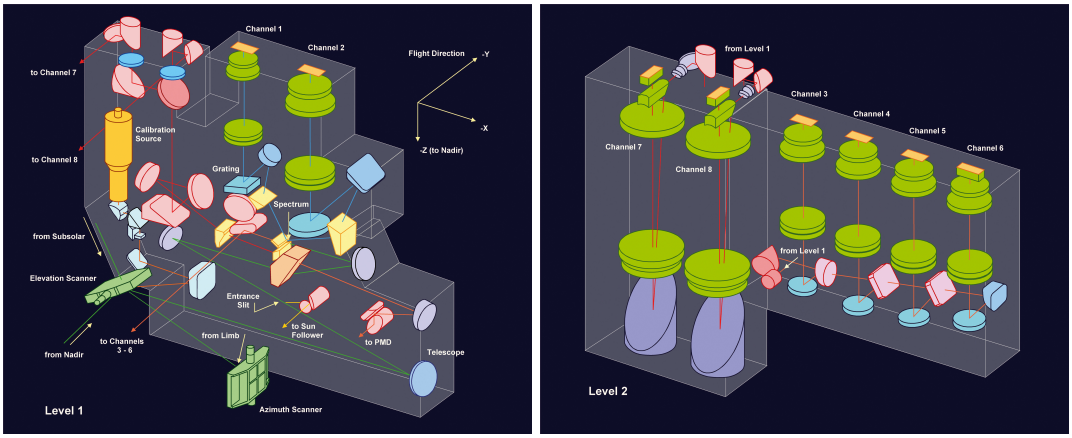

Figure 3.2: Optical configuration of SCIAMACHY (figure from Gottwald and Bovensmann (2011)).

processes such as stratosphere-troposphere-exchange or the impact of anthropogenic and natural sources on tropospheric ozone, air quality, and global warming, to mention only a fraction of them – SCIAMACHY delivered a multitude of parameters characterising the system Earth-Atmosphere-Sun (Gottwald and Bovensmann, 2011). Next to a wide range of trace gases (O_2, O_3, O_4 NO, NO_2, NO_3, CO, CO_2, HCHO, CH_4, H_2O, N_2O, SO_2, BrO, OClO) this includes information on clouds (including PSCs and NLCs), surface parameters, and aerosols.

3.2.1 Instrument design

Centerpiece of the instrument is the two-level Optical Assembly, where the incoming radiation in collected and converted into spectral information as output (Gottwald and Bovensmann, 2011). Figure 3.2 shows the different paths that the incoming light follows within the two levels of the instrument, dependent on wavelength and scan geometry (see below). By means of mirrors, the incoming radiation from the nadir, limb or subsolar port is directed to a predisperser prism and a geometrical channel seperator, where it is split and – depending on the spectral segment –

Channel #	Spectral range [nm]	Resolution [nm]	Temperature range [K]	Detector material
1	214 – 334	0.24	204.5 – 210.5	Si
2	300 – 412	0.26	204.0 – 210.0	Si
3	383 – 628	0.44	221.8 – 227.8	Si
4	595 – 812	0.48	222.9 – 224.3	Si
5	773 – 1063	0.54	221.4 – 222.4	Si
6	971 – 1773	1.48	197.0 – 203.8	InGaAs
7	1934 – 2044	0.22	145.9 – 155.9	InGaAs
8	2259 – 2386	0.26	143.5 – 150.0	InGaAs

Table 3.1: SCIAMACHY science channels.

directed by mirrors to the channels 1 and 2 on the same instrument level or the channels 3–8 on the second level. In Table 3.1 the 8 channels of SCIAMACHY are listed with the corresponding wavelength intervals, spectral resolution, temperature range and the detector material.

The channels 1–6 cover continuously and slightly overlapping the spectral region from 214–1773 nm, from ultraviolet (UV) to short-wavelength infrared (SWIR). Channel 7 and 8 cover two separated wavelength segments in the SWIR. While the channels 1–5 use standard Silicon (Si) photodiode arrays, the channels 6–8 use Indium Gallium Arsenide (InGaAs) detectors to be sensitive to radiation with wavelengths above 1700 nm. All 8 channels are cooled to reach a channel-dependent signal-to-noise performance, with lowest temperatures in the SWIR channels 7 and 8. Overall the detector performance is characterized by low noise and high instrument throughput, resulting in a high signal-to-noise ratio required for the retrieval of the targeted geophysical parameters (Gottwald and Bovensmann, 2011). Additionally, for polarization correction the Optical Assembly contains Polarization Measurement

Devices (PMDs) measuring the polarization perpendicular to the SCIAMACHY optical plane in six broadband channels between 310 and 2400 nm and the 45° component of the light between 800 and 900 nm. An on-board calibration unit consisting of a White Light Source (WLS) and Spectral Line Source (SLS) maintains a high spectral stability and high relative radiometric accuracy over the mission's lifetime.

3.2.2 Scan geometries

Figure 3.3 shows a sketch of SCIAMACHY's Total Clear Field of View (TCFoV) and scanning geometries.

In Nadir mode, the instrument Instantaneous Line-of-Sight (ILoS) is pointed towards the subsatellite point, probing the atmosphere directly under the instrument with a scan duration of 4 s across track, followed by a 1 s backscan. At one measuring point ("state") this is repeated for either 65 or 80 s, depending on the orbital region. The across track swath size is 960 km, typical spatial resolution is about 30 km (along track) x 60 km (across track).

In Limb mode, SCIAMACHY scans the atmosphere in flight direction tangentially to the earth's surface from ground to about 100 km altitude, measuring sunlight scattered by the atmosphere. The swath size in each tangent height is – as in nadir mode – 960 km, corresponding to a scan duration of 1.5 s. The distance between instrument and TP is approximately 3280 km. After each horizontal scan the LOS is stepped upwards by about 3.3 km at the tangent point to a total of 100 km altitude with a geometrical field of view of 2.6 km in vertical direction and 110 km in horizontal direction (Gottwald and Bovensmann, 2011). For more details, see Chapter 4.

The composition of the nadir and limb scans during one orbit – the limb-scanned atmospheric volume is overflown by the satellite for nadir scanning with a delay

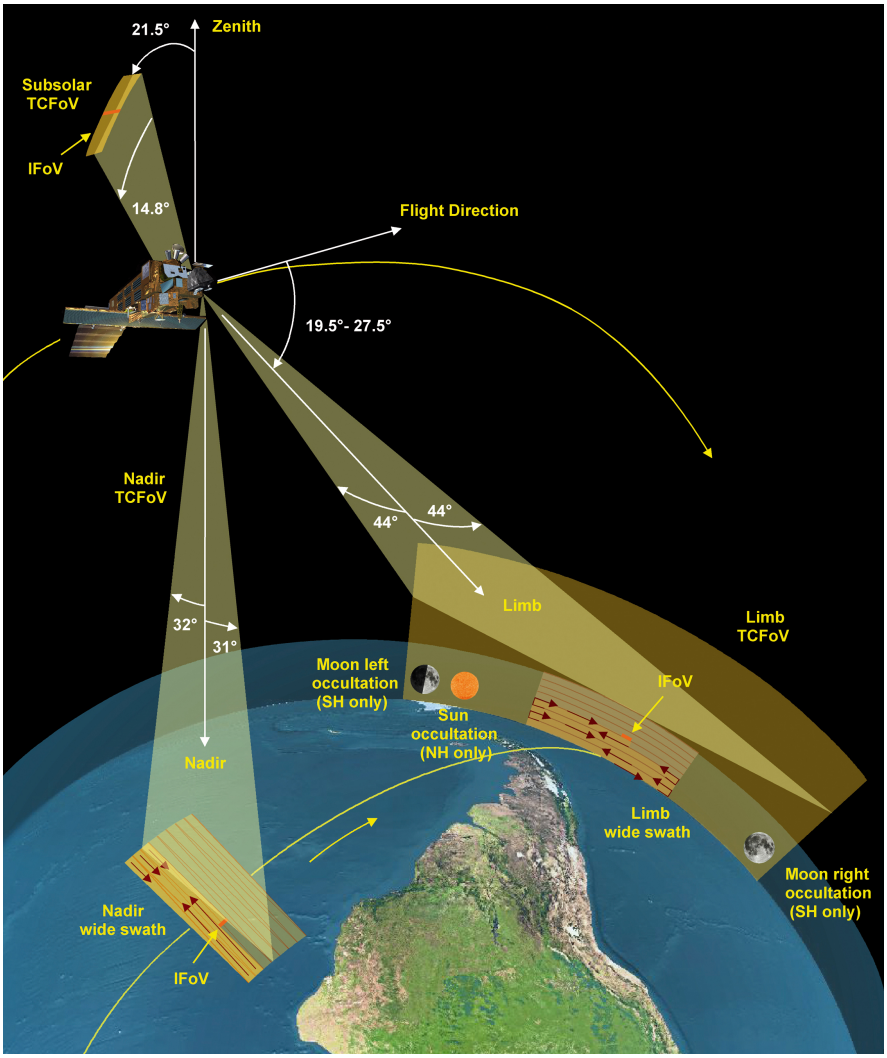

Figure 3.3: Sketch of SCIAMACHY's TCFoV (Total Clear Field of View) and observation geometries (courtesy: DLR-IMF).

of approximately 8 minutes – allows a combination of both scanning geometries, the so-called limb-nadir-matching, which enables the retrieval of tropospheric columns of various atmospheric components by subtracting the stratospheric column determined by the limb scan from the total nadir column.

Similar to the limb mode is the geometry of the solar and lunar occultation mode. In occultation mode, SCIAMACHY "looks" tangentially to the earth's surface through

the atmosphere directly into the sun or the moon. The absorption on the way through the atmosphere causes changes in the well-known spectrum of sun and moon which can be used to interprete the composition of the atmosphere. In both solar and lunar occulation mode, the atmosphere is scanned from approximately 17 to 100 km altitude. Because of the sun-fixed orbit of Envisat and the forward viewing direction of SCIAMACHY, it can only perform solar occultation measurements with the rising sun once per orbit while the moon is only visible quite irregularly within one week per month in the southern hemisphere. Therefore solar occultation measurements are limited to a small latitudinal range between 50°N and 70°N while lunar occultation covers large regions of the southern hemisphere from about 20°S to 90°S (Noël et al., 2002).

4 Limb geometry

The relatively new limb-scatter technique is similar to the occultation technique used for the first satellite measurements of the stratospheric aerosol layer in the early seventies, but with substantial differences. As in occultation mode, the instrument line-of-sight (LOS) is directed tangentially to the Earth's surface through the atmosphere, but not at the sun but at a tangent altitude in the name-giving atmospheric limb. Thus, the atmospheric state is not interpreted from the transmitted fraction of the sunlight (or moon-/starlight in case of lunar/stellar occultation), but from the spectrum of sunlight that is Rayleigh- and Mie-scattered into the field of view (FOV) of the instrument. The limb-scatter technique is able to combine a high vertical resolution with a good global coverage, but at the cost of the necessity for complicated radiative transfer calculations and inversion techniques which are presented in Part II of this work. The increase of computing power in the last decades reduced the relevance of this disadvantage and enabled an effective use of this measurement geometry. The general goal of this measurement technique is to obtain information on the atmospheric state (in this case the aerosol extinction) of the air parcel at the tangent point of successive altitude levels, assembling to a vertical profile of a parameter above a point at the Earth's surface. The tangent point (TP) is defined as the point of the LOS with the shortest distance to the surface below, the tangent height (TH) is the corresponding distance between the TP and surface. The latitude and longitude of the point at the suface directly below the TP are used as the geolocation of the measurement.

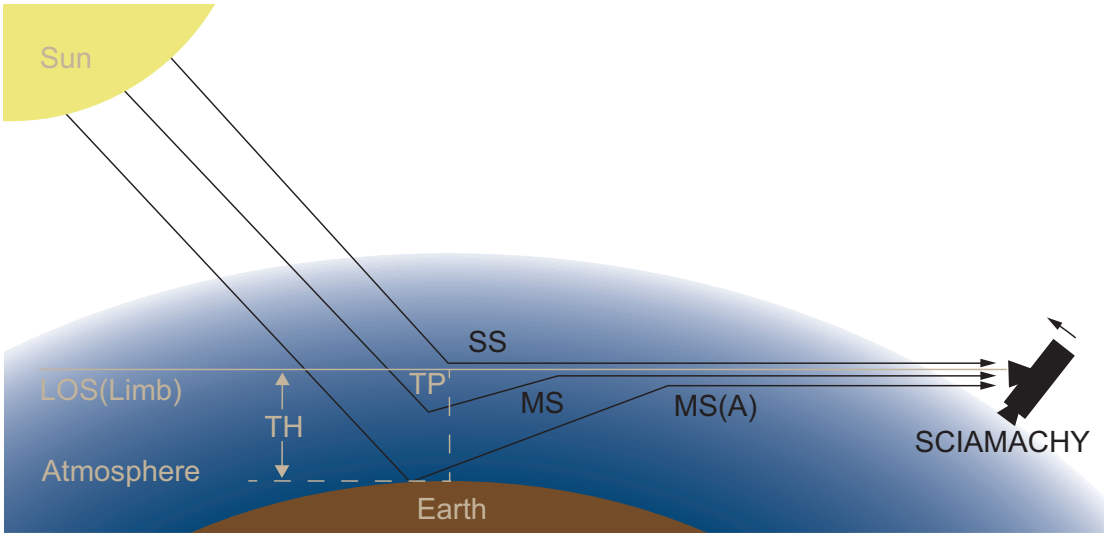

Figure 4.1: Sketch of the limb-scattering technique.

Figure 4.1 shows a sketch of the limb-scatter technique. The radiance measured in limb mode consists of a single-scattered ("SS" in Figure 4.1) and a multiple-scattered ("MS") fraction whose percentaged contribution to the measured radiance depends on the measurement geometry (in particular the solar zenith angle) and atmospheric and surface parameters (in particular the ground albedo). In the SS case, solar radiation is scattered by particles in the LOS directly into the instrument. In the MS case, the photons are scattered multiple times by atmosphere and/or surface before measured by the instrument, containing information from outside the LOS – usually from the denser air below – and thus outside the air parcel in the focus of investigaton. The multiple-scattered fraction normally also includes radiation reflected by the Earth's surface, modified by the ground albedo ("MS(A)"). Hence it is desirable to maximize the single-scattered portion of the measured radiance, in particular to minimize the influence of the ground albedo. Therefor the atmosphere should ideally be optically thin in the LOS to make sure that most of the single-scattered light reaches the instrument and is not scattered out of the LOS or

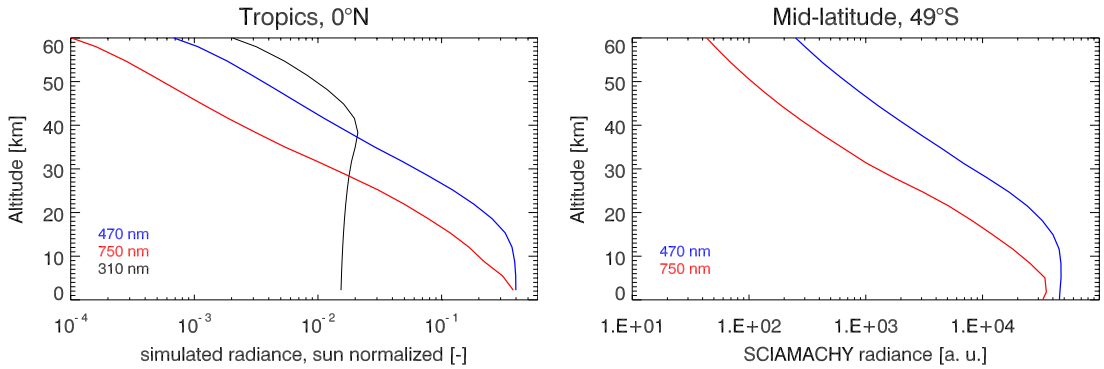

Figure 4.2: Sun normalized simulated SCIAMACHY radiance at three wavelengths for a tropical geometry (left panel) and real SCIAMACHY measurements at two wavelengths at a southern hemispheric mid-latitude (right panel).

absorbed in the LOS. Below the measurement altitude – in our case the stratosphere – an optically thick atmosphere is useful for limb measurements, because in this case information from below – in our case the troposphere and the surface – is filtered out to a high percentage. Due to the curvature of the earth's atmosphere, the optically thickest part of the LOS is the region around the tangent point (TP), which has the advantage that most of the information in LOS comes from the air parcel around the TP.

Figure 4.2 shows exemplarily the limb radiance profiles for the wavelengths 750, 470, and 310 nm. In the left panel, simulated radiances for the three wavelengths are shown for a tropical geometry, the right panel shows measured SCIAMACHY radiances (in photons/s in a wavelength interval of ± 2 nm) for 750 and 470 nm for a southern hemispheric mid-latitude geometry (50°S) from 02 February 2004. The so-called "knee" appears at altitudes where the atmosphere becomes optically thick. Below that altitude, information gets lost by scattering out of and absorption in the LOS. Retrieving atmospheric parameters from limb measurements below this altitude would be difficult. In the case of $\lambda = 310$ nm this "knee" appears at approximately 38 km due to absorption in the Huggings and Hartley bands of

stratospheric O_3. For stratospheric measurements outside these two absorption bands, the shortest possible wavelength is approximately 400 nm because of the proportionality of Rayleigh scattering to λ^{-4} (see Section 2). The two wavelengths used in this work – the blue and red curve in Figure 4.2 – are suitable from this point of view.

SCIAMACHY puts the limb-scatter technique into practice as follows. On the sunlit side of the earth, approximately 25 limb scans ("states") per orbit are executed. A typical SCIAMACHY limb scan starts with a horizontal scan approximately 4 km below the horizon from the right to left side in flight direction. The total swath width at the tangent point is 960 km with a total integration time of 1.5 s, divided into four pixels of 240 km width each. Afterwards the ILoS is moved upward by approximately 3.3 km and the next horizontal scan is executed in opposite direction. This is repeated for a total of 30 horizontal scans up to an altitude of approximately 90 km. After the last horizontal scan the ILoS is moved to an altitude of 250 km to obtain a dark current measurement for calibration. During the scan from bottom to top the satellite moves with a speed of approximately 27,000 km/h, leading to a shift in the geolocation of subsequent tangent points. Thus, the ground pixel size of each of the four adjacent limb profiles per state ("horizontal readouts") is approximately 400 km in flight direction and 240 km across flight direction.

In Figure 4.3 the geometry that describes the limb-scattering is sketched. In the SCIAMACHY data set a limb measurement is described sufficiently by the geolocation below the TP and the solar geometry at the TP, namely the solar zenith angle (SZA@TP) and the solar azimuth angle relative to the LOS of the instrument (SAA@TP). The line-of-sight angle is the angle between the LOS and the local zenith. The single scattering angle (SSA) which is crucial when interpreting the aerosol phase function (SSA$\equiv \Theta$ in Section 2) can be calculated from

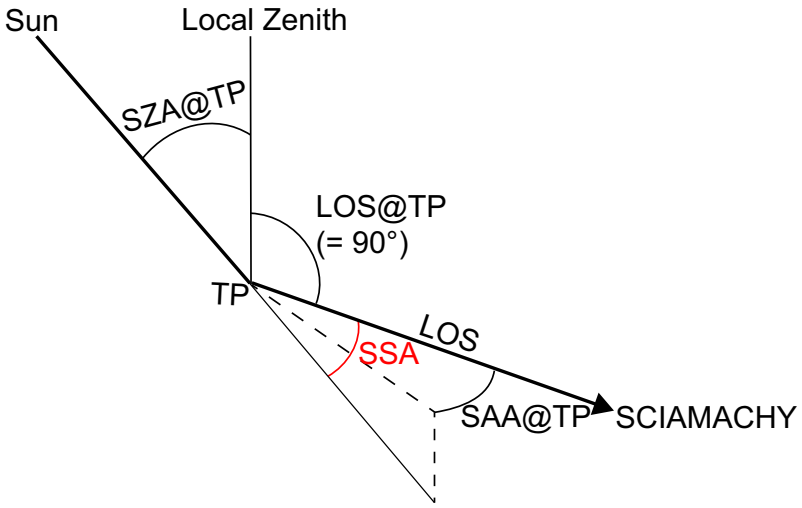

Figure 4.3: Sketch of the limb-scatter geometry with the solar angles at the tangent point (TP).

$$\begin{aligned}\cos(SSA) = &\cos(SZA@TP)\cdot\cos(LOS@TP)\\ &+\sin(SZA@TP)\cdot\sin(LOS@TP)\cdot\cos(SAA@TP)\end{aligned} \tag{4.1}$$

Since the line-of-sight angle at the TP (LOS@TP) is always 90°, Equation (4.1) simplifies to

$$\cos(SSA) = \sin(SZA@TP)\cdot\cos(SAA@TP) \tag{4.2}$$

The fixed equator crossing time of SCIAMACHY leads to a strong dependence of the SZA and the SSA from latitude. From one orbit to the next both angles are similar at a fixed latitude, changing slowly with the position of the sun throughout the year. Figure 4.4 shows the SZA and SSA for all states of a sample orbit at 21 December, 21 March, 21 June, and 21 September, respectively, averaged in 10° latitude bins from 90°N to 90°S. Measurements with a SZA>87° are not included as these are

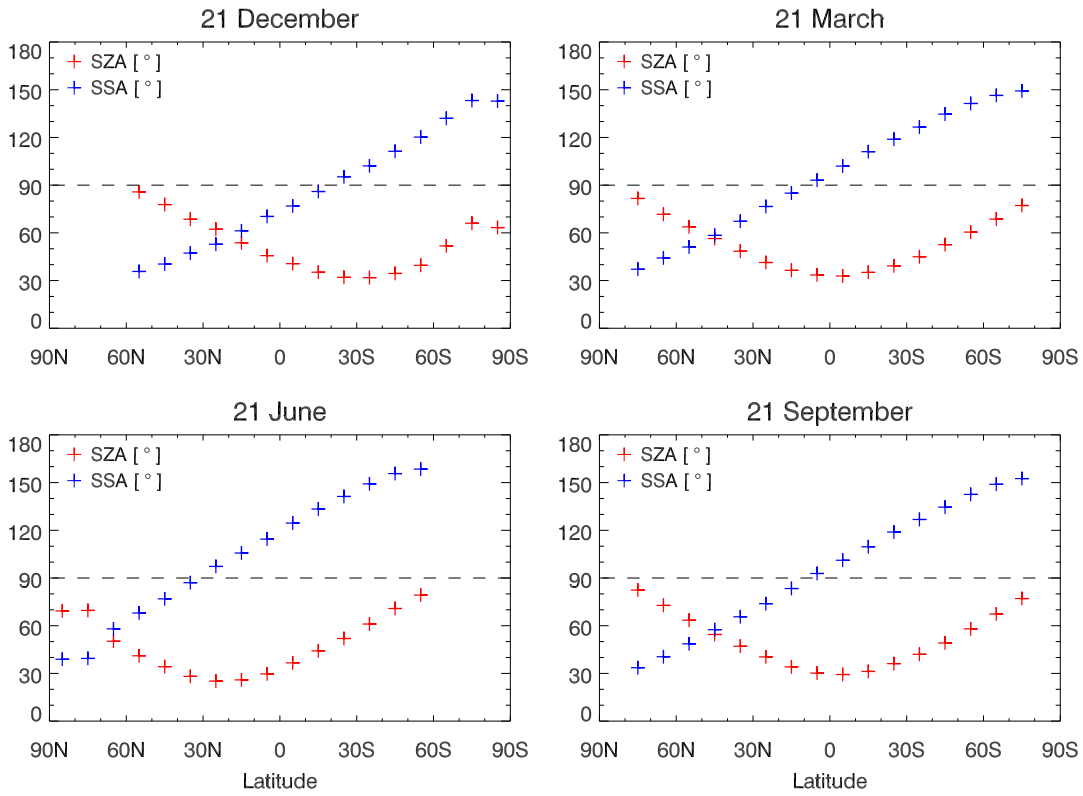

Figure 4.4: Solar zenith angle (SZA, red) and single scattering angle (SSA, blue) for the winter solstice, spring equinox, summer solstice, and summer equinox. Each cross is centered in a 10° latitude bin in which the corresponding measurement angles of a sample orbit at that particular day are averaged. The horizontal dashed line denotes 90° for distinguishing between forward and backward scattering with respect to the SSA and to show the horizon with respect to the SZA.

also filtered out later in the retrieval. At winter and summer solstice (panels a and c) the winter poles are in the dark, thus no limb radiance measurements can be executed. The general picture is similar for all seasons but both curves are shifted to the summer hemisphere thoughout the year due to the dependence of the SSA on the SZA (see Equation (4.2)). At low state numbers at high northern latitudes SCIAMACHY starts with the limb measurements when the first light reaches the instrument. For the stratospheric aerosol retrieval we use the first measurements at which the sun is slightly above the horizon at the TP (SZA≥87°). The SZA

reaches a minimum of roughly 30° at a latitude between 30°N and 30°S depending on the season and grows south of this latitude until sunset. At the summer poles the instrument is illuminated even while on the ”back side” of the Earth, thus averaging over latitudes from 80–90° leads to the somewhat irregular behaviour of the SZA and the SSA seen at this latitude bin. The SSA is small for high northern latitudes (30–40°), i.e., the sunlight is forward-scattered into the instrument. During the course of the orbit, the SSA grows monotonically reaching values far in the backscattering region (SSA>150°) in the polar southern hemisphere. As we will see leater in this work, this asymmetrical behaviour of the SAA strongly affects the retrieval of stratospheric aerosol extinction.

Part II

Methodology

5 Retrieval algorithm

5.1 Algorithm description

A main task to establish a retrieval method for stratospheric aerosols is to distinguish between the portion of light Rayleigh-scattered by the atmosphere's gaseous constituents and the portion Mie-scattered by aerosols and clouds, i.e., to separate the aerosol signal in the limb-scattered radiance from the signals of all other atmospheric constituents as good as possible. To achieve this, we use a color-index approach applied to SCIAMACHY limb radiance profiles at two wavelengths to derive the measurement vector required for the retrieval, following the method previously used by Bourassa et al. (2007). The two wavelengths to be combined in the color-index are $\lambda_l = 750\,\text{nm}$ as the long wavelength and $\lambda_s = 470\,\text{nm}$ as the short wavelength. As shown in Figure 4.2, for these wavelengths the atmosphere is sufficiently optically thin in the stratosphere, and the "knee" altitude is below the tropopause. Spectral windows with weak atmospheric absorption are preferred for the wavelength selection in order to avoid retrieval errors caused by incorrect knowledge of absorber profiles.

Figure 5.1 depicts spectra of the SCIAMACHY channel 3 (top panel) and 4 (bottom panel) limb radiance at tangent heights from -2 to 58 km, normalized with the 37 km spectrum. The vertical grey bars mark λ_l and λ_l. For the synthetic retrievals, discrete wavelengths are used, but for the retrieval from real SCIAMACHY limb radiances we average over a wavelength interval of $\pm 2\,\text{nm}$ to improve the signal-

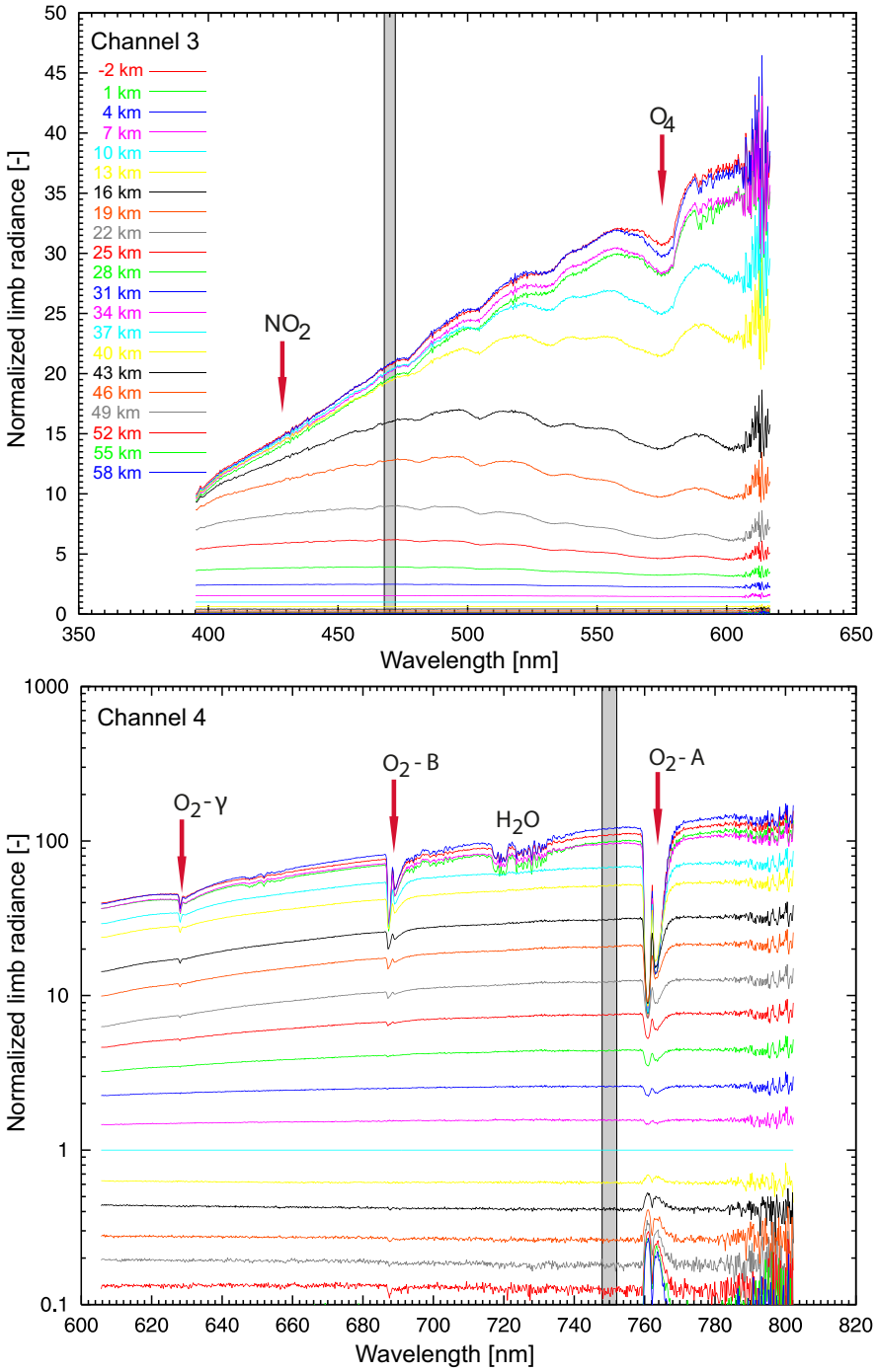

Figure 5.1: Calibrated limb spectra of the SCIAMACHY channels 3 (top panel) and 4 (bottom panel) for tangent heights between −2 and 58 km. The limb radiances at the tangent heigths listed in the legend in the top panel are normalized by division with the spectrum at 37 km. The vertical grey bars mark the wavelength intervals used in this work, 470±2 nm and 750±2 nm (figure provided by Kai-Uwe Eichmann, IUP Bremen).

to-noise ratio (see also Section 6.3). λ_s falls between an NO_2 and the Chappuis absorption band which can be seen as a broadband structure in the lower tangent heights between approximately 475 nm and the edge of the channel at 628 nm. λ_l is just below the O_2 *A*-band and above a weak tropospheric water vapour band.

λ_s and λ_l are combined in a 2-step approach to accentuate the aerosol signal. First we normalize the limb radiance at each tangent height $I^{\lambda}(TH)$ with the radiance at a reference tangent height TH_{ref} of the same limb radiance profile for both wavelengths separately:

$$I_N^{\lambda}(TH) = I^{\lambda}(TH)/I^{\lambda}(TH_{ref}) \tag{5.1}$$

where subscript N indicates normalization.

This technique is adapted from trace gas retrievals (e.g., Flittner et al., 2000, von Savigny, 2003) and adjusted for the aerosol retrieval. It has two advantages: first, an absolute calibration of the limb radiances is not required. An error causing the same relative contribution to the radiance at all tangent height is cancelled out by this procedure. Furthermore, von Savigny (2003) showed that the tangent height normalization leads to a reduced sensitivity to errors in the assumed ground albedo. This is based on the assumption that the fraction of ground-reflected sunlight in the limb radiance is similar at all tangent heights, including the reference tangent height. A reference tangent height (TH_{ref}) of 35 km was chosen because at this point (and above) the aerosol loading in the atmosphere is small under background conditions due to evaporation of sulfate droplets (see Section 1.2.1). Above that tangent height the SCIAMACHY limb measurements are potentially contaminated by external or "baffle" straylight, a potentially large error which would be imported into the complete profile by normalization with such a contaminated tangent height.

Figure 5.2 illustrates the effect of the tangent height normalization on limb radiance profiles for a polar and a tropical scenario using simulated radiance profiles

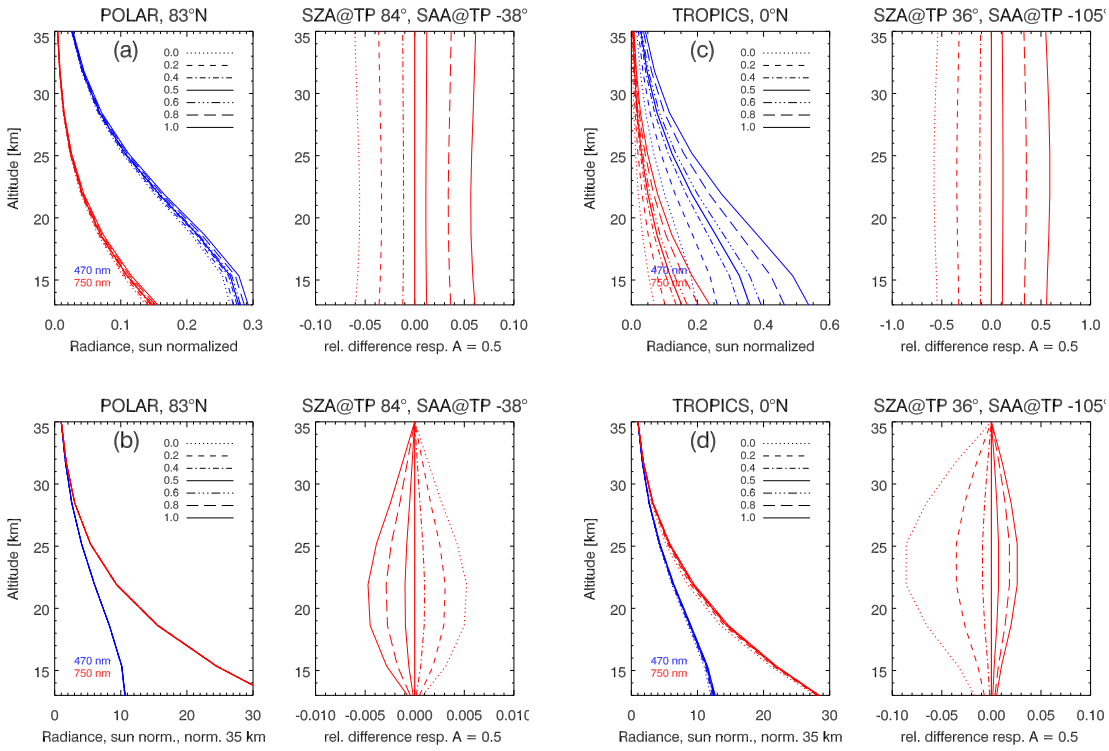

Figure 5.2: Effect of the tangent height normalization: simulated radiance for $\lambda = 470\,\text{nm}$ (blue) and $\lambda = 750\,\text{nm}$ (red) with seven different ground albedos. Left two panels: polar geometry (83°N) without (a) and with (b) tangent height normalization; right two panels: tropical geometry (0°) without (c) and with (d) tangent height normalization. Relative deviations with respect to an albedo of 0.5 for $\lambda = 750\,\text{nm}$ are shown on the right.

for $\lambda_s = 470\,\text{nm}$ (blue) and $\lambda_l = 750\,\text{nm}$ (red) with 7 different ground albedos. For the two latitudes 83°N and 0°, respectively, typical SCIAMACHY geometries have been simulated, with solar zenith angles at tangent point (SZA@TP) of 84° and 36°, respectively, and solar azimuth angles at tangent point (SAA@TP) of 38° and 105°, respectively (see Table 5.1, compare also with Figure 4.4). The modified ECSTRA (Extinction Coefficient for STRatospheric Aerosol, (Fussen, 1999)) profiles for the two latitudes have been used as aerosol extinction profile (see Section 6.3.1).

The unnormalized radiance profiles for the two latitudes (panels a and c of Figure 5.2) show a much larger impact of the ground albedo at the equator (note the

Latitude	SZA	SAA	SSA
83°N	84°	38°	38°
40°N	48°	60°	68°
0°	36°	105°	99°
40°S	58°	145°	134°
75°S	88°	155°	155°

Table 5.1: Typical SCIAMACHY solar zenith angle (SZA), solar azimuth angle (SAA), and single scattering angle (SSA) at the tangent point for five latitudes on 21 September.

factor of ten between the two abscissas of the difference plots). The reason for this is the smaller solar zenith angle in the tropics, which leads to a larger fraction of radiation reaching the earth's surface (beam denoted with "MS(A)" in Figure 4.1), being reflected from the surface and finally scattered into the field of view of the instrument. The tangent height normalization (panels b and d of Figure 5.2) leads to a significant decrease of the albedo influence by roughly a factor of 10 at both latitudes (note again the differently scaled abscissas). Interestingly, the sign of the difference changes for the polar geometry while it remains the same for the tropical geometry.

In a second step we combine the normalized limb radiance profiles at the two wavelengths in a color-index-ratio. Retrieving aerosol extinction profiles from limb radiance profiles at a single wavelength is also an option, but it relies on the assumption that the background Rayleigh atmosphere can be modelled perfectly. Any uncertainty in the neutral density would result in an error in the aerosol profile. To reduce this effect, it is suitable to use the ratio of a long to a short wavelength. Since the Ångstrøm exponent for Mie-scattering is highly variable, but for stratospheric aerosols generally significantly smaller than for Rayleigh scattering ($\alpha \approx 4$), wavelength pairing provides a suitable measurement vector for the retrieval

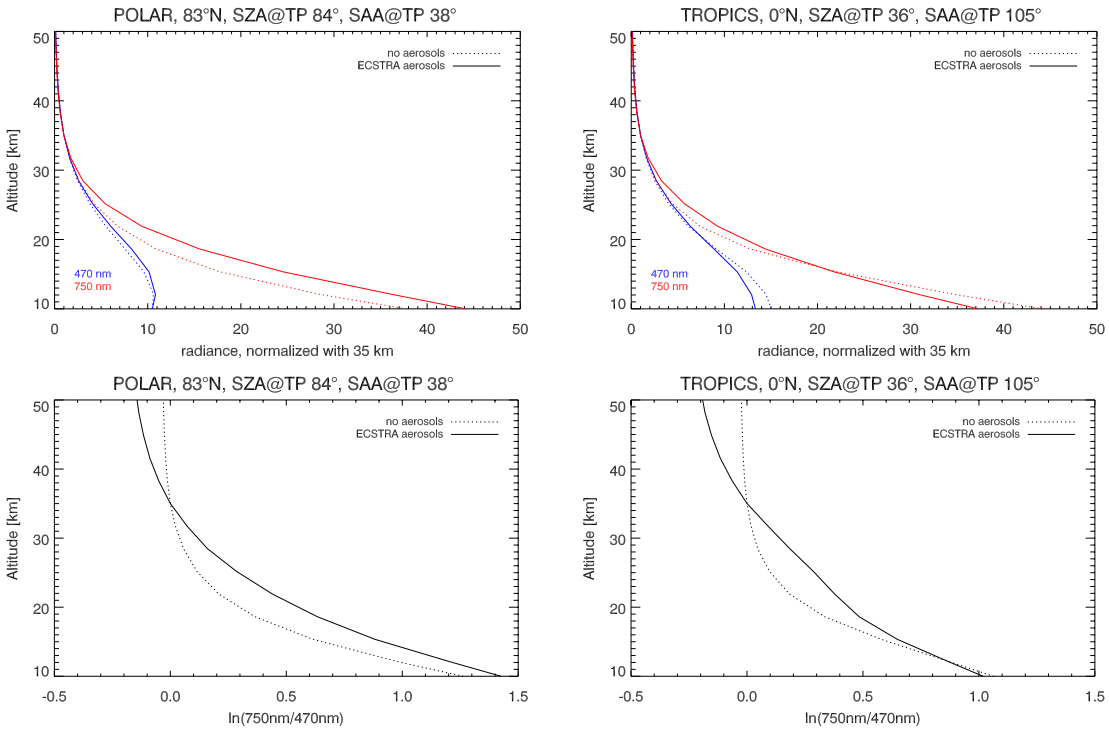

Figure 5.3: Effect of the color-index-ratio: simulated tangent height normalized radiance with ground albedo A = 0.3 for $\lambda_s = 470\,\text{nm}$ and $\lambda_l = 750\,\text{nm}$ (top panels) and the logarithm of the ratio of both (bottom panels). Left panels: polar geometry (83°N), right panels: tropical geometry (0°).

of stratospheric aerosols. Instead of the simple ratio of the two normalized limb radiance profiles, we use the natural logarithm of the ratio as the retrieval vector for the inversion (see below). As shown in previous studies (Klenk et al., 1982, Hoogen et al., 1999, Rozanov and Kokhanovsky, 2008), this approach improves the linearity of the inverse problem resulting in smaller linearization errors. The wavelength pairing can then be described mathematically as follows:

$$y(TH) = \ln\left(\frac{I_N^{\lambda_l}(TH)}{I_N^{\lambda_s}(TH)}\right) \tag{5.2}$$

Figure 5.3 shows the effect of the wavelength pairing for the two geometries used

above. At the top the tangent height normalized radiances of the two wavelengths are plotted separately with (solid lines) and without (dotted lines) aerosol loading. The bottom panels show the logarithms of the color-index-ratio as described above.

5.2 Retrieval scheme

After normalizing and pairing SCIAMACHY limb-scattered radiance spectra as described in the previous section, we need a mathematical method to retrieve the aerosol extinction profiles from this. The retrieval scheme we used is based on the Optimal Estimation Method (OEM) developed by Rodgers (2000). An important difference is the iteration procedure described at the end of this section. As during the complete thesis, vectors are written in boldface lower-case letters and matrices in boldface upper-case letters.

5.2.1 Formulation of the inverse problem

In Section 5.1 we explained the derivation and meaning of the so-called *measurement vector* $\mathbf{y}$ which contains the combined measured limb radiances at two different wavelengths at m tangent heights

$$\mathbf{y} = \left(\ln\left(\frac{I_N^{\lambda_l}(TH_1)}{I_N^{\lambda_s}(TH_1)}\right), \ln\left(\frac{I_N^{\lambda_l}(TH_2)}{I_N^{\lambda_s}(TH_2)}\right), \ldots, \ln\left(\frac{I_N^{\lambda_l}(TH_m)}{I_N^{\lambda_s}(TH_m)}\right)\right) \tag{5.3}$$

The *state vector* $\mathbf{x}$ contains the unknown aerosol extinction coefficient profile at a finite number of altitude levels n. The connection between both is described by the general equation

$$\mathbf{y} = \mathbf{f}(\mathbf{x}) + \epsilon \tag{5.4}$$

where **f** is the so-called *forward model* which contains the measurement physics. ϵ represents all kinds of errors of the measurement vector **y**.

If Equation (5.4) is linear, it can be expressed as

$$\mathbf{y} = \mathbf{K}\mathbf{x} + \epsilon \tag{5.5}$$

with the $m \times n$ matrix **K** as the *weighting function matrix* or *Jacobian matrix*. The elements of **K** are

$$K_{i,j} = \frac{\partial f_i(\mathbf{x})}{\partial x_j} \tag{5.6}$$

meaning that each of the m rows of **K** calculates one element of **y** from all n elements of **x** considering all other atmospheric parameters and the measurement geometry.

Since the inversion $\mathbf{x}(\mathbf{y})$ is usually ill-conditioned (since $m > n$) and thus no unique solution of this equation can be found, it is necessary to "choose" from all possible solutions. OEM provides different approaches how to do so in an objective mathematical manner. Here we use the so-called *Maximum a Posteriori Solution* (MAP). The equation for the inversion $\mathbf{x}(\mathbf{y})$ for the linear case is then

$$\mathbf{x} = (\mathbf{K}^{\mathrm{T}}\mathbf{S}_y^{-1}\mathbf{K} + \mathbf{S}_a^{-1})^{-1} + (\mathbf{K}^{\mathrm{T}}\mathbf{S}_y^{-1}\mathbf{y} + \mathbf{S}_a^{-1}\mathbf{x}_a) \tag{5.7}$$

This "optimal" solution for **x** can be interpreted as a weighted mean of the real measurement **y** and a virtual measurement $\mathbf{x}_a$ with the matrix weights $\mathbf{K}^{\mathrm{T}}\mathbf{S}_y^{-1}\mathbf{K}$ and $\mathbf{S}_a^{-1}$. In the framework of Rodgers' OEM, the *a priori* $\mathbf{x}_a$ with the *a priori covariance matrix* $\mathbf{S}_a$ represents knowledge of the desired atmospheric state before the measurement is made, e.g., seasonal and zonal statistics and covariances of aerosol extinction profiles. $\mathbf{S}_y$ is the covariance matrix of **y**, the *noise covariance matrix*. Equation (5.7) is very similar to the simpler scalar case with the two measurements x_1 and x_2 of an unknown x with the standard deviations σ_1 and σ_2

$$x = (1/\sigma_1^2 + 1/\sigma_2^2)^{-1}(x_1/\sigma_1^2 + x_2/\sigma_2^2) \tag{5.8}$$

For most inverse problems – including obtaining the unknown aerosol extinction profile from SCIAMACHY limb-scattered radiance measurements – Equation (5.4) is non-linear and thus the analytical method described above is not sufficient to find a solution. Therefore, Equation (5.4) is linearized with respect to a *reference state vector* $\mathbf{x}_0$ using the first two terms of the Taylor series expansion.

$$\mathbf{y} - \mathbf{f}(\mathbf{x}_0) = \frac{\partial \mathbf{f}(\mathbf{x})}{\partial \mathbf{x}}(\mathbf{x} - \mathbf{x}_0) + \epsilon \tag{5.9}$$

Using the a priori $\mathbf{x}_a$ as linearization point and

$$\mathbf{y}_a = \mathbf{f}(\mathbf{x}_a) = \mathbf{K}\mathbf{x}_a \tag{5.10}$$

Equation (5.9) can be written in a form similar to the linear case (Equation (5.5))

$$\mathbf{y} - \mathbf{y}_a = \mathbf{K}(\mathbf{x} - \mathbf{x}_a) + \epsilon, \tag{5.11}$$

A Gauss-Newton scheme can be employed to solve this equation iteratively,

$$\mathbf{x}_{i+1} = \mathbf{x}_a + (\mathbf{K}_i^{\mathrm{T}}\mathbf{S}_y^{-1}\mathbf{K}_i + \mathbf{S}_a^{-1})^{-1}\mathbf{K}_i^{\mathrm{T}}\mathbf{S}_y^{-1}(\mathbf{y} - \mathbf{y}_i + \mathbf{K}_i(\mathbf{x}_i - \mathbf{x}_a)) \tag{5.12}$$

with $\mathbf{S}_i = (\mathbf{K}_i^{\mathrm{T}}\mathbf{S}_y^{-1}\mathbf{K}_i + \mathbf{S}_a^{-1})^{-1}$ as the *solution covariance matrix*.

5.2.2 Solution in SCIATRAN

Within the retrieval algorithm of the model SCIATRAN (further described in the next chapter), the inversion is implemented with some differences compared to the original OEM by Rodgers. First, Equation (5.11) is used in form of

$$\hat{\mathbf{y}} = \mathbf{K}\hat{\mathbf{x}} + \epsilon, \tag{5.13}$$

where $\hat{\mathbf{y}} = \mathbf{y} - \mathbf{y}_a$ is the measurement vector containing the differences between logarithms of measured and simulated spectra (both normalized and paired) and $\hat{\mathbf{x}}$ is the state vector containing relative differences between the a priori and retrieved aerosol extinction profiles in a way that its components $j = 1, \ldots, n$ are $\hat{x}_j = (x_j - x_{a_j})/x_{a_j}$. This does not change the method substantially, but it alters Equation (5.12) to

$$\hat{\mathbf{x}}_{i+1} = (\mathbf{K}_i^{\mathrm{T}} \mathbf{S}_y^{-1} \mathbf{K}_i + \mathbf{S}_a^{-1})^{-1} \mathbf{K}_i^{\mathrm{T}} \mathbf{S}_y^{-1} (\mathbf{y} - \mathbf{y}_i + \mathbf{K}_i \hat{\mathbf{x}}_i) \tag{5.14}$$

The second modification is more substantial. At each iterative step the a priori information $\mathbf{x}_a$ is replaced by the result of the previous iteration $\mathbf{x}_i$, leading to the following iterative scheme

$$\mathbf{x}^* = (\mathbf{K}_i^{\mathrm{T}} \mathbf{S}_y^{-1} \mathbf{K}_i + \mathbf{S}_a^{-1})^{-1} \mathbf{K}_i^{\mathrm{T}} \mathbf{S}_y^{-1} (\mathbf{y} - \mathbf{y}_i) \tag{5.15}$$

with $x_j^* = (x_{i+1_j} - x_{i_j})/x_{i_j}$ being the components $j = 0, \ldots, n$ of the vector $\mathbf{x}^*$. This iterative scheme is more robust than the original Gauss-Newton approach, which means it converges with a higher probability at bad starting conditions (i.e., a bad "first guess" for the a priori). On the other hand it devalues the knowledge of the state before the measurements are made (a priori). Since we do not have much statistical a priori information about the global aerosol extinction anyway and are retrieving the aerosol extinction profiles with the same a priori extinction profile and an a priori covariance of 100 % at each geolocation and under totally different conditions (including very large aerosol particles induced by volcanic eruptions), it is suitable for us to make sure that our retrieval works even under conditions with a large difference between the a priori assumption and the true extinction.

5.2.3 Averaging kernel matrix

As described above, the weighting function matrix **K** represents the sensitivity of the measurement vector **y** (the limb radiance) to changes of the state vector **x** (the aerosol extinction). On the other hand, in Equations (5.12), (5.14), and (5.15) the *gain matrix*

$$\mathbf{D}_i = (\mathbf{K}_i^{\mathrm{T}}\mathbf{S}_y^{-1}\mathbf{K}_i + \mathbf{S}_a^{-1})^{-1}\mathbf{K}_i^{\mathrm{T}}\mathbf{S}_y^{-1} \tag{5.16}$$

describes the sensitivity of the retrieved aerosol extinction **x** to the measurement **y**. Furthermore, the *averaging kernel matrix*

$$\mathbf{A}_i = \mathbf{D}_i\mathbf{K}_i = (\mathbf{K}_i^{\mathrm{T}}\mathbf{S}_y^{-1}\mathbf{K}_i + \mathbf{S}_a^{-1})^{-1}\mathbf{K}_i^{\mathrm{T}}\mathbf{S}_y^{-1}\mathbf{K}_i \tag{5.17}$$

is a measure for the sensitivity of the retrieved aerosol extinction to the true aerosol extinction. Investigating the *averaging kernels*, i.e., the rows of the averaging kernel matrix after the last iterative step of Equation (5.15), can give us information about how the retrieved aerosol extinction at a specific altitude is influenced by changes of the aerosol extinction at other altitudes and about the vertical resolution. In general, **A** is a measure for vertical correlations between parameters. The sum of each kernel allows a statement about the information content coming from the measurement, while the difference of this sum to 1 represents the information content coming from the a priori at each altitude. Thus, values of 1 would mean that the a priori profile had no influence on the retrieval. See Section 6.4 for more information about the averaging kernels with respect to the retrieval parameters of the SCIAMACHY aerosol extinction retrieval.

6 SCIATRAN model and retrieval parameters

To apply the iterative scheme described in the previous section to all SCIAMACHY measurements and to analyse the retrieval algorithm, a forward model and retrieval code is necessary. SCIATRAN (Rozanov et al., 2013) is a radiative transfer model developed at the University of Bremen as an enhancement of the UV-visible near-nadir model GOMETRAN (Rozanov et al., 1997) and it is capable to perform a wide range of scientific tasks. The software package also contains a retrieval code that is suitable to solve the inverse problem of retrieving the atmospheric state such as aerosol extinction profile from limb-scattered radiance spectra. For this work, SCIATRAN version 3.1 was extended for the retrieval of aerosols. It can execute fast and accurate simulations of radiance spectra appropriate to atmospheric remote sensing observations in the ultraviolet, visible, near-infrared, mid-wavelength infrared, and thermal infrared spectral regions between 175.44 nm and 40 μm in a fully spherical atmosphere, a prerequisite for modeling limb-scattered solar radiation. This allows the simulation of any viewing geometry common for measurements of the scattered or transmitted solar radiation within or above the atmosphere (including radiative transfer in a coupled ocean-atmosphere system), e.g., limb, nadir, occultation, off-nadir, zenith, or off-axis as measured by satellite, air- and balloon-borne, or ground-based instruments, for all solar zenith angles. The forward model provides the capability to calculate polarized radiative transfer by means of using the discrete ordinate method (DOM) (Stamnes et al., 1988) with all four components of the Stokes vector. However, the retrieval mode depends on the calculation of weighting

functions which (next to other properties, e.g., the phase function) is not available in the vector version of DOM. Thus, the scalar mode of DOM is used in this work taking the intensity and no polarization into account.

6.1 Aerosol parameterization in SCIATRAN

Next to a wide range of gaseous atmospheric constituents, SCIATRAN includes the simulation of various types of aerosols of different origin and properties. Three types of parameterizations are available in addition to the possibility to choose the aerosol setting manually. Within this work, the parameterization specifically developed for SCIATRAN by Hoogen (1995) and Kauss (1998) is used for the retrieval containing the Henyey-Greenstein approximation of the phase function (retrieval version V1.0) and the manual setting is used to implement a Mie phase function (retrieval version V1.1). The next two sections describe both approaches.

6.1.1 Henyey-Greenstein approximation

If the SCIATRAN parameterization is selected, for each arbitrarily choosable atmospheric layer the extinction and scattering coefficients of mixtures of four different water soluble and eight insoluble aerosol components can be calculated at eight possible discrete relative humidities between 0 and 100 % by a standard Mie programm (Kauss, 1998, Hoogen, 1995, Wiscombe, 1980). Table 6.1 lists the available aerosol types. The underlying data for microphysical properties are from the software package OPAC (Optical Properties of Aerosols and Clouds, Hess et al., 1998). For the retrieval of stratospheric background aerosols we selected ”sulfate” (which means 75 % H_2SO_4 particles) at 0 % relative humidity without any other aerosol components for altitudes between 10 and 50 km. The size distribution of the stratospheric sulfate aerosols is assumed to be lognormal (see Equation (1.1) in Section 1.4) with

#	Type (size mode)	hygroscopic
1	water soluble	yes
2	sea salt (accumulation)	yes
3	sea salt (coarse)	yes
4	sulfate	yes
5	insoluble/dust	no
6	soot	no
7	mineral (nucleation)	no
8	mineral (accumulation)	no
9	mineral (coarse)	no
10	mineral (transported)	no
11	fresh volcanic ash	no
12	meteoric dust	no

Table 6.1: Aerosol types available in the SCIATRAN aerosol parameterization (adapted from Kauss (1998)).

a mode radius of 0.1 μm and a distribution width of 1.86, resulting in a median radius of approximately 0.07 μm (see Section 1.4). For detailed information on the SCIATRAN parametrization see Kauss (1998).

For the first part of the sensitivity studies and SCIAMACHY retrievals presented in this thesis (V1.0, Sections 7.1 and 8.1, respectively) we use the Henyey-Greenstein approximation for the aerosol phase function (see Equation (2.33)) which describes the phase function at a scattering angle Θ for an asymmetry parameter g:

$$P(\Theta) = \frac{1}{4\pi} \frac{(1-g^2)}{(1+g^2-2\,g\,\cos\,\Theta)^{3/2}} \tag{6.1}$$

The second expansion coefficient of the Legendre series of the phase function is

used as wavelength-dependent asymmetry parameter for the Henyey-Greenstein approximation, g(470nm) = 0.712 and g(750nm) = 0.655. Figure 6.1 shows the Henyey-Greenstein phase functions for 470 nm and 750 nm (dotted curves).

6.1.2 Mie phase function

For the second part of the sensitivity studies and SCIAMACHY retrievals (V1.1, Sections 7.2 and 8.2, respectively) a Mie phase function was implemented in SCIATRAN. As explained in detail in Section 1.4 by means of Figure 1.4, we chose a median radius of 0.11 μm and a distribution width of 1.37 to describe the lognormal size distribution for stratospheric background aerosols. Yue et al. (1994) deduced the stratospheric aerosol refractive index $n = n_r + in_i$ for different wavelengths, latitudes and seasons from SAGE II data. We chose $n_r(450\,nm) = 1.453$ and $n_r(800\,nm) = 1.446$ with an imaginary part $n_i = 10^{-8}$ as a spatial and temporal mean value for the complete SCIAMACHY data set. For background conditions, absorption of sulfate particles can be neglected. With these parameters we calculated the Mie phase functions with a standard Mie code developed at the University of Oxford (http://www-atm.physics.ox.ac.uk/code/mie/mie_lognormal.html). Figure 6.1 shows the phase functions for 450 and 800 nm for a lognormal size distribution with $r_g = 0.11$ μm and $\sigma = 1.37$ together with the Henyey-Greenstein phase function used in Sections 7.1 and 8.1.

6.2 Retrieval using SCIATRAN

Figure 6.2 depicts a schematic illustration of the retrieval process within SCIATRAN. As first step of the retrieval process, the forward model simulates the radiance profiles for 470 and 750 nm by executing Equation (5.5) and calculates the weighting functions by means of the corresponding SCIAMACHY geometry, atmospheric and

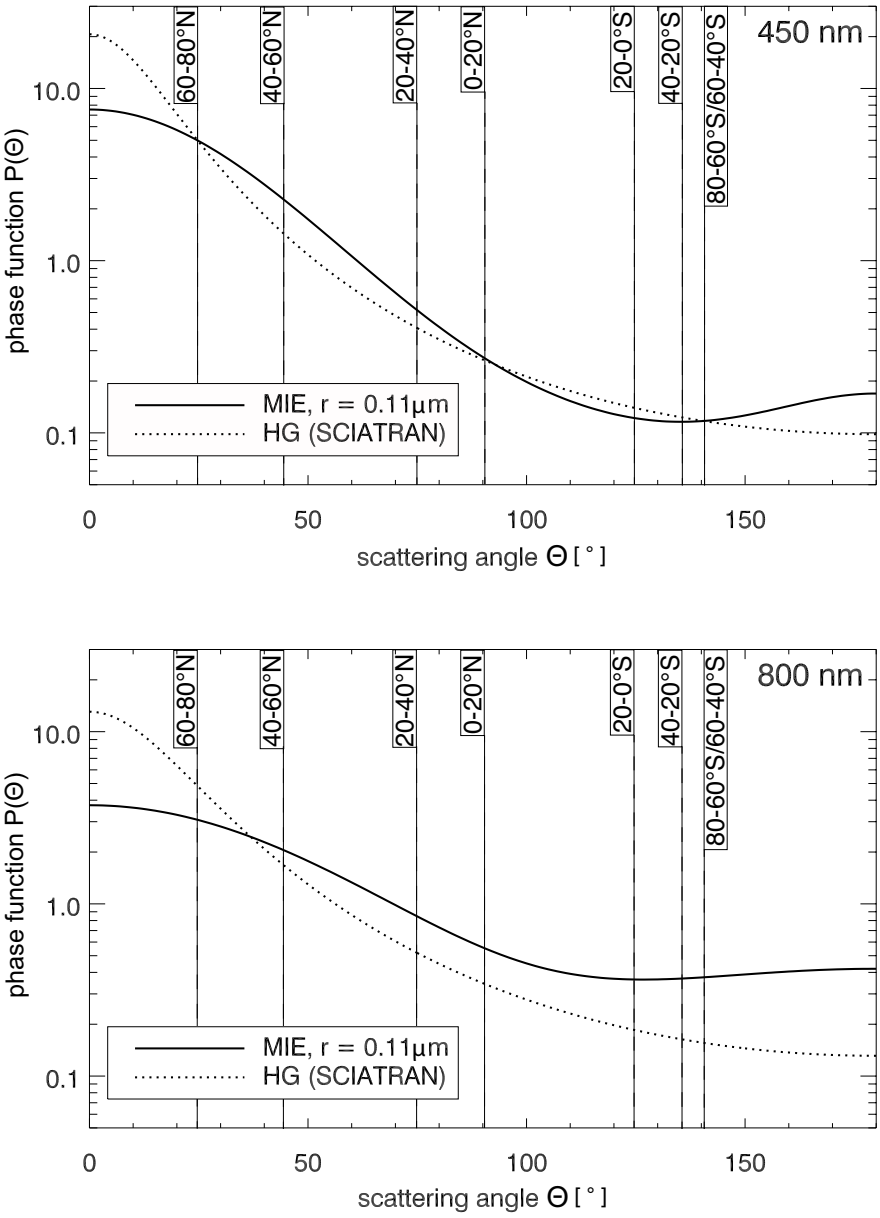

Figure 6.1: Phase functions for 450 nm (top panel) and 800 nm (bottom panel). The solid line shows the Mie phase function for a lognormal PSD with a median radius $r_g = 0.11\,\mu m$ and a distribution width of $\sigma = 1.37$, the dotted line the Henyey-Greenstein phase function used in the first version of the retrieval. The dashed vertical lines show the averaged scattering angles corresponding to the 20° latitude bins used for the SAGE II co-locations in Chapter 8.

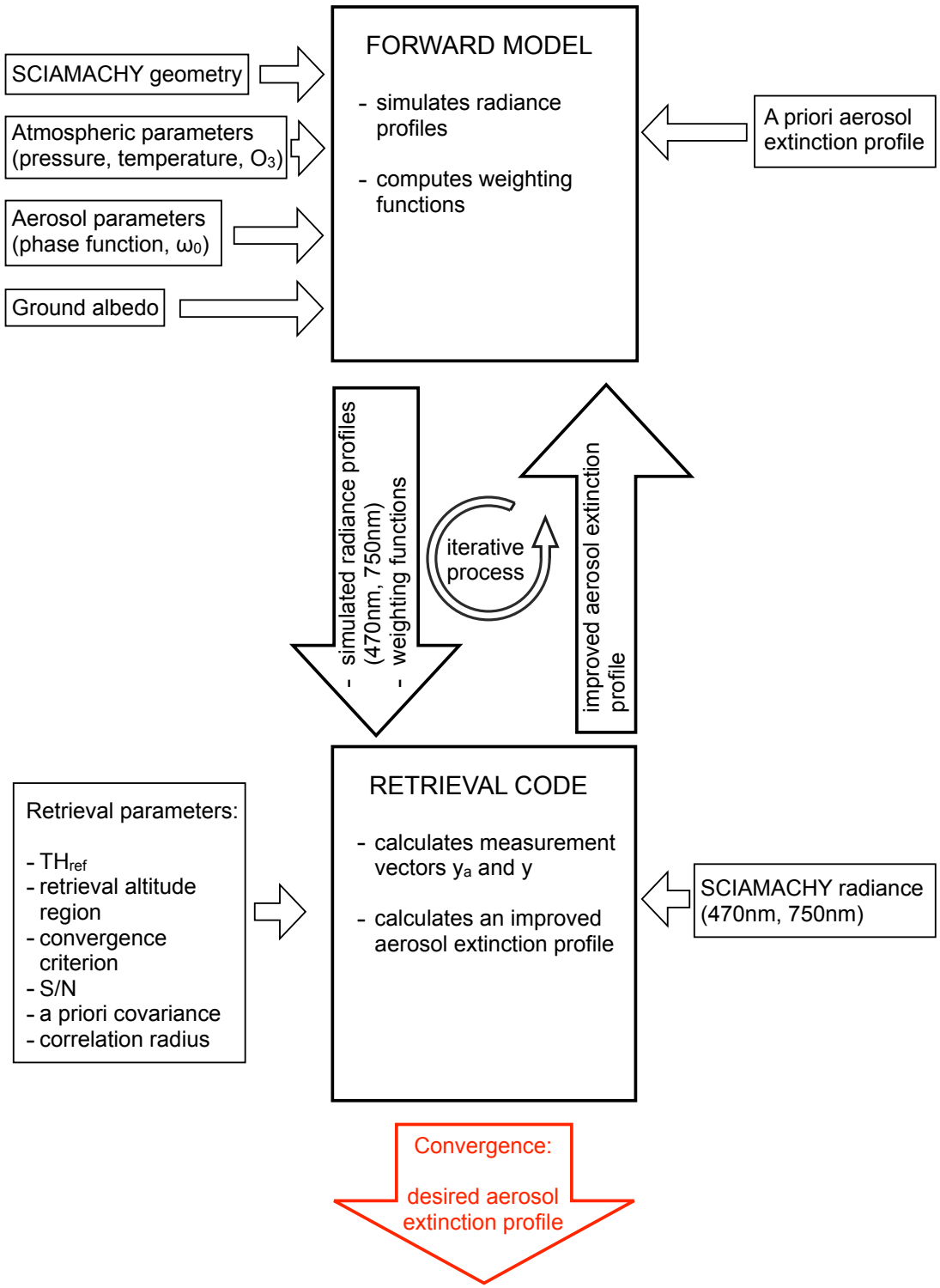

Figure 6.2: A sketch of the retrieval process within SCIATRAN.

surface parameters, and aerosol information including an a priori aerosol extinction profile $\mathbf{x}_a$. The simulated radiances and the weighting functions are then passed to the retrieval algorithm which calculates the measurement vector $\mathbf{y}_a$ from these simulated radiances (normalized and paired) and mathematically "compares" this simulated measurement vector with the corresponding vector $\mathbf{y}$ of the true SCIAMACHY measurement and alters the aerosol extinction profile by performing the first iterative step of Equation (5.15). This new aerosol extinction profile is returned to the forward model which uses it instead of the a priori profile to simulate a new measurement vector closer to the true SCIAMACHY measurement vector. Forward model and retrieval code are run subsequently within the iterative process until the relative change of either the root mean square of the fit residual (i.e, the difference between the simulated and true measurement vector) or the aerosol extinction with respect to the previous iterative step falls below a predefined value, the *convergence criterion*. The retrieval altitude grid is a regular 1 km grid. SCIATRAN allows for a field of view integration to take the finite vertical resolution of the SCIAMACHY limb measurements into account.

Figure 6.3 shows as an example the retrieval of the aerosol extinction profile from a SCIAMACHY measurement from 12 September 2004 (Orbit #13254). The left side of each of the four panels shows the simulated and SCIAMACHY measurement vector constructed as described in Section 5.1 before the retrieval (top left) and after the first 3 iterative steps (after which the convergence criterion was fulfilled). The right side of each panel shows the corresponding aerosol extinction profile in comparison to the a priori profile (dotted line) and a co-located SAGE II profile as the assumed "true" aerosol extinction (blue). For further information on SAGE II co-locations see Chapter 8. The horizontal dashed lines denote the tangent heights between which the retrieval is performed (approximately 12–35 km).

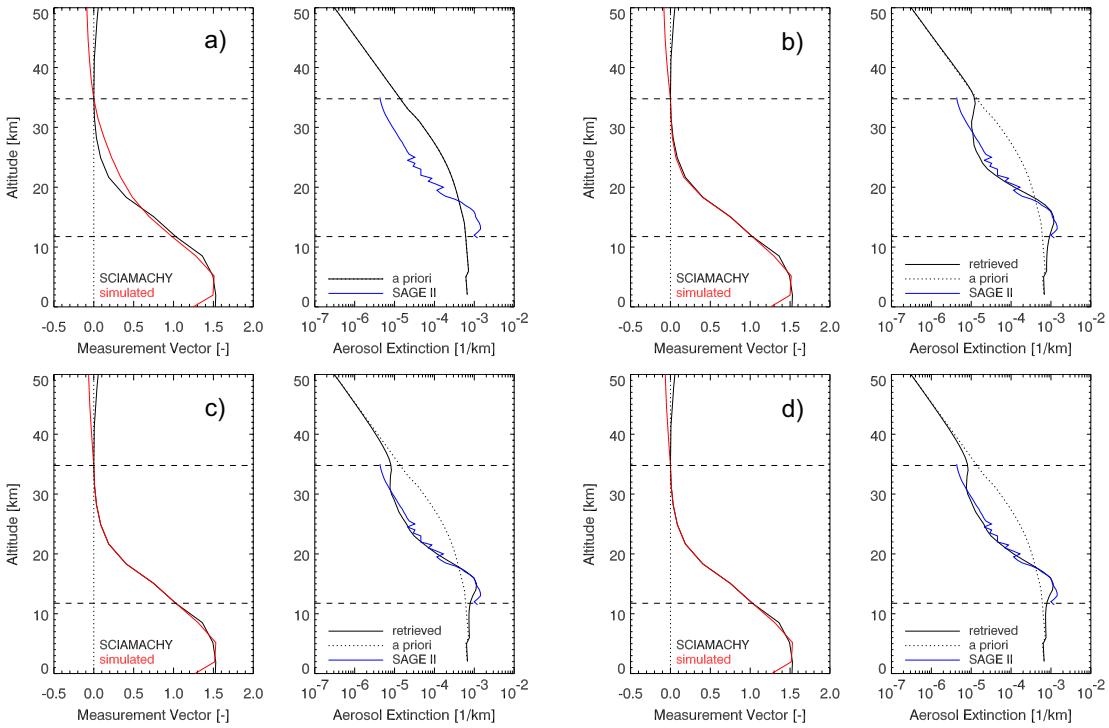

Figure 6.3: Exemplary retrieval process: simulated (red) and SCIAMACHY (black) measurement vector (left side of the four panels) and aerosol extinction profile (right side) before the retrieval (a) and after the first three iterative steps (b, c, d). The black dotted curve in panels b – d depicts the a priori aerosol extinction profile, the blue curve a co-located SAGE II measurement. The horizontal dashed lines denote the tangent heights between which the retrieval is performed (approximately 12–35 km).

6.3 Retrieval setup

The aerosol extinction is retrieved at the SCIAMACHY tangent height steps 6–13, corresponding to tangent altitudes of approximately 12–35 km. To reduce the signal-to-noise ratio, we do not use the radiance at two discrete wavelengths near 470 and 750 nm in the SCIAMACHY spectrum, but the radiance averaged over two 4 nm spectral windows. The lower wavelength window (468–472 nm) contains 17 SCIAMACHY detector pixels (channel 3), the upper one (748–752 nm) 19 (channel 4).

The retrievals performed as part of this study are based on SCIAMACHY Level 1 data version 7.03. Table 6.2 shows the possible calibrations for SCIAMACHY level 1 data. Due to remaining issues with the memory effect correction, polarization correction, and absolute calibration, these calibrations were not performed for aerosol extinction retrievals. Note that absolute calibration is made obsolete by the tangent height normalization step of the retrieval algorithm.

Flag	Calibration
0	Memory effect
1	Leakage current
2	pixel to pixel gain (ppg)
3	etalon
4	Straylight
5	Spectral calibration
6	Polarization
7	Radiance (absolute calibration)

Table 6.2: Calibration options for SCIAMACHY level 1 data.

The exact time, location, and geometry (tangent heights and angles) used by the forward model are taken from the corresponding SCIAMACHY measurement while ECMWF analysis data are used as pressure and temperature profiles of each SCIAMACHY measurement. To determine the ground albedo, we used the Matthews data base (Matthews, 1983) which contains the wavelength-independent Lambertian reflectance considering vegetation, land use, and land cover on a $1^\circ \times 1^\circ$ grid. As trace gas O_3 is taken into account. The McLinden climatological data base (private comm.) gives monthly vertical distributions for altitudes of 0–100 km in 10° latitude bins. As a priori profile we used the 75°S modified ECSTRA aerosol extinction profile for all latitudes. The following section delivers further information on the

choice of the a priori aerosol extinction profile. These and more parameter settings are listed in Table 6.3.

Forward model & retrieval code	SCIATRAN 3.1
Radiative transfer model	scattering in approximately spherical atmosphere
Numerical method	Discrete Ordinate Method (scalar) and Combined Differential-Integral approach
Aerosol phase function	V1.0: Henyey-Greenstein approximation V1.1: Mie phase function
Single scattering albedo ω_0	1 (no absorption)
Wavelengths	470±2 nm (ch. 3), 750±2 nm (ch. 4)
Tangent heigth selection	# 6 – 13 (≈ 12 – 35 km)
Normalization TH	# 13 (≈ 35 km)
Surface albedo	Lambertian reflector (Matthews data base)
Clouds	not present
Convergence criterion	10^{-3} (RMS or aerosol profile) between 13 – 35 km
S/N	200
A priori covariance	1 (all altitudes)
Correlation radius	3.3 km
Trace gases	Ozone
Pressure and temperature	ECMWF operational

Table 6.3: SCIATRAN parameter settings for the aerosol extinction profile retrieval.

6.3.1 A priori aerosol extinction profiles

The a priori aerosol extinction profiles required for the retrievals were determined with the ECSTRA model by Fussen (1999). ECSTRA is a climatological model of vertical extinction coefficient profiles of stratospheric aerosols in the UV-visible range as a function of wavelength, month, latitude, and volcanism level represented by the aerosol optical depth. The ECSTRA model is based on SAGE II stratospheric aerosol extinction profile data. ECSTRA provides aerosol extinction profiles above the tropopause only, and the tropopause height was taken – depending on latitude and month of the year – from the climatological tropopause height data set by Randel et al. (2000). The vertical structure of the ECSTRA aerosol profile climatology describes the tropopause region, the Junge layer and the high altitude domain (Fussen, 1999). For the retrieval sensitivity studies described in Chapter 7 we calculated aerosol extinction profiles for five different latitudes (83°N, 40°N, 0°, 40°S, and 75°S) and the month of September with a stratospheric aerosol optical depth of 10^{-3} corresponding to a background aerosol loading without preceding volcanic activity (Thomason et al., 2006). The ECSTRA aerosol extinction profiles were extrapolated exponentially above 30 km with a scale height of 4 km, based on Thomason et al. (2006), and we removed the edge below the tropopause that is generated by the ECSTRA model. Figure 6.4 shows the modified ECSTRA profiles for the five latitudes. It turned out that the modified ECSTRA profile for 75°S worked best as a priori profile for the retrieval of the aerosol extinction profiles at all SCIAMACHY latitudes. This profile has been used to obtain the results presented in Chapters 8 and 9.

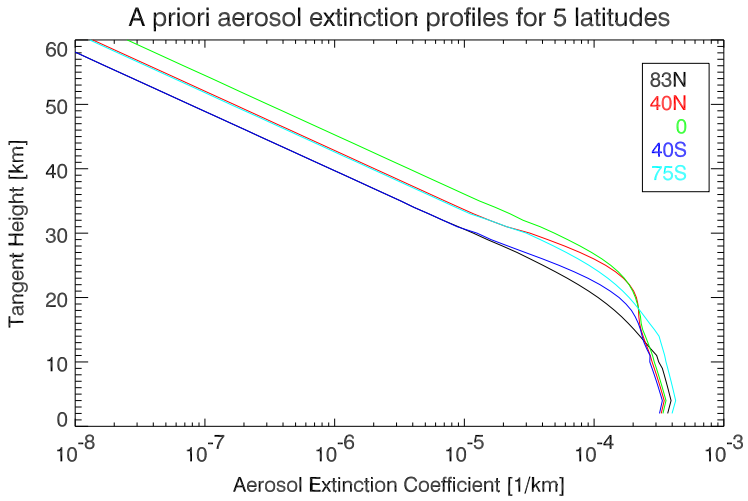

Figure 6.4: The modified a priori aerosol extinction profiles for the five latitudes 83°N, 40°N, 0°, 40°S, and 75°S.

6.4 Averaging kernels

Figure 6.5 shows the averaging kernels (see Section 5.2.3) of a SCIAMACHY aerosol extinction coefficient retrieval. The shape of each kernel with a FWHM of about 3 km gives evidence about the vertical resolution which is limited by the TH steps and the finite vertical field of view of the instrument of the instrument. The multiple thin black curves above 30 and below 15 km with values up to -0.15 and $+0.3$, respectively, indicate that in these altitude regions the retrieval is influenced by aerosol extinction changes outside the retrieval altitude region. The black dashed line is the sum of each kernel below the normalization tangent height plotted over its corresponding altitude. As mentioned in Section 5.2.3, the value of this curve compared to 1 provides information about the balance between the influence of the a priori and the measurement in the retrieved aerosol extinction profile. In our case, with values around 0.8 in the retrieval altitude region below 25 km and smaller values between 25 and 35 km, the choice of the apriori profile *has* an influence on

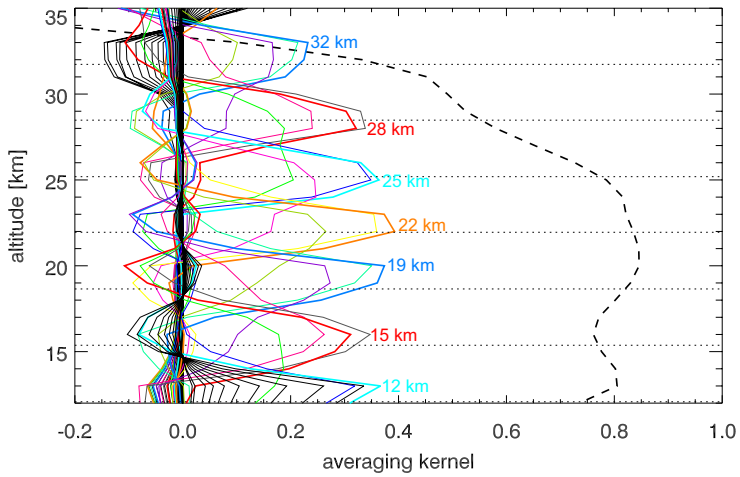

Figure 6.5: Averaging kernels of the SCIAMACHY aerosol extinction coefficient retrieval, within (colored) and outside (black) the retrieval altitude region (12–35 km). The thick lines represent the averaging kernels corresponding to altitudes near the measurement tangent heights. The black dashed line shows the sum of all averaging kernel elements below the normalization tangent height, the thin dotted lines depict the tangent heights of the SCIAMACHY measurement.

the retrieval, but since the a priori information is replaced at each iteration step by the result from the previous iteration, this influence is strongly reduced during the iterative process. Running the SAGE II co-locations (Chapter 8) with a different a priori profile did not change the results noticeably.

7 Sensitivity studies

The retrieval of stratospheric aerosol extinction profiles presented in this thesis is based on measurements of limb-scattered solar radiation. Unfortunately, the observed limb radiances do not only depend on the aerosol extinction profiles, but also on several other geophysical parameters (e.g., surface albedo, neutral density, clouds, and potentially minor constituent profiles) and instrumental effects (e.g., tangent height registration). A precondition for retrieving stratospheric aerosols or any other atmospheric parameter from limb-scattered solar radiation with the retrieval setup used here is the accurate simulation of the above mentioned physical parameters and the viewing geometry of the instrument. Futhermore, retrieval parameters such as the assumed a priori aerosol extinction profile can influence the retrieval result. In order to quantify the effects of these parameters on the retrieval results, sensitivity analyses were performed for the most important effects. The general approach used for these sensitivity studies is to perform forward model runs with different settings – i.e., introducing artificial errors – for the specific parameter to be investigated, leaving all other settings unchanged. The simulated limb radiance profiles are then used as input data for the retrieval with the standard parameter set. For the cloud sensitivity study, tropospheric clouds are simulated in forward model runs which are then used as input data for cloud-free retrieval runs. The artificial error in the corresponding parameter or the effect of the cloud is compensated by an error in the retrieved aerosol extinction. The effect on the aerosol extinction profile retrievals is quantified in terms of the relative difference

between the retrieved and the true aerosol profile (retrieved−true)/true. In the first part of this chapter (Section 7.1) the results of the sensitivity studies for the Henyey-Greenstein retrieval version (V1.0) are presented, the second part (Section 7.2) shows the results for the retrieval version with an implemented Mie phase function (V1.1) and a discussion of the differences between the two versions.

7.1 Henyey-Greenstein approximation

The following sections deal with the effect of the a priori profiles (Section 7.1.1), errors in the assumed surface albedo (Section 7.1.2), neutral density profiles (Section 7.1.3), ozone profiles (Section 7.1.4), occurence of tropospheric clouds (Section 7.1.5), and errors in the tangent height registration (Section 7.1.6) for the retrieval version V1.0 using the Henyey-Greenstein approximation for the phase function. In Section 7.1.7 the results are summarized in the Tables 7.1 and 7.2.

7.1.1 Impact of a priori profile

The retrieval algorithm was tested by performing retrievals with synthetic, i.e., forward modelled observations. For these the a priori aerosol extinction profiles were modified in six different ways – as described below – and used as aerosol extinction profiles for SCIATRAN forward model runs that produced the synthetic observations. The six modifications are multiplication with a factor of 0.5 and 2 in all altitudes, a height shift of the complete profile by ± 3 kilometers, and an artificial minimum/maximum around an altitude of 25 kilometers. Then we ran the retrieval with the unmodified a priori profile without changing any other parameter to see if the true profiles are reproduced by the retrieval. A northern mid-latitude SCIAMACHY geometry was simulated (see Table 5.1), the corresponding a priori profile used (red curve in Figure 6.4). Figure 7.1 shows the results of the synthetic

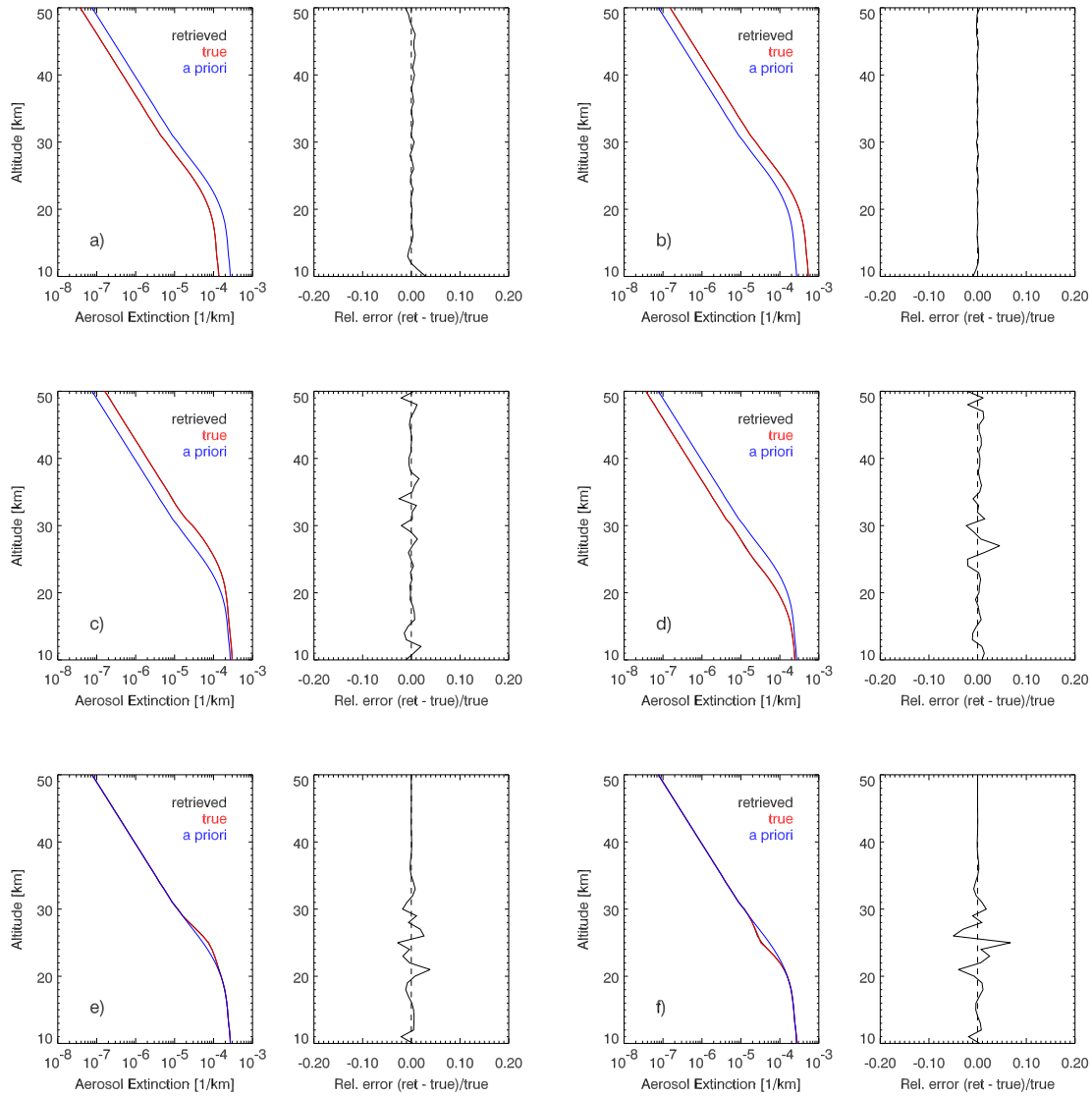

Figure 7.1: Synthetic retrievals with the six modifications of the a priori aerosol extinction profiles using the Henyey-Greenstein approximation for the phase function. Left panels: true, retrieved, and a priori aerosol extinction profiles. Right panels: relative difference between the true and the retrieved aerosol extinction profiles. Modifications of the true profile in comparison to the a priori profile: a) multiplied by 0.5; b) multiplied by 2; c) altitude shift +3 km; d) altitude shift −3 km; e) artificial maximum around 25 km; f) artificial minimum around 25 km.

retrievals. The relative error is generally on the order of a few percent and is below 10 % even in the worst case. We conclude that the retrieval works well in a general sense and that it reacts relatively insensitively to a priori profiles that may not well represent the true aerosol extinction profile.

7.1.2 Effect of surface albedo

Figure 7.2 shows the relative error in the retrieved aerosol extinction coefficient for different true albedo values with respect to an assumed albedo of 0.5 as a function of the ground albedo and altitude. Five typical SCIAMACHY geometries are simulated here, for latitudes ranging from 83°N to 75°S (see Table 5.1) for northern fall equinox to allow a comparison of the two hemispheres. The first three panels, corresponding to 83°N, 40°N, and 0°, show that the sensitivity of the retrieval to the ground albedo is much higher in the tropics (with errors of up to 40 %) than in the northern polar regions (with errors of about 2 %). Due to the smaller solar zenith angle of the SCIAMACHY observations in the tropics, a larger part of the sunlight is reflected by the ground and scattered into the instrument. The tangent height normalization (see Section 5.1) is not capable of fully compensating for this effect. Comparing the two hemispheres – 40°N and 40°S in particular – indicates that the retrieval is far more sensitive to the ground albedo in the southern hemisphere. This finding is consistent with the general shape of the aerosol scattering phase function and the latitudinal variation of the scattering angle associated with SCIAMACHY limb-scatter observations, which shows a smooth transition from small scattering angles at high northern latitudes to large scattering angles at high southern latitudes (see Figure 4.4). A typical aerosol phase function has much smaller values at larger scattering angles (see Figures 2.1 and 6.1), corresponding to the larger solar azimuth angles at southern latitudes (see Table 5.1 and Figure 4.4). This leads to a smaller relative contribution of aerosol scattering with respect to Rayleigh scattering. In

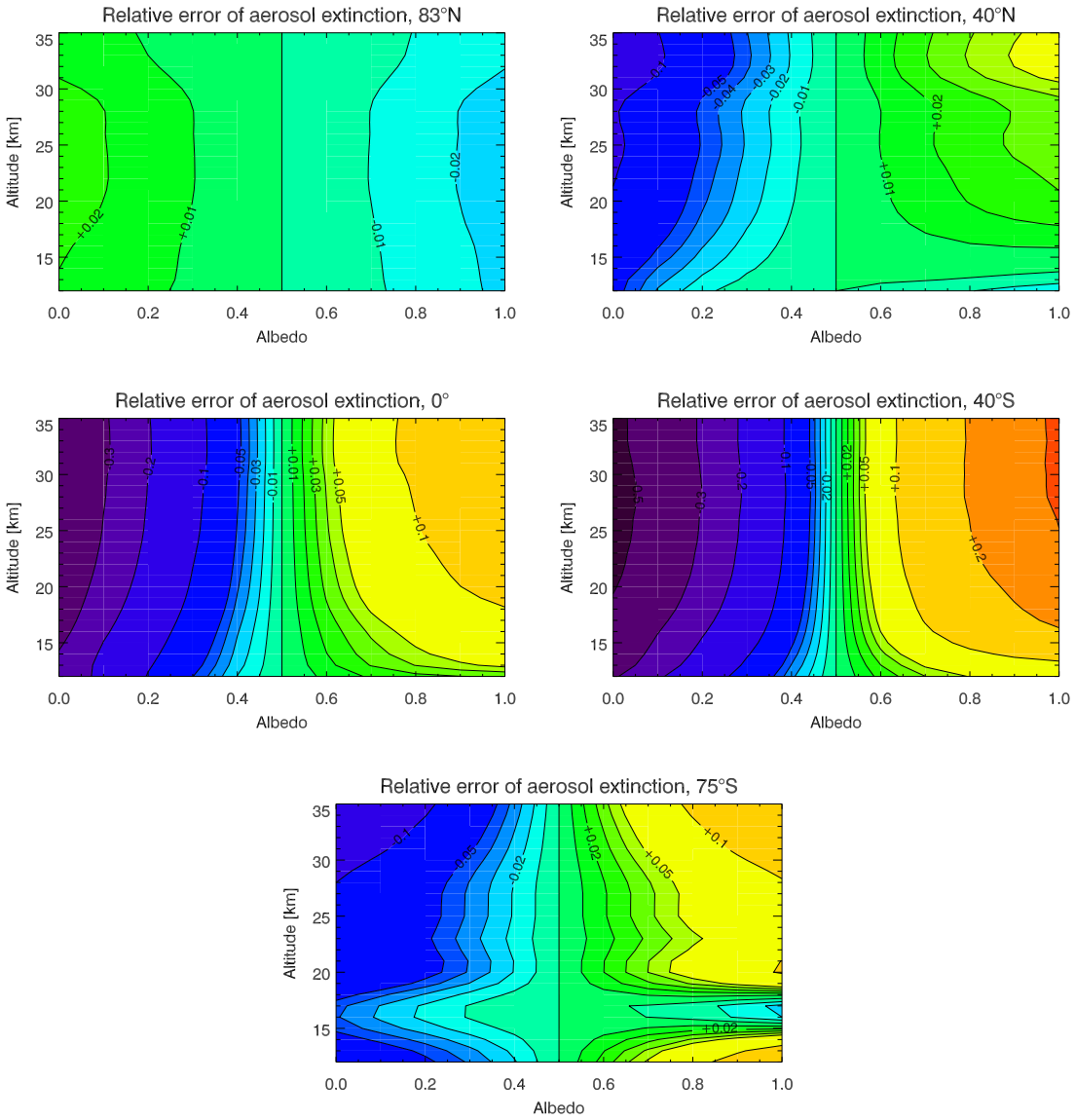

Figure 7.2: Relative errors in the aerosol extinction coefficients retrieved with the Henyey-Greenstein retrieval version for different values of the true surface albedo A and the SCIAMACHY viewing geometry at 83°N, 40°N, 0°, 40°S, and 75°S. The albedo assumed for the retrieval is A = 0.5.

other words: at 40°S, a larger amount of aerosols is needed to compensate for the same albedo error than at 40°N. In the southern polar region, this effect is superimposed by the smaller impact of the ground albedo due to higher solar zenith angles in the polar regions (see Table 5.1). The feature below 20 km at this latitude is probably a consequence of the very high solar zenith angle of 88° which causes problems in most sensitivity studies for this latitude and altitude. We also note that apart from the highest northern latitude studied (83°N) – where large solar zenith angles and small scattering angles coincide – a low bias in the assumed surface albedo will lead to a high bias in the retrieved aerosol extinction values.

7.1.3 Effect of neutral density

For the same latitudes and viewing angles as above, we investigated the effect of errors in the neutral density profile on the aerosol profile retrievals. The neutral density profile has a direct impact on the limb radiance profiles, because it determines the Rayleigh scattering contribution to the limb radiances. In SCIATRAN the neutral density at all altitudes can be adjusted by the ground pressure, using a constant temperature profile. Figure 7.3 shows the impact on the retrieved aerosol extinction of changing the ground pressure by ± 30 hPa relative to a reference pressure of 1013 hPa, corresponding to a roughly 3 % perturbation in the density at all altitudes. The effect is generally below 10 % at all latitudes for altitudes above 20 km, closer to the tropopause it can be up to 20 %.

7.1.4 Effect of ozone

To investigate the effect of an error in the assumed ozone profile on the retrieval, we scaled the entire ozone profile by ± 15 % for polar and tropical geometry. SCIATRAN allows to scale the ozone profiles – which are taken from the MPI-C (Max Planck

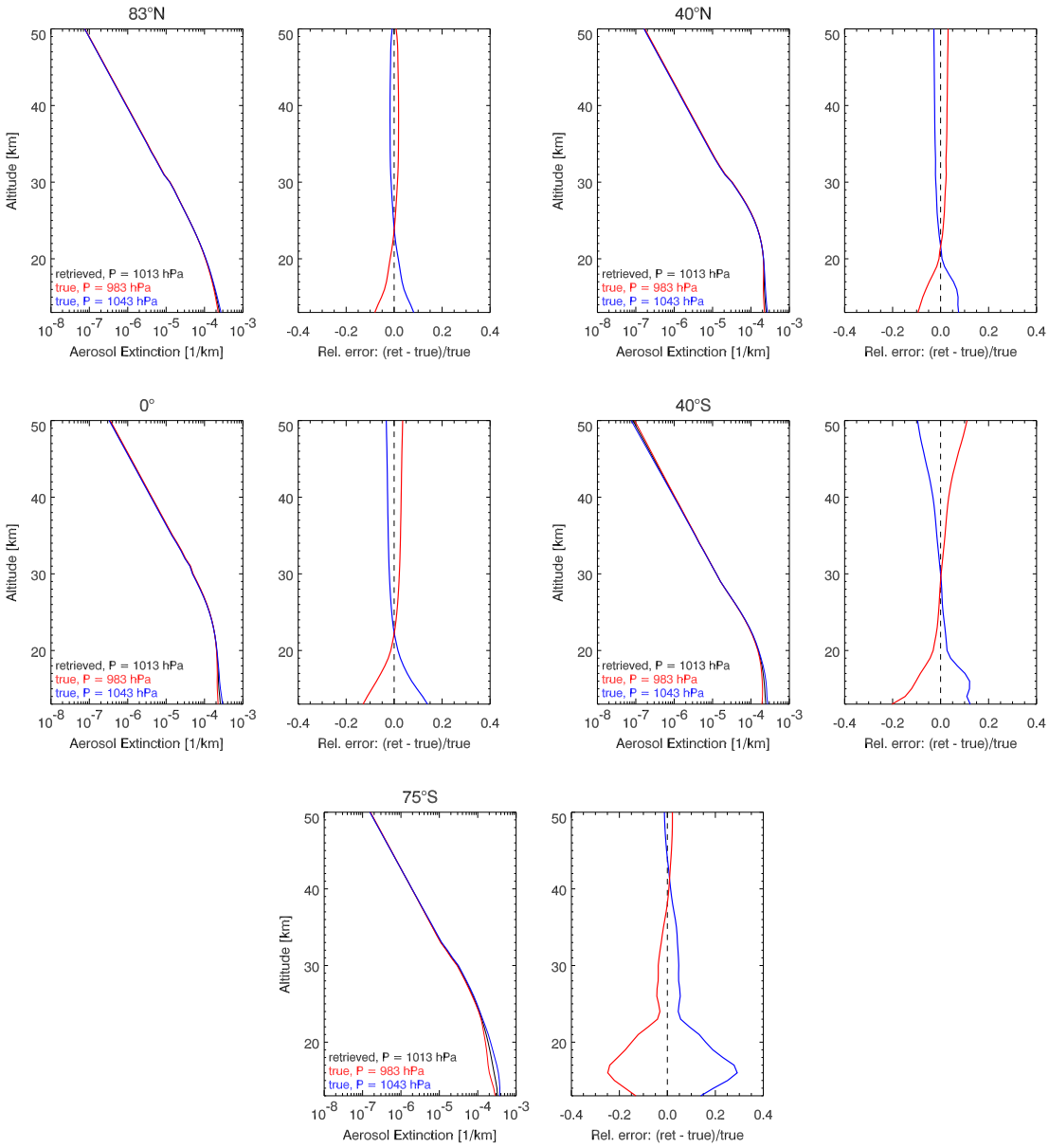

Figure 7.3: Relative errors in the aerosol extinction coefficients retrieved with the Henyey-Greenstein retrieval version for an error of about ±3 % in the neutral density and the SCIAMACHY viewing geometry at 83°N, 40°N, 0°, 40°S, and 75°S.

Institute for Chemistry) stratospheric ozone climatology using monthly and zonal means at 10 degree latitude bins – with a manually set total column. In the standard runs we chose typical values of the total ozone column for the reference case: 400 DU for polar latitudes and 250 DU for tropical latitudes. For the sensitivity study these reference columns were then perturbed by ± 15 %. The SCIAMACHY geometry is simulated for the two latitudes. Figure 7.4 shows the result of the sensitivity study. Even for the polar scenario with a large total ozone abundance, the impact on the aerosol extinction is below 2 %. The main reason why the stratospheric aerosol retrieval is relatively independent of the stratospheric ozone profile is that $\lambda_s = 470$ nm and $\lambda_l = 750$ nm are well outside the center of the Chappuis absorption bands of ozone, and the ozone absorption cross-section is relatively small at these wavelengths.

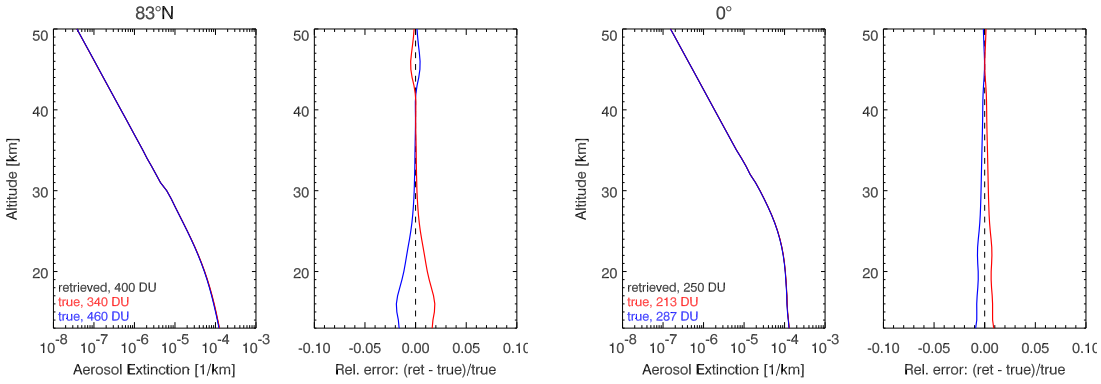

Figure 7.4: Relative errors in the aerosol extinction coefficients retrieved with the Henyey-Greenstein retrieval version for an error of ± 15 % in the ozone profile for a polar and a tropical SCIAMACHY viewing geometry. Left panel: 83°N, 400 DU ± 15 %; right panel: 0°, 250 DU ± 15 %.

7.1.5 Effect of tropospheric clouds

Tropospheric clouds are an additional error source for the retrieval of stratospheric aerosols as they influence the fraction of light that is scattered from below the

retrieval altitude into the line-of-sight of the instrument. Figure 7.5 shows the relative error in the aerosol extinction (V1.0) caused by a 3 km thick, closed water cloud layer with an optical thickness of $\tau = 20$ at different altitudes (cloud top height from 4 to 10 km) below the retrieval altitude (12–35 km) at the five geometries. The assumed ground albedo is 0.3. For this optically thick cloud layer the relative error in the northern hemisphere and at the equator is rather small, <15 % at all altitudes. At 40°S, the error is larger than 20 % and at 75°S the picture looks completely different. Not only is the error extremely large (up to 300 %, note the different abscissa), but also behaves very differently depending on the cloud top height (CTH) compared to the other latitudes studied. While a low cloud (1–4 km, red curve) leads to an overestimation in the aerosol extinction of up to 80 % from above the tropopause to 32 km and an underestimation of up to 80 % above, a high cloud (7–10 km, turquois curve) leads to a strong underestimation (up to 100 %) in the aerosol extinction below 16 km and an extremely high overestimation of up to 300 % above. This pattern is an effect of the large solar zenith angle of 88° (see Table 5.1) which leads to the relatively strong dependence of the retrieval errors on cloud top height (in contrast to the other cases studied, but also visible at 83°N) combined with the large scattering angle, which leads to the large error at high southern latitudes (see discussion with respect to the phase function in Section 7.1.2). Reducing the SZA to 83° without changing other parameters (see last panel in Figure 7.5) removes the dependence on cloud top height, but the relative error in the aerosol extinction is with >50 % between 25 and 30 km relatively large compared to the other latitudes.

We performed this sensitivity study with water and ice clouds of different optical thicknesses (1, 5, 10, and 20). Figure 7.6 shows two examples of the results for 40°S. Ice clouds with the same properties as the water clouds discussed above (3 km thick, $\tau = 20$) lead to more or less the same error in the aerosol extinction as water

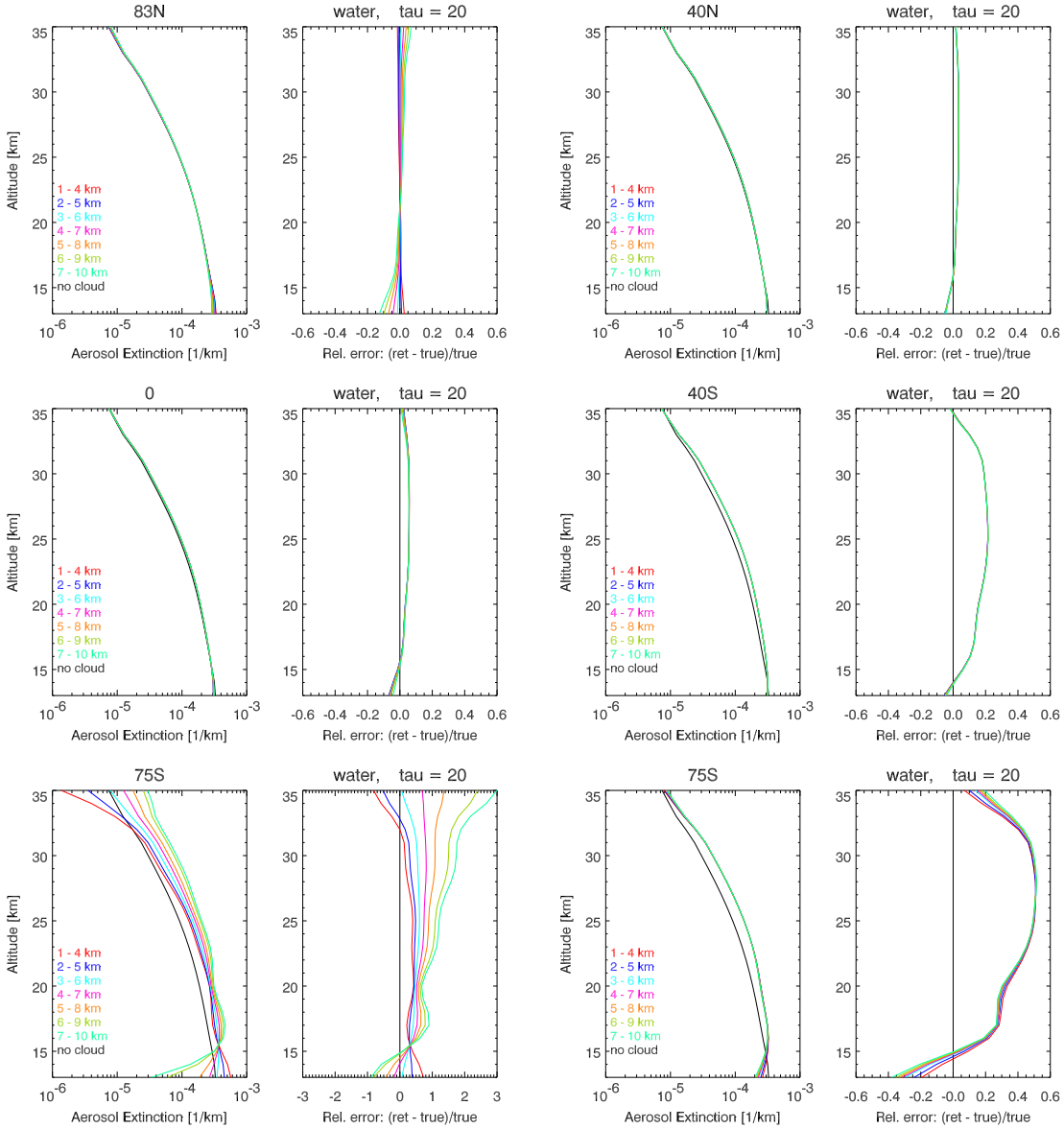

Figure 7.5: Relative error in the aerosol extinction (V1.0) for a water cloud layer with 3 km vertical extension and an optical thickness of $\tau = 20$ at seven different altitudes below the retrieval altitude. The first five sets of panels again show aerosol extinction profiles (left panels) and the relative error (right panels) for a SCIAMACHY viewing geometry at 83°N, 40°N, 0°, 40°S, and 75°S as listed in Table 5.1. The last set of panels (bottom right) shows the 75°S geometry with a modified solar zenith angle of 83°S.

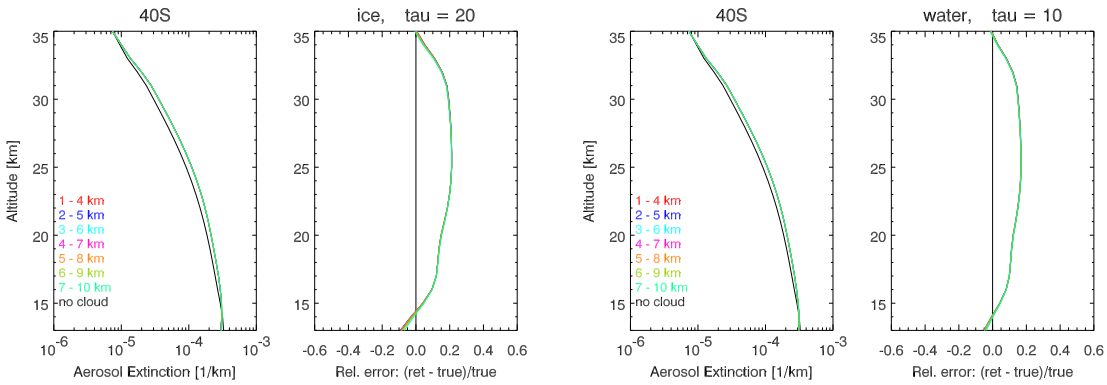

Figure 7.6: Relative error in the aerosol extinction (V1.0) for a cloud layer with 3 km vertical extension at seven different altitudes below the retrieval altitude for a SCIAMACHY viewing geometry at 40°S. Left panel: ice cloud with $\tau = 20$, Right panel: water cloud with $\tau = 10$.

clouds. Reducing the optical thickness of a water cloud to $\tau = 10$ leads to a smaller error in the aerosol extinction.

7.1.6 Effect of tangent height errors

Another error source for the retrieval of aerosol extinction profiles are errors in the tangent height registration of the SCIAMACHY limb-scatter observations. Older versions of the SCIAMACHY level 1 data set (lower than version 6.0) were affected by TH errors of up to several kilometers (von Savigny et al., 2005). The currently used versions 7.03 and 7.04 are associated with TH errors of a few hundred meters at most. To investigate this effect, we shifted all tangent heights by ± 200 m, ± 500 m and ± 1000 m. Figure 7.7 shows the impact on the aerosol extinction profiles at 40°N latitude. Above an altitude of about 20 km, this impact is below 20 % for the 1000 m shift, while below the error can be quite large, up to 45 % at 16 km for a tangent height error of 1000 m. For a typical SCIAMACHY tangent height error of ± 200 m (von Savigny et al., 2009), the impact on the aerosol extinction has a maximum of about 8 % at 16 km and is smaller than 5 % above 20 km.

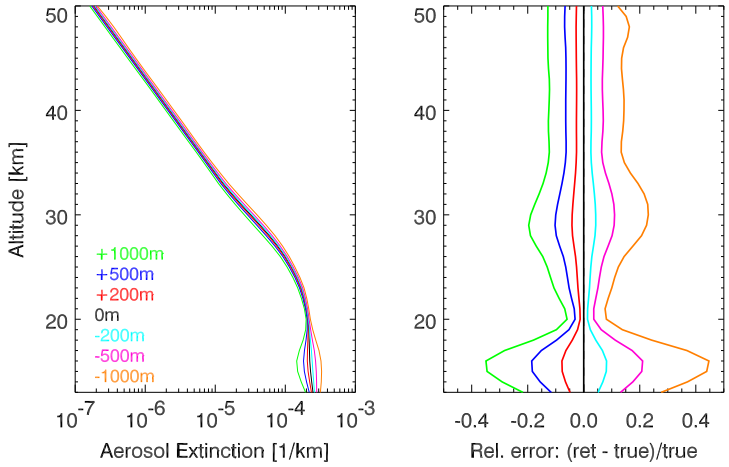

Figure 7.7: Relative errors in the aerosol extinction coefficients retrieved with the Henyey-Greenstein retrieval version for a tangent height error of ± 200 m, ± 500 m, and ± 1000 m for a northern mid-latitude SCIAMACHY viewing geometry.

7.1.7 Summary of the sources of potential systematic errors

The Tables 7.1 and 7.2 provide an overview of the sensitivity study results described above. Listed in Table 7.1 are the retrieval errors – at the five different latitudes – associated with tropospheric clouds and with uncertainties in the knowledge of surface albedo and neutral density profile. Table 7.2 shows the retrieval errors corresponding to uncertainties in the ozone profile for a polar (83°N) and a tropical (0°) viewing geometry, and in tangent height registration at 40°N. The assumed albedo error is 0.15 (with respect to A = 0.5), the assumed error in the neutral density profile is 3 % (scaling with altitude independent factor), and the error in the ozone profile is 15 % (scaling with altitude independent factor). The tangent height error is 200 m. To determine the error with respect to clouds, a typical tropospheric cloud (following Sonkaew et al. (2009) and references therein) is simulated, i.e., a water cloud with a droplet radius of 8 µm, an optical thickness of 10 and a vertical extension from 4–7 km. Again, the ground albedo is 0.3.

Alt. [km]	83°N			40°N			0°			40°S			75°S		
	A	ND	Cl.	A	ND	Cl.	A	ND	Cl.	A	ND	Cl.	A	ND	Cl.
15	<1	5	1	1	8	1	5	10	1	8	12	4	1	20	15
20	<1	2	2	2	1	2	7	2	2	12	3	12	3	15	25
25	<1	0	2	2	1	3	8	2	3	15	1	17	3	5	30
30	<1	2	2	2	2	3	8	2	3	15	0	15	4	5	25
35	<1	2	1	3	2	2	8	3	2	15	2	1	5	5	10
Mean	< 1	2	2	2	3	2	7	4	2	13	5	10	3	10	20

Table 7.1: Absolute value of the relative error [%] of the aerosol extinction retrieved with the Henyey-Greenstein retrieval version (V1.0) due to uncertainties in ground albedo ("A", uncertainty 0.15) and neutral density ("ND", 3 %) and due to a typical tropospheric cloud ("Cl.") for the SCIAMACHY viewing geometry at 83°N, 40°N, 0°, 40°S, and 75°S.

The results show that retrieval version V1.0 using a Henyey-Greenstein phase function is very sensitive to errors in other geophysical parameters, particularly in the southern hemisphere. Tropospheric clouds and uncertainties in the knowledge of neutral density and ground albedo can lead to errors of up to 30 %, 20 %, and 15 %, respectively. Smaller error sources are tangent height registration (8 %), the a priori profile (7 %), and ozone (2 %).

Alt. [km]	O3		TH
	83°N	0°	40°N
15	2	1	8
20	2	1	2
25	1	0.5	3
30	0	0.5	5
35	0	0.5	3
Mean	1	1	4

Table 7.2: Absolute value of the relative error [%] of the aerosol extinction retrieved with the Henyey-Greenstein retrieval (V1.0) version due to uncertainties in the ozone profile (15 %) and tangent height (200 m) for the SCIAMACHY viewing geometry at 83°N and 0° and 40°N, respectively.

7.2 Mie phase function

The sensitivity studies for the HG retrieval version showed a strong dependence on the latitude of the SCIAMACHY observations, which is a consequence of the aerosol scattering phase function in combination of the latitudinal dependence of the scattering angle. The following Sections 7.2.1 – 7.2.6 show the results of the same studies using the Mie phase function described in Section 6.1.2 and point out the differences to the Henyey-Greenstein retrieval version. In Section 7.2.7, the results are summarized. Unless mentioned otherwise in the text, all parameters except the phase function remained unchanged for a better comparison with the HG version.

7.2.1 Impact of a priori profile

Figure 7.8 shows the results of the synthetic retrievals with the six different true aerosol extinction profiles generated by modifications of the a priori profile described in Section 7.1.1. A different a priori profile than for the HG version is used, i.e. the one that is used for the retrieval of real SCIAMACHY data later in this work (the light blue curve for 75°S in Figure 6.4). The modifications are the same as for the HG version. The results are very similar to those of the HG version, the relative error is below 10 % for all cases and altitudes. The only mentionable difference appears in altitudes between 30 and 40 kilometers for the ± 3 km shift (panels c and d of Figure 7.8), were the relative error is larger than for the HG phase function, but still relatively small (within ± 7 %).

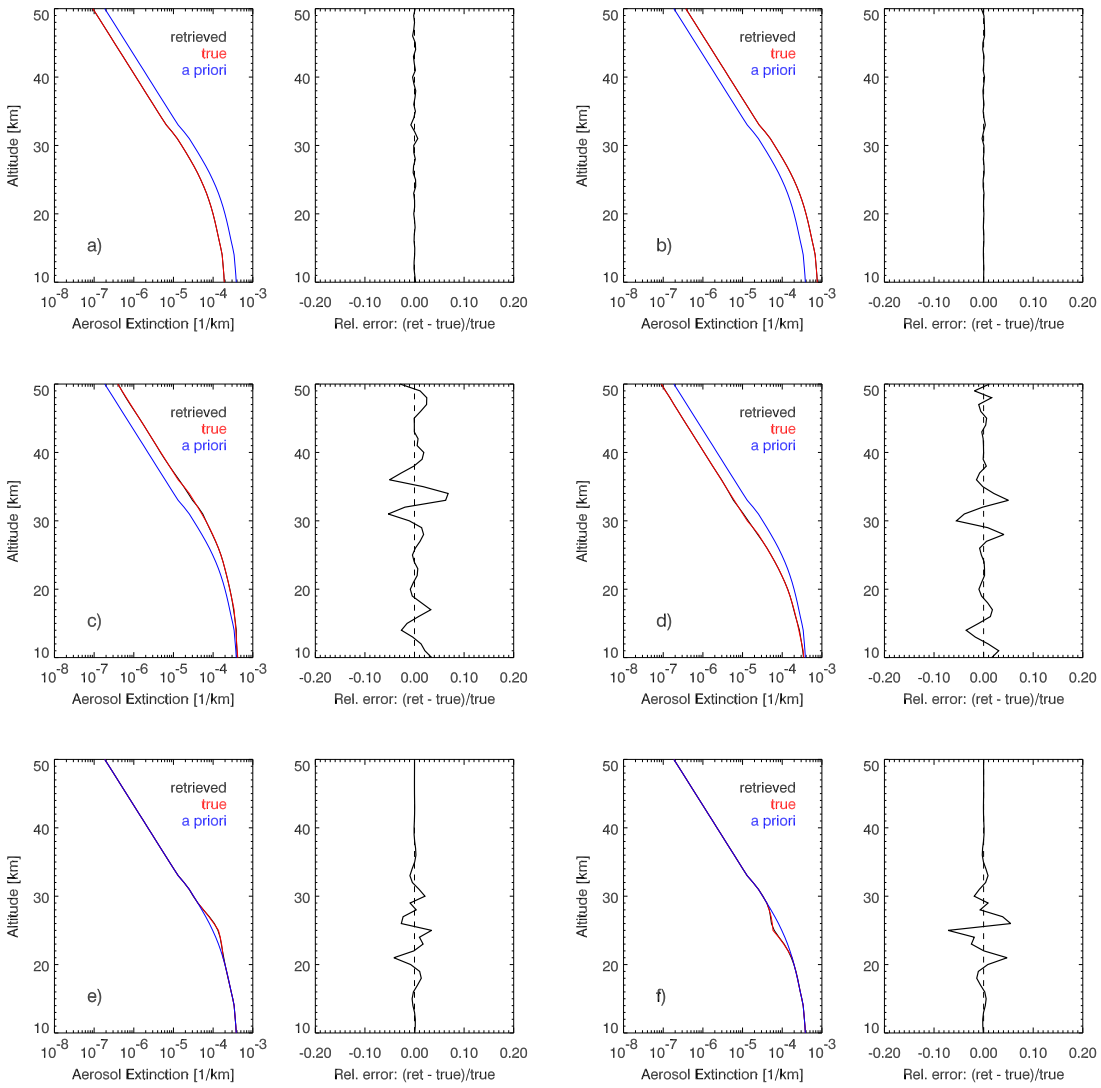

Figure 7.8: As Figure 7.1, but with the Mie phase function described in Section 6.1.2 instead of the Henyey-Greenstein approximation. Left panels: true and a priori aerosol extinction profiles. Right panels: relative difference between the true and the retrieved aerosol extinction profiles. Modifications of the "true" profile in comparison to the a priori profile: a) multiplied by 0.5; b) multiplied by 2; c) altitude shift +3 km; d) altitude shift −3 km; e) artificial maximum around 25 km; f) artificial minimum around 25 km.

7.2.2 Effect of surface albedo

Equivalent to Figure 7.2, Figure 7.9 shows the relative error in the retrieved aerosol extinction coefficient for true albedo values between 0 and 1 with respect to an assumed albedo of 0.5 for the five SCIAMACHY geometries. The two main observations described in Section 7.1.2 – a much higher error in the tropics compared to the polar regions and a much higher sensitivity to the ground albedo in the southern hemisphere – are still visible, but both less pronounced. The reason for this is the reduced sensitivity at the equator and at 40°S, where the absolute value of the largest relative error is reduced by ≈20 %. This is a result of the higher value of the Mie phase function compared to the Henyey-Greenstein approximated one at scattering angles corresponding to these latitudes, which means that less aerosol extinction is needed to compensate for the same error. The changes in the polar regions are small compared to the HG version, the already small relative error at 75°S is even smaller for the Mie phase function. Note again the feature below 20 km at this latitude, a result of the very large solar zenith angle. The sign of the relative error switches between 40°N and the equator, while in the HG version this happens between 83°N and 40°N. This is also a result of the different behaviour in the forward scattering area of the new phase function (see Figure 6.1) that corresponds to single scattering for SCIAMACHY geometries in the northern hemisphere (see Table 5.1). At 40°N, an overestimation or underestimation of the ground albedo would now lead to an aerosol extinction error with different sign than for the HG case, but with relatively small absolute values of generally smaller than 10 % in both cases.

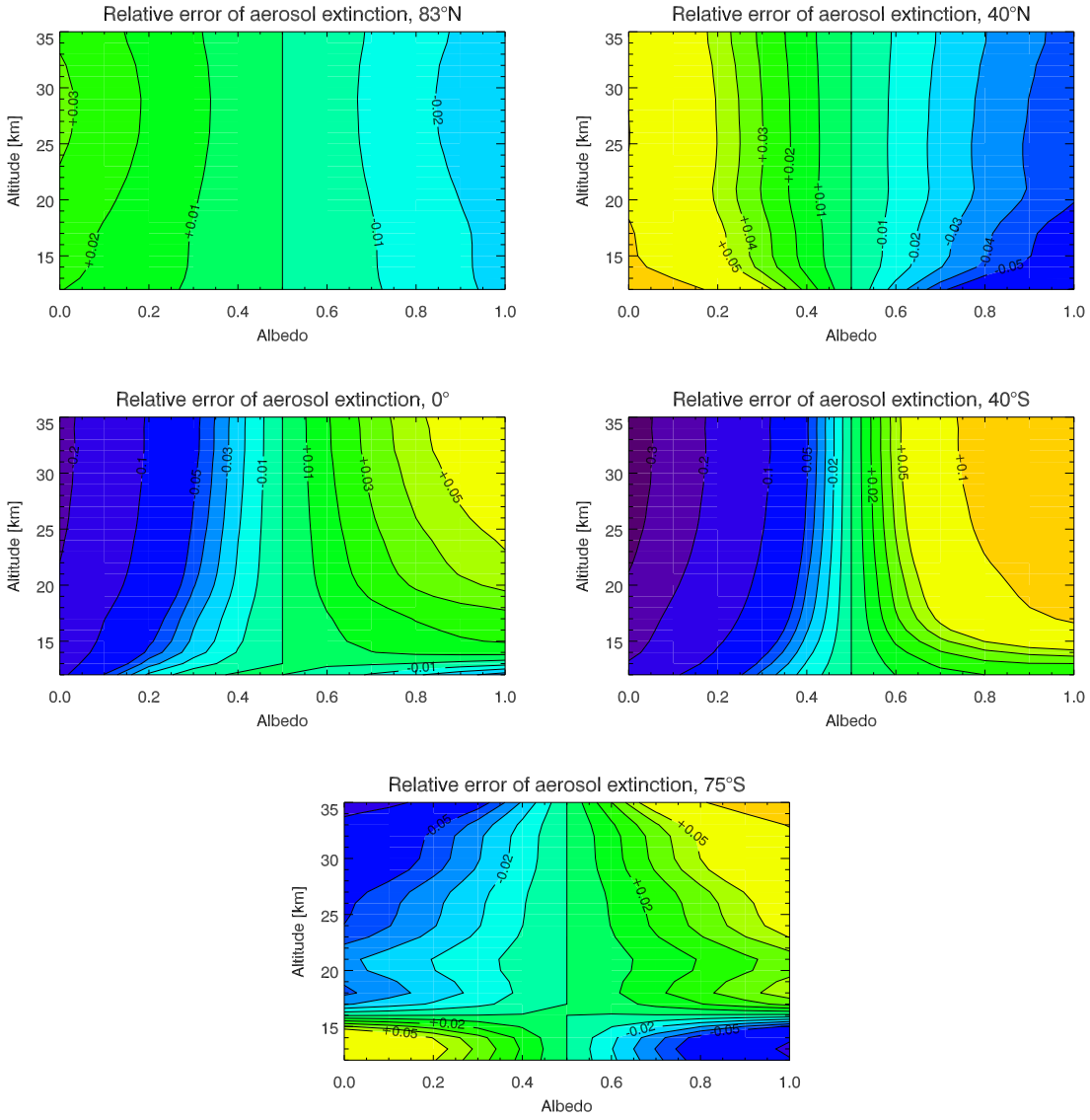

Figure 7.9: As Figure 7.2, but with the Mie phase function described in Section 6.1.2 instead of the Henyey-Greenstein approximation: relative errors in the aerosol extinction coefficients for different values of the true surface albedo A and the SCIAMACHY viewing geometry at 83°N, 40°N, 0°, 40°S, and 75°S. The albedo assumed for the retrieval is A = 0.5.

7.2.3 Effect of neutral density

In Figure 7.10 the relative errors in the retrieved aerosol extinction for artificial errors of ± 3 % in the neutral density – simulated by corresponding changes of the ground pressure, see Section 7.1.3 – are depicted. Compared to the HG version, the errors are similar for 83°N, 40°N, and the equator, and smaller for the two southern latitudes. The largest effect can be seen in altitudes above 35 km at 40°S and below 35 km at 75°S. Above 20 km the error is now ≤ 5 % for all latitudes.

7.2.4 Effect of ozone

Figure 7.11 shows the result for the ozone sensitivity study for the retrieval with a Mie phase function. For the reasons mentioned in Section 7.1.4, the impact of errors in the ozone profile on the retrieved aerosol extinction is negligible, <2 % even for the polar geometry with a high ozone column.

7.2.5 Effect of tropospheric clouds

Figure 7.12 shows the result for the cloud sensitivity study for the retrieval with a Mie phase function. As for the previous parameters, the error in the aerosol extinction is significantly reduced after implementing a Mie phase function. Even for this optically thick cloud layer the relative error at all latitudes except 75°S is rather small, <15 % at all altitudes. The effect of the large solar zenith angle at 75°S is still visible, but not as pronounced as for the Henyey-Greenstein version. A low cloud (1–4 km, red curve) now leads to an overestimation in the aerosol extinction of up to 40 % from above the tropopause to 32 km and an underestimation of up to 40 % above, a high cloud (6–9 km, green curve) to a strong underestimation (up to 60 %) in the aerosol extinction below 16 km and an overestimation of up to 50 % above. (Note that the highest cloud with a CTH of 10 km leads to a failure of the

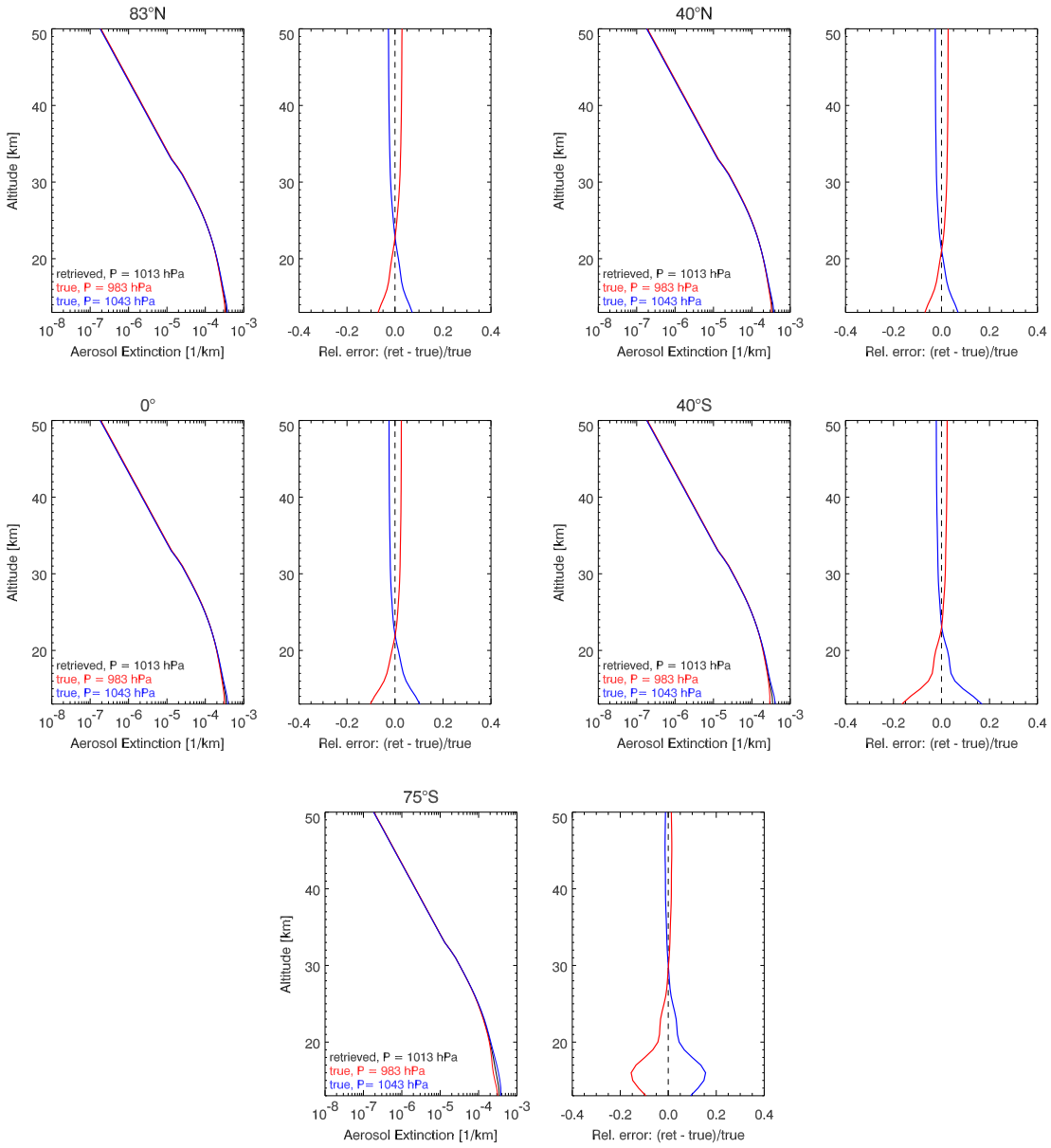

Figure 7.10: As Figure 7.3, but with the Mie phase function described in Section 6.1.2 instead of the Henyey-Greenstein approximation: relative errors in the aerosol extinction coefficients for an error of about ±3 % in the neutral density and the SCIAMACHY viewing geometry at 83°N, 40°N, 0°, 40°S, and 75°S.

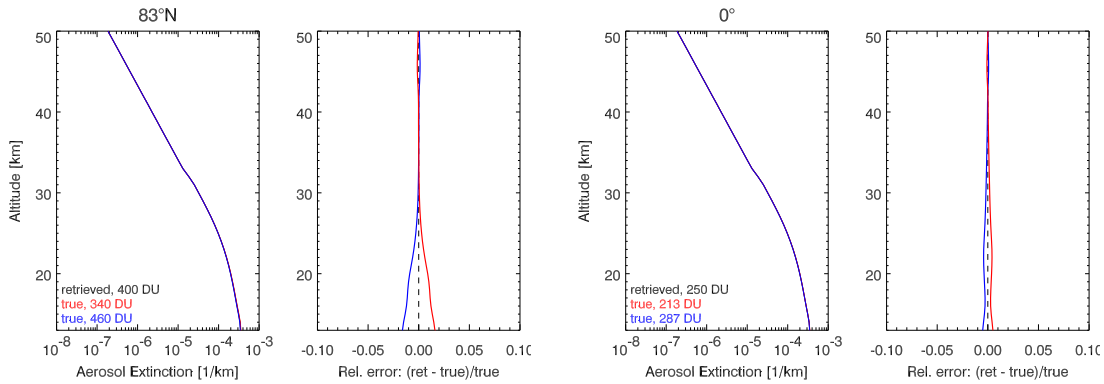

Figure 7.11: As Figure 7.4, but with the Mie phase function described in Section 6.1.2 instead of the Henyey-Greenstein approximation: relative errors in the aerosol extinction coefficients for an error of ± 15 % in the ozone profile for a polar and a tropical SCIAMACHY viewing geometry. Left panel: 83°N, 400 DU ± 15 %; right panel: 0°, 250 DU ± 15 %.

retrieval.) After reducing the SZA to 83° (see last panel in Figure 7.12) the relative error in the aerosol extinction is with ±20 % still relatively large compared to the other latitudes, but much smaller than in retrieval version V1.0.

The comparison with an ice cloud (left set of panels in Figure 7.13) and an optically thinner cloud ($\tau = 10$, right set of panels) at 40°S leads to the same conclusion as for retrieval version V1.0: the aggregation state only plays a minor role with respect to influencing the retrieved aerosol extinction, a smaller optical thickness leads to a smaller error in the aerosol extinction.

7.2.6 Effect of tangent height errors

The results of repeating the sensitivity study for tangent height errors for the Mie phase function are shown in Figure 7.14. The sensitivity of V1.1 is smaller compared to V1.0, the error for the ± 1000 m shift is <20 % above 20 km and <35 % below. For a typical SCIAMACHY tangent height error of ± 200 m, the largest impact on the aerosol extinction is about 6 % at 16 km and <4 % above 20 km.

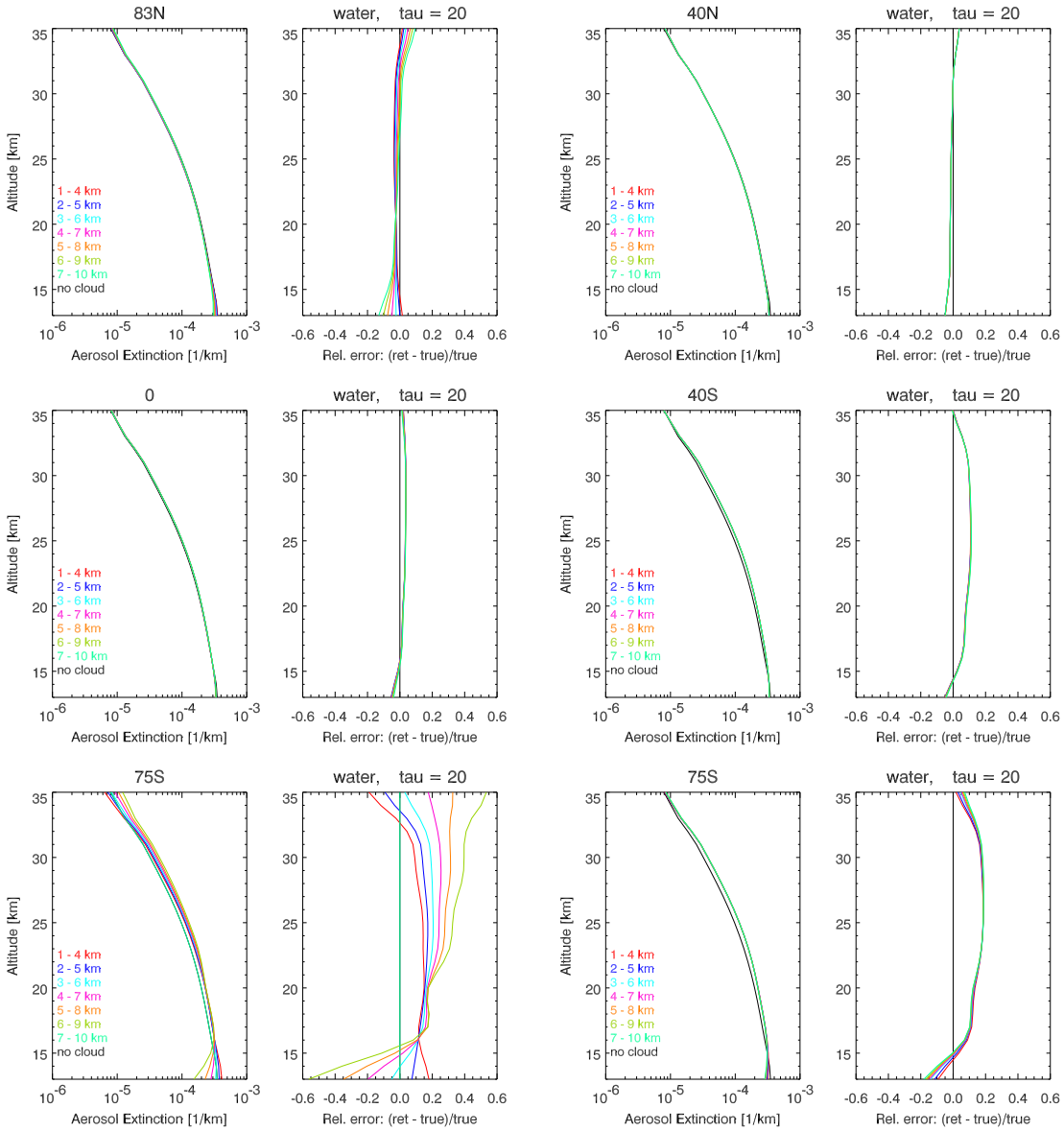

Figure 7.12: As Figure 7.2, but with the Mie phase function described in Section 6.1.2 instead of the Henyey-Greenstein approximation: Relative error in the aerosol extinction (V1.1) for a water cloud layer with 3 km vertical extension and an optical thickness of τ = 20 at seven different altitudes below the retrieval altitude. The first five sets of panels again show aerosol extinction profiles (left panels) and the relative error (right panels) for a SCIAMACHY viewing geometry at 83°N, 40°N, 0°, 40°S, and 75°S as listed in Table 5.1. The last set of panels (bottom right) shows the 75°S geometry with a modified solar zenith angle of 83°S.

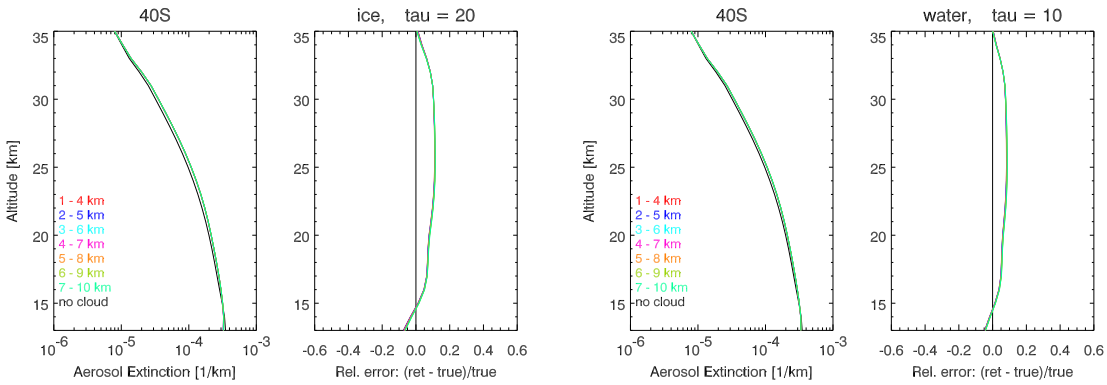

Figure 7.13: Relative aerosol extinction retrieval error for a cloud layer with 3 km vertical extension at seven different altitudes below the retrieval altitude for a SCIAMACHY viewing geometry at 40°S. Left panel: ice cloud with $\tau = 20$. Right panel: water cloud with $\tau = 10$.

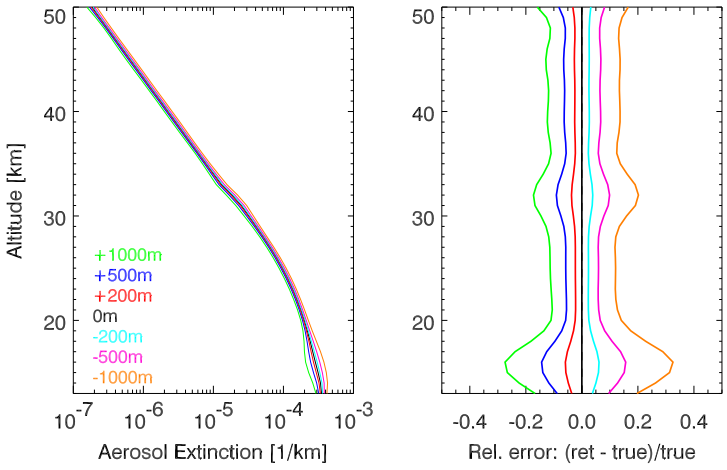

Figure 7.14: As Figure 7.7, but with the Mie phase function described in Section 6.1.2 instead of the Henyey-Greenstein approximation: relative errors in the aerosol extinction coefficients for a tangent height error of ± 200 m, ± 500 m, and ± 1000 m for a northern mid-latitude SCIAMACHY viewing geometry.

7.2.7 Summary of the sources of potential systematic errors

Similar to the Tables 7.1 and 7.2 for the retrieval with a Henyey-Greenstein approximation, the Tables 7.3 and 7.4 summarize the results of the sensitivity studies for the retrieval with a Mie phase function. In general, the retrieval with an implemented Mie phase function is much less sensitive to errors in other geophysical parameters than the Henyey-Greenstein version. Especially in the southern hemisphere the effect is apparent, the error induced by the same uncertainty in a geophysical parameter is reduced by a factor 2. As a result, the difference in sensitivity between the two hemispheres – visible most clearly comparing Figure 7.2 and Figure 7.9 – is reduced significantly.

The largest source for errors are uncertainties in the knowledge of neutral density (15 % error at most), tropospheric clouds (9 %) and ground albedo (8 %) in the southern hemisphere, followed by the a priori profile (7 %), tangent height registration (6 %), and ozone (<1 %).

Alt. [km]	**83°N**			**40°N**			**0°**			**40°S**			**75°S**		
	A	**ND**	**Cl.**	**A**	**ND**	**Cl.**	**A**	**ND**	**Cl.**	**A**	**ND**	**Cl.**	**A**	**ND**	**Cl.**
15	<1	5	1	1	4	3	<1	7	1	4	8	2	1	15	4
20	<1	1	1	1	0	2	1	1	2	6	2	6	1	4	8
25	<1	0	1	1	1	1	1	1	3	7	0	9	2	2	9
30	<1	2	1	1	2	0	2	2	3	7	2	8	2	0	8
35	<1	2	1	1	2	3	2	2	1	8	2	0	4	1	2
Mean	<1	2	1	1	2	2	1	3	2	6	3	5	2	4	6

Table 7.3: As Table 7.1, but with a Mie phase function instead of the Henyey-Greenstein approximation: absolute value of the relative error [%] of the aerosol extinction (V1.1) due to uncertainties in ground albedo ("A", uncertainty 0.15) and neutral density ("ND", 3 %) and due to a typical tropospheric cloud ("Cl.") for the SCIAMACHY viewing geometry at 83°N, 40°N, 0°, 40°S, and 75°S.

Alt. [km]	O3		TH
	83°N	0°	40°N
15	1	0.5	6
20	1	0.5	2
25	0	0.5	2
30	0	0	3
35	0	0	2
Mean	0.5	0.5	3

Table 7.4: As Table 7.2, but with a Mie phase function instead of the Henyey-Greenstein approximation: absolute value of the relative error [%] of the aerosol extinction (V1.1) due to uncertainties in the ozone profile (15 %) and tangent height (200 m) for the SCIAMACHY viewing geometry at 83°N and 0° and 40°N, respectively.

Part III

Retrieval results

8 Comparison with SAGE II data

After testing the sensitivity of the algorithm to various parameters, we applied the retrieval approach described in Section 5.1 to the entire SCIAMACHY data set of limb-scatter observations from August 2002 – April 2012. To demonstrate the quality of the algorithm, we validated our results with co-located SAGE II measurements. As described in Section 1.1, the SAGE solar occultation instrument series and particularly SAGE II provided a stratospheric aerosol extinction data set which is widely regarded as highly accurate and therefore well suited for the validation of the SCIAMACHY results presented here. One of the data products of SAGE II are aerosol extinction profiles at 525 nm wavelength. We converted the SCIAMACHY stratospheric aerosol extinction values to this wavelength using the assumed spectral dependence of the aerosol extinction coefficient with Ångstrøm exponents delivered by SCIATRAN, approximately 1.54 for V1.0 and 1.43 for V1.1. The 525 nm profiles were then compared to co-located SAGE II profiles within a spatial distance of 500 km and a temporal difference of six hours at most during the temporal overlap of the two missions between 01 January 2003 (start of the SCIAMACHY routine operations phase) and 17 August 2005 (demise of SAGE II). SCIAMACHY data with a SZA exceeding 87° were not considered in this comparison.

Recently a new version (V7.0) of the SAGE II aerosol extinction data set has been published (Damadeo et al., 2013). Changes in the algorithm and meteorological data used to derive the aerosol extinction from the occultation measurements led to significant differences in the 525 nm aerosol extinction compared to V6.2 published

in 2003, particularly above 20 km altitude. In this chapter both SCIAMACHY versions V1.0 and V1.1 are compared with both SAGE II versions V6.2 and V7.0.

The first part of this chapter deals with retrieval version V1.0 containing the Henyey-Greenstein phase function. In the second part, the same procedure is repeated with the Mie phase function (retrieval version V1.1) and the results are compared to V1.0. To investigate the effect of clouds on the retrieval, the comparisons of both retrieval versions are additionally shown in the corresponding section using cloud occurence information that is also obtainable from SCIAMACHY radiance spectra.

8.1 Henyey-Greenstein approximation

Figure 8.1 shows the comparison – mean profiles and relative differences (SCIAMACHY −SAGE)/SAGE – of the globally averaged SAGE II V6.2 (black) and V7.0 (blue) with SCIAMACHY stratospheric aerosol extinction profiles V1.0 (red) at 525 nm wavelength. Below 15 km, SCIAMACHY overestimates the aerosol extinction by up to 40 % as compared to both versions of SAGE II. But above 15 km the agreement to V6.2 is within 20 % and between 16 and 30 km even within about 10 %. Compared to V7.0, SCIAMACHY overestimates the stratospheric aerosol extinction by approximately 20 % between 15 and 32 km.

To gain more information about the meridional behavior of the retrieval, the profiles were averaged zonally and over all available co-locations as well as binned into eight 20° latitude bins between 80°N and 80°S (Figure 8.2). Table 8.1 shows the relative differences of the retrieved aerosol extinction in comparison to co-located SAGE II measurements for the eight latitude bins. Between 20°N and 20°S values for 15 km altitude have been ignored because of tropospheric influences at these latitudes. For the same reason, the 15 km values for 20–40° N/S are put in

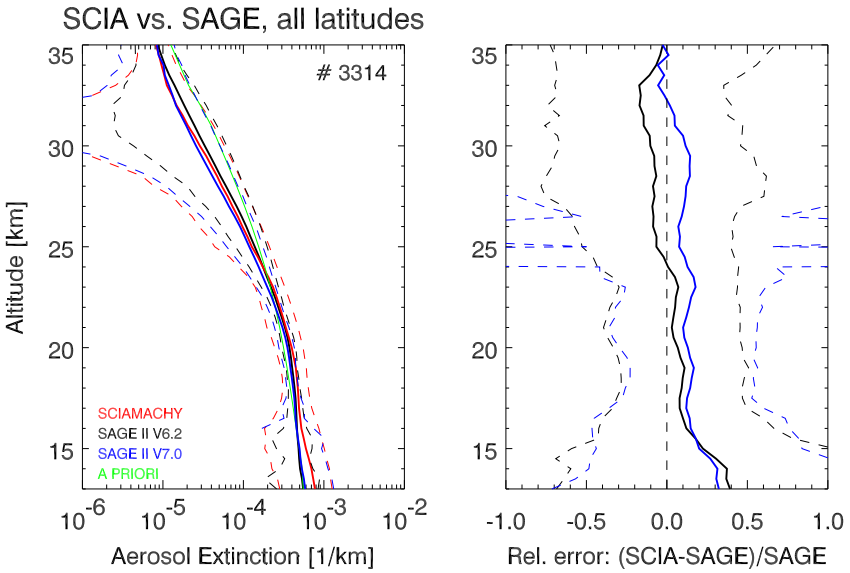

Figure 8.1: Left panel: comparison of average co-located SAGE II V6.2 (black)/V7.0 (blue) and SCIAMACHY (red) 525 nm aerosol extinction profiles (V1.0) with standard deviation (dashed lines). The green line shows the a priori extinction profile used for the SCIAMACHY retrievals. The number in the top right corner shows the number of co-locations averaged. Right panel: mean relative difference between SCIAMACHY and both versions of SAGE II aerosol extinction profiles with standard deviation (dashed).

parentheses. In the following, first the comparison to V6.2 (black curves in Figure 8.2) is discussed.

At low latitudes (20°N–20°S) the agreement is quite good above 20 km altitude. Above the tropopause the relative difference is generally smaller than 20 % in both hemispheres. Above 20 km altitude the SCIAMACHY aerosol extinctions in the southern hemisphere are up to 20 % larger than the SAGE II values. Below 20 km the frequent occurrence of tropospheric clouds makes SCIAMACHY and SAGE II products uncomparable. An analysis of the tropospheric cloud detection data set obtained with SCODA (SCIAMACHY ClOud Detection Algorithm) (Eichmann et al., 2009) showed that about 95 % of all SCIAMACHY limb measurements are affected by tropospheric clouds.

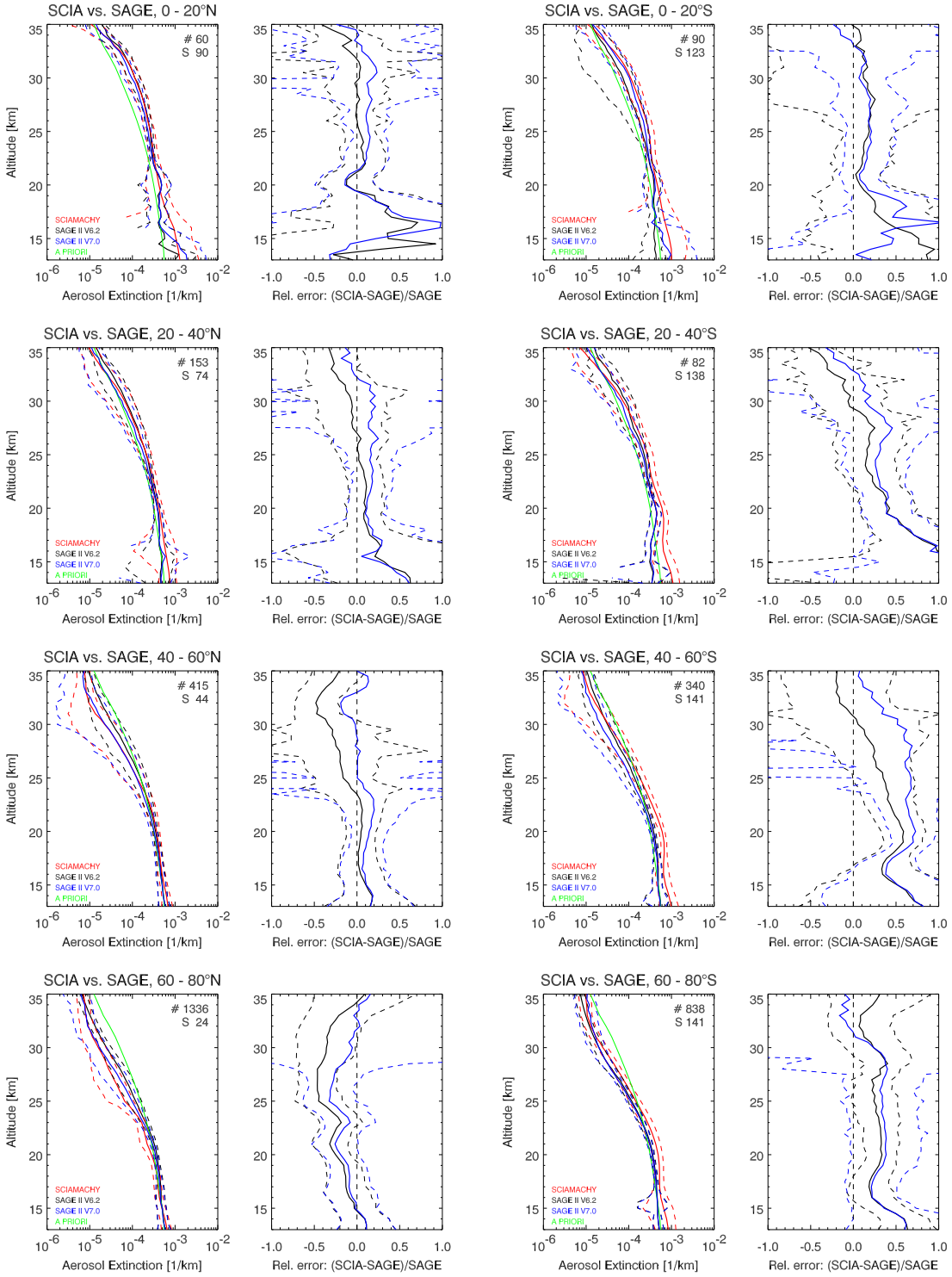

Figure 8.2: Left panels: comparison of the retrieved (V1.0) 525 nm aerosol extinction profiles (red) with SAGE II V6.2 (black) and V7.0 (blue) aerosol extinction in eight latitude bins with standard deviation (dashed lines). The a priori profile is shown in green. The numbers in the top right corner show the number of co-locations averaged ("#") and the average scattering angle ("S"). Right panels: mean relative difference between SCIAMACHY and both versions of SAGE II aerosol extinction profiles with standard deviation (dashed).

Alt. [km]	60–80°N		40–60°N		20–40°N		0–20°N		0–20°S		20–40°S		40–60°S		60–80°S	
	6.2	7.0	6.2	7.0	6.2	7.0	6.2	7.0	6.2	7.0	6.2	7.0	6.2	7.0	6.2	7.0
15	0	0	10	10	(30)	(25)	-	-	-	-	(> 100)	(> 100)	50	50	35	35
20	−20	−20	5	15	10	10	−10	−10	5	15	40	40	60	70	35	40
25	−45	−30	−15	0	0	15	5	15	20	20	15	30	35	65	25	35
30	−35	−5	−35	0	−5	15	0	15	10	10	−5	15	5	50	25	25
Mean	−25	−15	−10	5	0	15	0	10	10	15	15	30	40	60	30	35

Table 8.1: Relative difference [%] of the SCIAMACHY aerosol extinction in comparison to co-located SAGE II **V6.2** and **V7.0** measurements, both averaged in eight latitude bins. The Henyey-Greenstein approximation for the phase function was used (V1.0).

Between 20°N and 40°N, the relative differences are generally within ± 20 %. Only above 30 km and below 17 km the differences are larger. In the corresponding region in the southern hemisphere, the shape of the relative difference profile is similar, but the values are larger than in the northern hemisphere, ranging from −50 % at 35 km altitude to +100 % near 15 km. However, between 20 and 30 km, the difference is generally within ± 20 %. The large error below 20 km might still be an effect of tropospheric clouds.

Between 40°N and 60°N, the agreement is quite good below 25 km with relative differences to SAGE of ± 20 % at most. Above 25 km, SCIAMACHY results are systematically lower than those of SAGE II, e. g., by about 50 % at 32 km. The picture of the corresponding latitude bin in the southern hemisphere looks completely different. At all altitudes below 30 km, we see systematically higher values. At 20 km the relative difference reaches 60 %.

For latitudes between 60° and 80° we observe a significant interhemispheric difference in the relative differences between SCIAMACHY and SAGE II aerosol extinction profiles. In the northern hemisphere the relative differences are negative for all altitudes between 15 and 34 km (with a maximum difference of about −50 % between 25 and 30 km), whereas they are positive for all altitudes in the southern

hemisphere remaining more or less constant at about +30 % between 15 and 30 km.

Summarized, the good globally averaged agreement of SCIAMACHY V1.0 with SAGE II V6.2 gets bad on closer inspection of the latitudinal behavior.

The comparison with SAGE II V7.0 (blue curves in Figure 8.2) looks slightly different, but not better. The difference at almost all latitudes and altitudes is shifted towards more positive values by approximately 5–10 %. This leads to worse agreement in all latitude bins except the ones representing mid and high northern latitudes (40°–80°N). The overall picture and therefore the following interpretation is valid for both SAGE II versions.

In general it can be said that the SCIAMACHY retrieval results in lower stratospheric aerosol extinction in the northern hemisphere and higher values in the southern hemisphere as compared to SAGE II measurements (see Figure 8.3). One possible reason for this apparent interhemispheric difference is the different sensitivity of the aerosol profile retrievals to errors in the surface albedo (see Section 7.1.2, in particular the comparison of 40°N and 40°S in Figure 7.2). Tropospheric clouds affect the majority of the SCIAMACHY limb observations, and this will lead to a higher effective albedo at 470 nm and 750 nm as compared to the surface albedo data base by Matthews (1983) currently used by SCIATRAN for the retrieval. This is particularly true for measurements above the ocean. A low bias in the assumed albedo is most commonly associated with high bias in the aerosol extinction values, and this effect is much stronger in the southern hemisphere. This is qualitatively consistent with the validation results presented in Figure 8.2 – particularly considering the comparisons for 40°–60° N/S and 60°–80° N/S.

This aspect was investigated further by applying the SCODA cloud detection data base (Eichmann et al., 2009) in order to exclude SCIAMACHY measurements from the comparison that were affected by clouds in the troposphere. The left panels in Figure 8.4 show the relative difference between SCIAMACHY and SAGE II aerosol

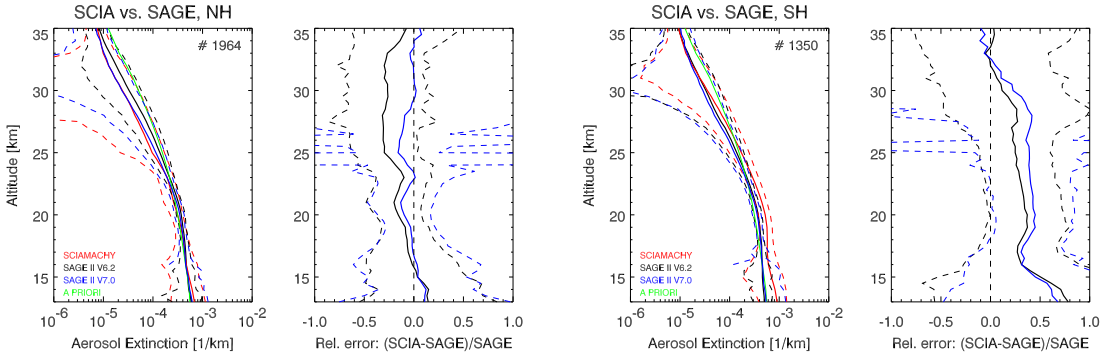

Figure 8.3: Mean relative difference between SCIAMACHY V1.0 (red) and SAGE II V6.2 (black)/V7.0 (blue) 525 nm aerosol extinction profiles with standard deviation (dashed) for the northern (left panel) and southern (right panel) hemisphere.

extinction profiles for all co-locations in the southern hemisphere without cloud filter applied. The right panels show the relative difference with all SCIAMACHY measurements removed that were affected by clouds. Unexpectedly, the cloud filtering does not improve the agreement between SCIAMACHY and both versions of SAGE II aerosol extinction, and we conclude that the overestimation of stratospheric aerosol extinction by SCIAMACHY in the southern hemisphere must have other reasons.

8.2 Mie phase function

The comparison of the V1.0 and the V1.1 sensitivity studies (described in Section 7.2.7) made clear that the choice of the phase function is crucial for the quality of the retrieval, particularly with regard to the interhemispheric difference shown above. Since the basic microphysical parameters of background stratospheric aerosols are established – refractive index of sulfuric acid/water mixture in spherical shape with particle radii of approximately 0.1 micron – it is the obvious next step to implement a Mie phase function in the retrieval. We implemented the aerosol phase function

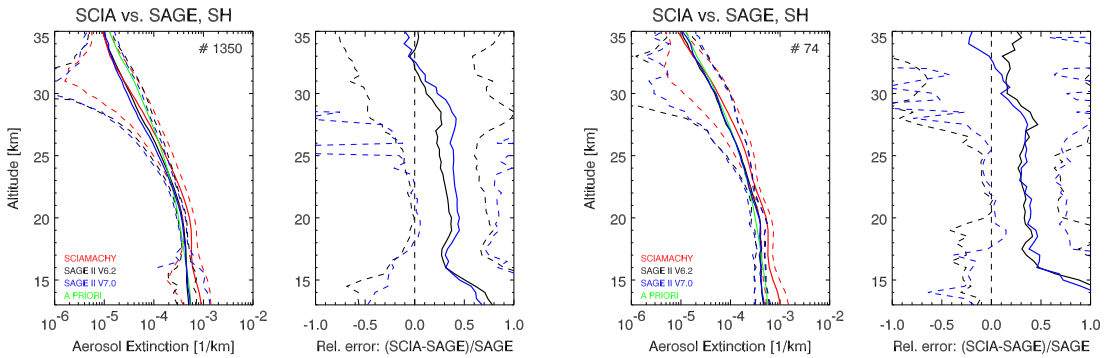

Figure 8.4: Comparison of SCIAMACHY V1.0 (red) and SAGE II V6.2 (black)/V7.0 (blue) aerosol extinction profiles at 525 nm wavelength for southern hemisphere co-locations only. Left panels: no cloud screening applied. Right panels: only SCIAMACHY observations not affected by tropospheric clouds are used.

Alt. [km]	60–80°N		40–60°N		20–40°N		0–20°N		0–20°S		20–40°S		40–60°S		60–80°S	
	6.2	7.0	6.2	7.0	6.2	7.0	6.2	7.0	6.2	7.0	6.2	7.0	6.2	7.0	6.2	7.0
15	10	10	10	10	(20)	(15)	-	-	-	-	(80)	(70)	10	10	5	5
20	0	5	5	15	−10	−5	−30	−30	−20	−20	−5	−5	0	5	−5	0
25	−40	−25	−15	0	−20	−5	−25	−20	−30	−20	−25	−20	−15	−5	−10	0
30	−50	−30	−35	0	−25	−5	−30	−20	−40	−30	−40	−25	−15	20	25	25
Mean	−20	−10	−10	5	−15	0	−30	−25	−30	−25	−20	−15	−5	10	5	5

Table 8.2: As Table 8.1, but with a Mie phase function used for the retrieval (V1.1).

for r = 0.11 µm explained in Section 6.1.2 and depicted in Figure 6.1 instead of the Henyey-Greenstein approximation in the retrieval and repeated the retrievals for the measurements co-located with SAGE II, leaving all other parameters unchanged.

Figure 8.5 shows the results for the same eight latitude bins, summarized in Table 8.2. Note that for the comparison with SAGE II the aerosol extinction at 525 nm is calculated by linearly interpolating the phase functions displayed in Figure 6.1, thus the phase function is similar to that shown in the upper panel of Figure 6.1.

As for the Henyey-Greenstein version, first the comparison of SCIAMACHY V1.1 to the older SAGE II V6.2 is discussed, followed by the comparison to SAGE II V7.0.

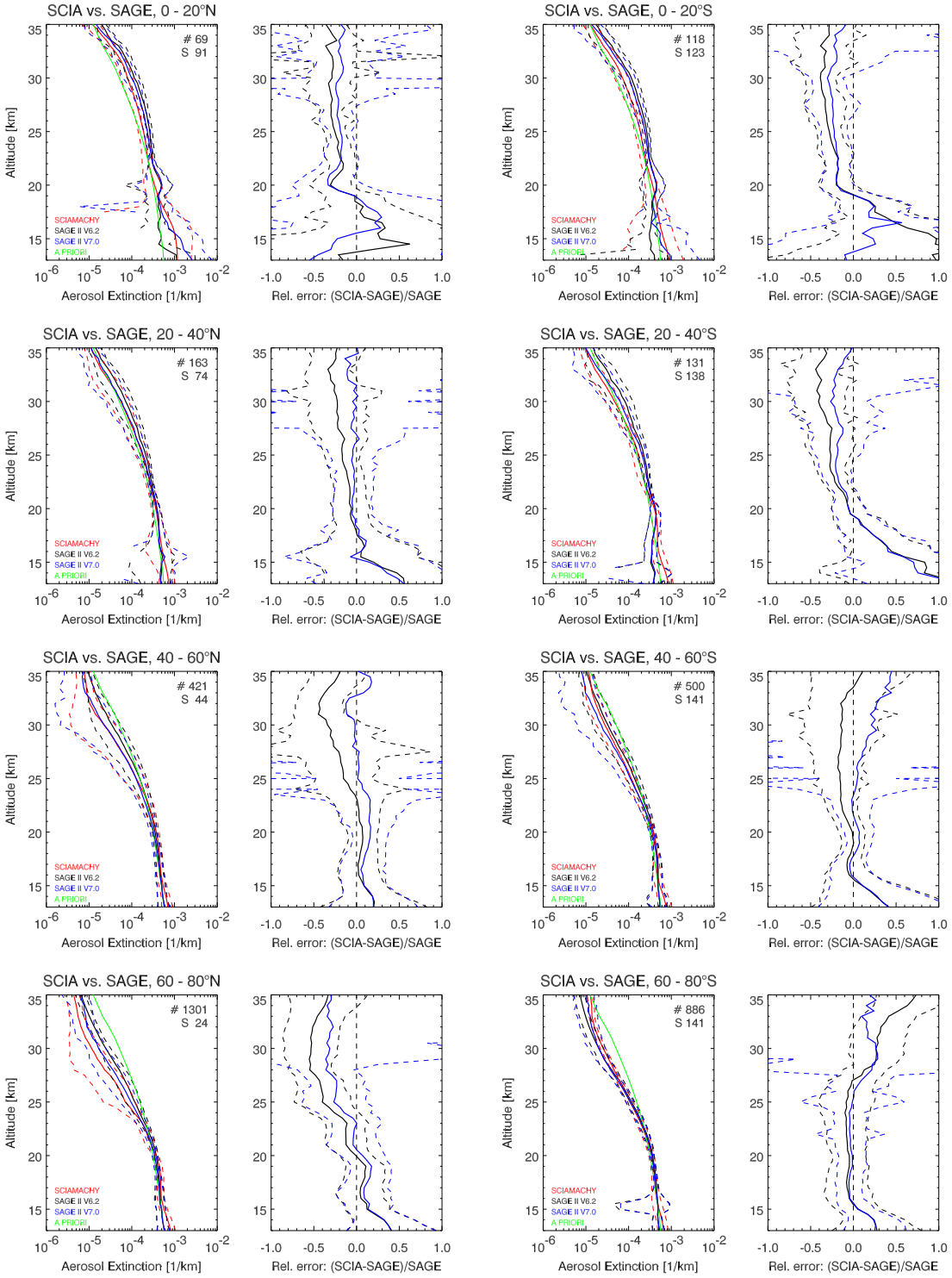

Figure 8.5: As Figure 8.2, but retrieved with a Mie phase function with r = 0.11 μm and σ = 1.37 (V1.1, red curves) instead of a Henyey-Greenstein approximation (V1.0). The black curves again correspond to SAGE II V6.2, the blue curves to SAGE II V7.0.

Compared to the HG version (see Figure 8.2), we see a shift of the relative difference towards negative values at all latitude bins between 40°N and 40°S. While for the two 20–40° bins it is difficult to say whether the result is better or worse than for the Henyey-Greenstein version, it is definitely worse for latitudes around the equator (20°N–20°S). Above the tropopause at approximately 20 km altitude, the relative difference is now around −30 % in both bins, compared to +20 % (0–20°S) and around 0 % (0–20°N).

The results at mid and high southern latitudes (40–80°S) are much closer to the SAGE II extinctions. Between 15 and 27 km altitude, the difference to SAGE II lies between −10 and −20 %, compared to +30 to +60 % for V1.0. At the same latitudes in the northern hemisphere, the quality of the retrieval remains more or less the same. Between 60°N and 80°N and at 15–23 km the difference to SAGE II is slightly smaller (−15 to +10 %), while above the difference grows to a maximum of −50 %. Between 40° and 60°N, there is almost no difference to the Henyey-Greenstein version, most probably because of the very similar phase function values at the scattering angles corresponding to this latitude bin (see vertical lines in Figure 6.1).

Summarized, the comparison with V6.2 of SAGE II data showed that the application of a Mie phase function improved the SCIAMACHY stratospheric aerosol extinction data set drastically.

The SCIAMACHY aerosol extinction profiles are in even better agreement with SAGE II retrievals, if the new version V7.0 is used rather than V6.2. At all latitudes and almost all altitudes, the difference of SCIAMACHY V1.1 to SAGE II V7.0 (blue curves in Figure 8.5) is smaller than to V6.2. In the equatorial region (20°N–20°S) the picture is qualitatively the same, but the underestimation by SCIAMACHY above the tropopause is reduced from 30 to 20 %. At 20°–40°N, the difference to SAGE II is now close to 0 % above 15 km. The negative offset above 20 km at 20°–40°S is reduced from ≈30 to ≈15 %. At mid and high northern latitudes (40°–80°N), the

large negative difference above 20 km is reduced drastically, particularly at 40-60°N. While at this latitude bin the formerly large difference to SAGE II is now around 0 % at these altitudes, the positive difference below gets slightly larger to ≈20 %. At 60°–80°N, the picture is similar, but next to the now slightly larger positive difference at low altitudes a relatively large negative difference of up to −35 % at high altitudes remains. In the corresponding part of the southern hemisphere (40°–80°S), between 15 and 27 km the good agreement in both 20° bins is even better now, within ±10 % at 40°–60°S and even within ±5 % at 60°–80°S. Above 27 km at 40°–60°S SCIAMACHY now overestimates the aerosol extinction compared to SAGE II. The large overestimation compared to V6.2 at 60°–80°S in this altitude region is reduced.

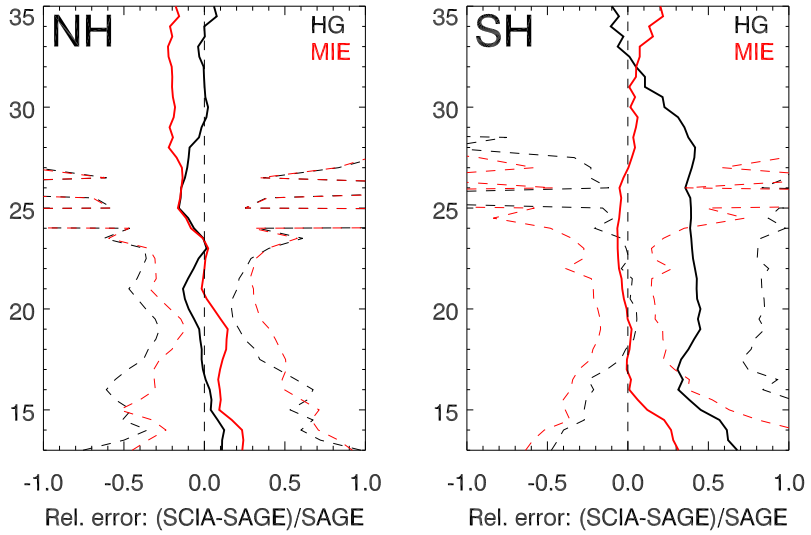

Figure 8.6: Mean relative difference between SCIAMACHY and SAGE II V7.0 aerosol extinction profiles with standard deviation (dashed) for the northern (left panel) and southern (right panel) hemisphere. The black curve shows the result for retrieval with a Henyey-Greenstein phase function (V1.0), the red one the version with a Mie phase function (V1.1).

Figure 8.6 shows the hemisphere-averaged relative differences of the retrieval results with respect to SAGE II V7.0 for both the Henyey-Greenstein version and the Mie version. The interhemispheric difference is significantly smaller for the Mie case with a much better agreement to SAGE II in the southern hemisphere and a qualitatively unchanged difference in the northern hemisphere.

The globally averaged relative difference for all co-locations retrieved with V1.1 (see Figure 8.7) reflects this improvement. For all altitudes above 15 km the relative difference to SAGE V7.0 (blue curve) is within ±10 %.

Figure 8.8 indicates that applying a cloud filter as shown for the southern hemisphere in Figure 8.4 does not have a large effect on the agreement between SCIAMACHY V1.1 and SAGE II aerosol extinction.

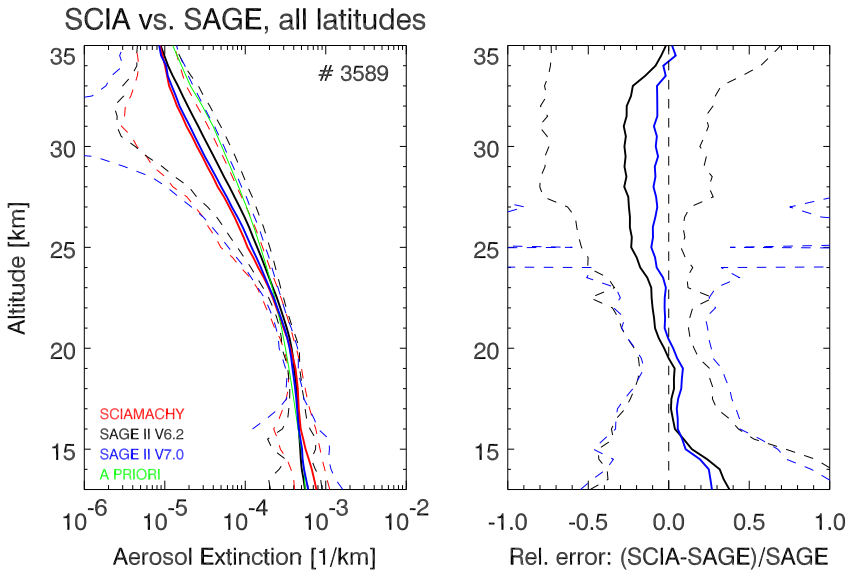

Figure 8.7: Global averaged relative difference to SAGE II V6.2 (black)/V7.0 (blue), as Figure 8.1, but retrieved with a Mie phase function with r = 0.11 µm and σ = 1.37 (V1.1) instead of a Henyey-Greenstein approximation.

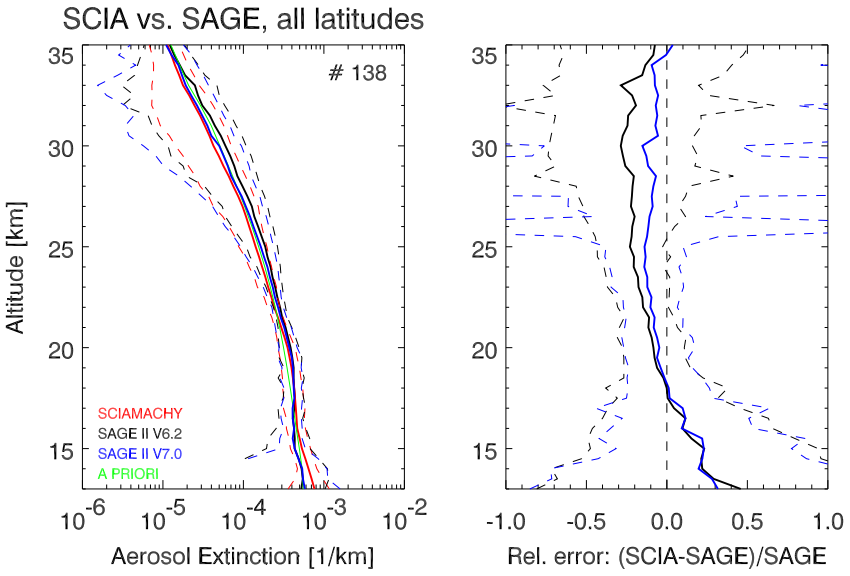

Figure 8.8: As Figure 8.7, but global average of cloud-free cases.

8.3 Comparison with previous results

In this section it is briefly discussed how the comparisons with SAGE II in this study compare to the results presented by Taha et al. (2011) and Ovigneur et al. (2011). Both of these studies also used SCIAMACHY limb measurements to infer stratospheric aerosol profiles.

Taha et al. (2011) used the Ozone Mapper and Profiler Suite, Limp Profiler (OMPS/LP) algorithm to derive aerosol extinction coefficients from normalized SCIAMACHY limb radiances at specific wavelengths assuming a particle size distribution with 0.06 μm mode radius and a variance of 1.73. A comparison with 120 co-located SAGE II V6.2 measurements within 250 km and 24 h find a systematic negative bias of the SCIAMACHY aerosol extinction profiles relative to SAGE II of about 25 %.

Ovigneur et al. (2011) present comparisons with co-located SAGE II measurements for two different values of the particle mean radius (0.15 and 0.35 micron). 2000 co-locations with SAGE II V6.2 have been investigated with co-location criteria of ± 300 km along flight direction and ± 115 km across flight direction, and a time difference of less than 12 h. In this study, the root mean square difference with respect to SAGE II is on the order of 30–50 % with a minimum of 30 % around 22 km.

9 Global stratospheric aerosol extinction data set

As already mentioned, this work focuses on the development, implementation, and testing of the retrieval algorithm. In this chapter, we will have a quick view into the resulting global SCIAMACHY stratospheric aerosol extinction data set to get an impression of the capabilies of the retrieval method by delivering an explanatory approach for the patterns seen in different pressure levels. A detailed investigation of the connections indicated here are not part of this work and must be object of future studies.

The Figures 9.1 and 9.3 show the time and latitude dependence of the retrieved SCIAMACHY aerosol extinction V1.1 at 525 nm on three pressure levels for the complete SCIAMACHY data set from August 2002 – April 2012. ECMWF reanalysis data were used to interpolate the date from the SCIATRAN altitude grid onto these pressure levels. The data were monthly averaged and binned into 5° latitude bins. White areas show regions were no aerosol extinctions could be retrieved due to the lack of SCIAMACHY limb radiance measurements during polar winter.

The aerosol extinction at the 70 hPa level (Figure 9.1), corresponding to an altitude of approximately 18 km, shows clear evidence for the occurrence of polar stratospheric clouds (PSCs) during each hemispheric winter at polar latitudes. These signals are particularly pronounced in the otherwise undisturbed southern polar region after the end of the polar winter (white areas). Note that even if PSCs are

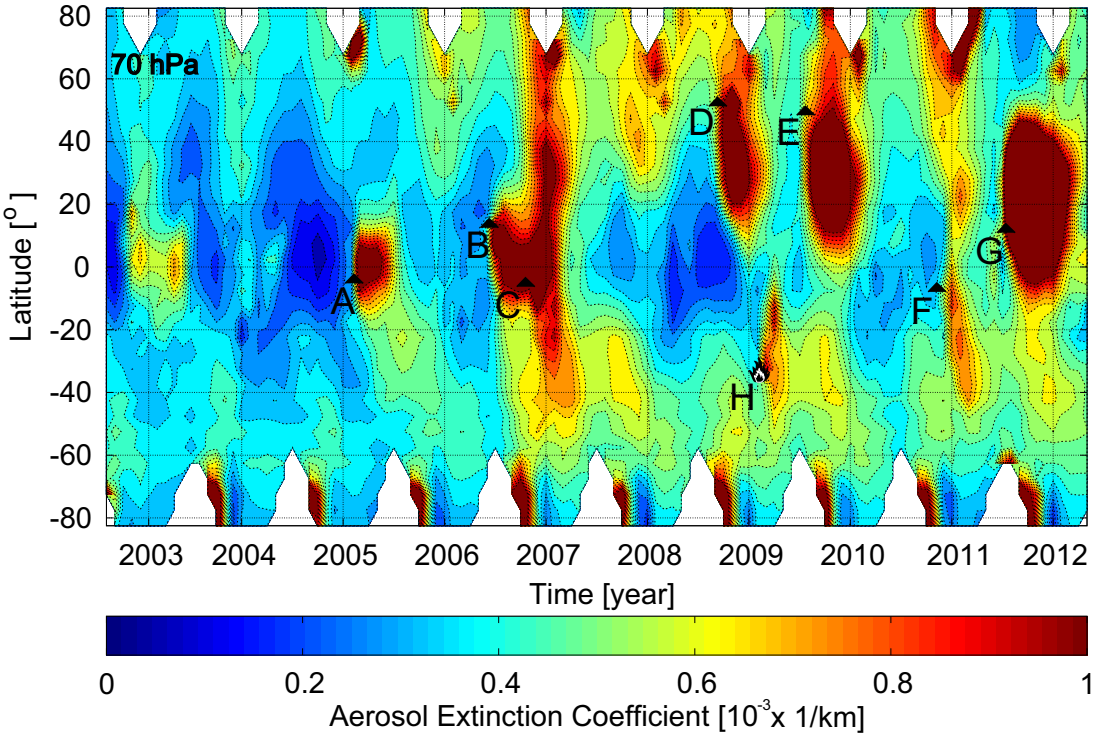

Figure 9.1: Temporal and latitude variation of stratospheric aerosol extinction at 70 hPa (approximately 18 km altitude) retrieved from SCIAMACHY limb-scatter observations. Volcanic eruptions indicated by strong stratospheric aerosol extinction signals: (A) Manam (Jan. 2005, 4°S); (B) Soufriere Hills (May 2006, 16°N); (C) Tavurvur (Oct. 2006, 4°S); (D) Kasatochi (Aug. 2008, 52°N); (E) Sarychev Peak (June 2009, 48°N); (F) Mount Merapi (Oct. 2010, 7°S); (G) Nabro (June 2011, 13°N). (H) indicates the Australian bush fires in Feb. 2009 at 38°S (figure prepared by Lena A. Brinkhoff, IUP Bremen).

present the retrievals are performed with the standard assumption on the aerosol phase function based on the microphysical properties of background aerosols, i.e., the derived extinction values are subject to potentially large systematic errors and only serve as a qualitative indicator for the presence of PSCs. As described in Section 1.2.2, volcanic eruptions can have a strong impact on the number density and the composition of stratospheric aerosol particles if they eject a significant amount of SO_2 and are explosive enough to inject it into the stratosphere. Seven volcanic

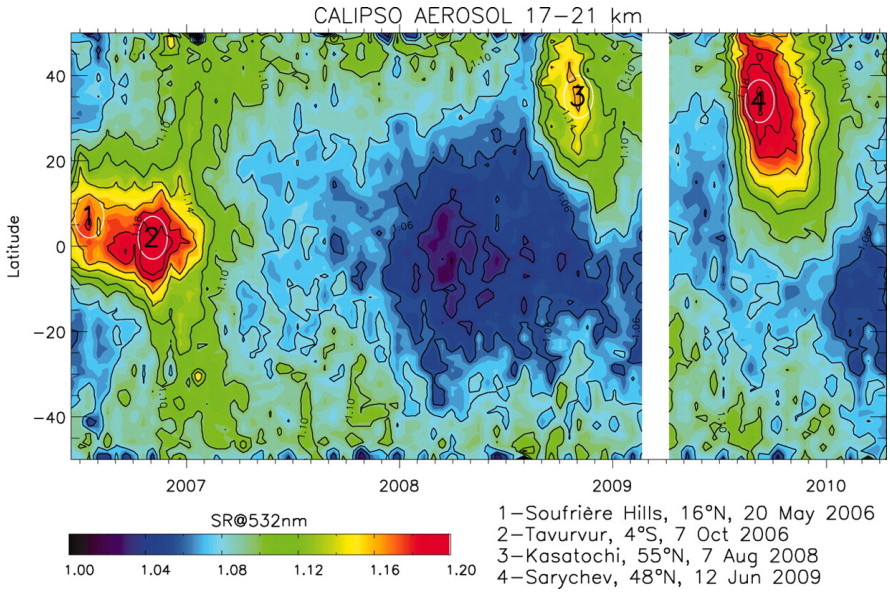

Figure 9.2: Evolution of the zonal mean scattering ratio at 532 nm between 17 and 21 km from the CALIPSO lidar measurements from June 2006 to April 2010. Plumes with scattering ratios greater than 1.15 that are observed in the tropics and at mid-latitudes are linked to the indicated volcanic eruptions (figure from Solomon et al. (2011)).

eruptions with stratospheric impact are clearly identifiable by their aerosol signal at this pressure level, starting with the Manam eruption in January 2005 after a quiescent period during the first years of SCIAMACHY measurements. Five of these eruptions happened in the tropics and two within one year in the northern mid-latitudes. See the caption of the Figure for further information about the time and latitude of the eruptions denoted by the letters A–G in Figure 9.1. The stratospheric aerosol morphology between the eruptions of Tavurvur in October 2006 and Kasatochi in August 2008 with the minimum in the tropics in 2008 agrees very well with the evolution of the zonal mean scattering ratio at 532 nm between 17 and 21 km from CALIPSO lidar measurements shown in Solomon et al. (2011) (see Figure 9.2).

Furthermore, there is evidence of a stratospheric aerosol signal caused by pyro-

convection (see end of Section 1.2.2) above the Australian bush fires in February 2009 (e.g., Siddaway and Petelina, 2011). As in the case of PSCs one should keep in mind that the assumed aerosol phase function is not representative for a volcanically or pyroconvectively enhanced stratospheric aerosol load. Investigations concerning the implementation of a volcanic stratospheric aerosol particle size distribution in the retrieval process should be content of future work.

At the 20 hPa pressure level (top panel of Figure 9.3, approximately 26 km altitude), the PSC signal is still visible, but much less pronounced than in 70 hPa. The dominating feature is an annual pattern in the tropics with a seasonal shift of the maximum of the aerosol load towards the winter hemisphere, i.e., around December/January in the northern hemisphere and around July in the southern hemisphere. This annual variation is consistent with the annual variation in lidar backscatter ratio observed at Boulder (40°N) and Hawaii (19°N) (Hofmann et al., 2009). This behaviour can be explained by the meridional transport processes within the Brewer-Dobson-Circulation steered by the westerly and easterly shears of the QBO (Trepte and Hitchman (1992), see paragraph "Transport and development of a size distribution" of Section 1.2.1). The result of the processes described there would be an aerosol transport in this altitude towards the winter hemisphere which is stronger in the northern hemisphere and cuts of sharply between 15° and 30° in both hemispheres. Although the pattern seen in this Figure seems to be consistent with this explanation, further studies must be conducted to investigate other potential reasons for the observed seasonal cycle. The lifting and lowering of the tropopause height with the seasons surely has an impact. Furthermore, the seasonal variation of the scattering angle at a specific latitude (see Figure 4.4) has the potential to evoke such a signal artificially by influencing the sensitivity of the algorithm to various parameters (see Chapter 7). The volcanic eruptions dominating the pattern at the 70 hPa pressure level are not directly visible at the 20 hPa pressure level since

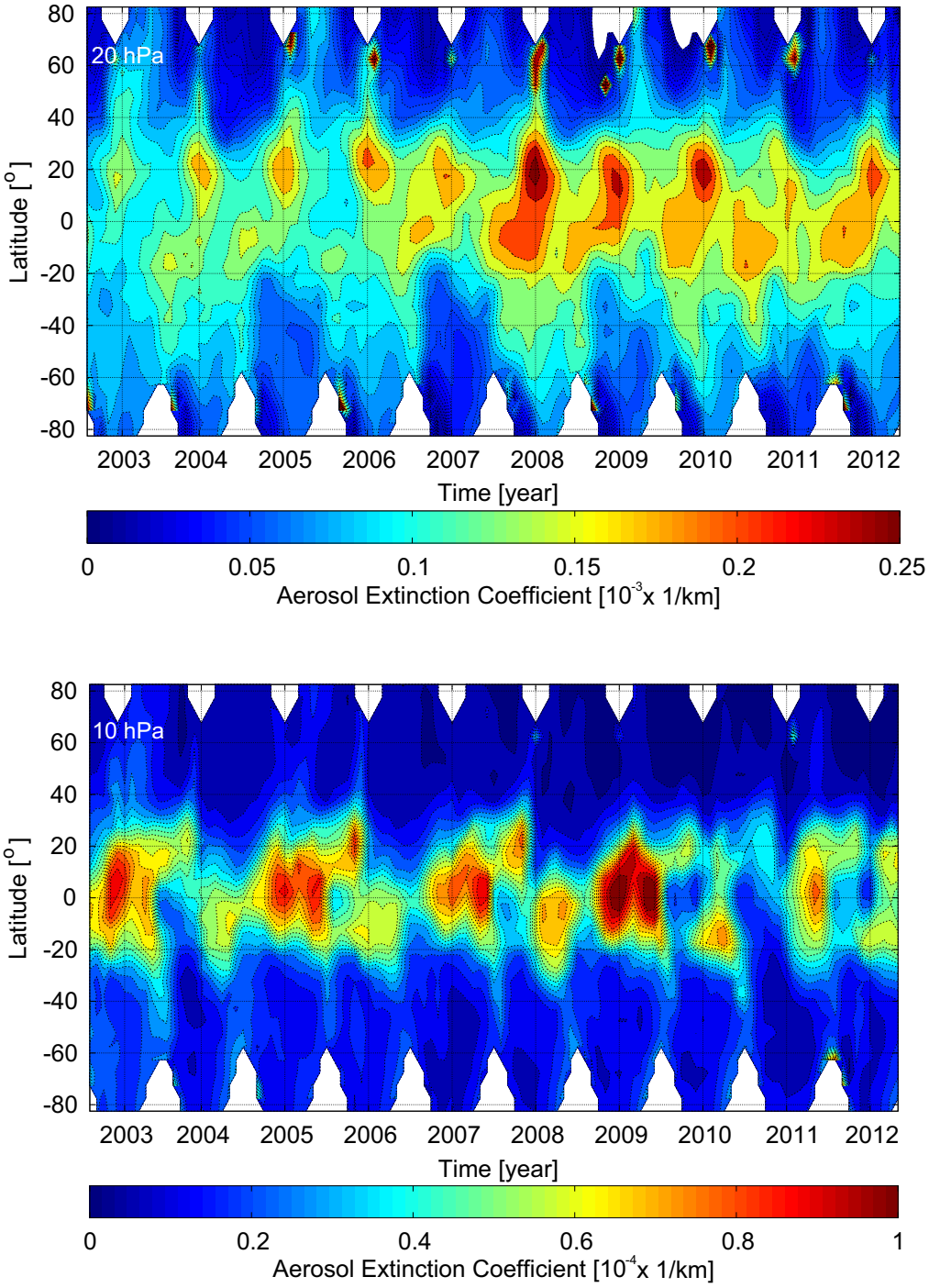

Figure 9.3: As Figure 9.1, but at 20 hPa (top panel, approximately 26 km altitude) and 10 hPa (bottom panel, approximately 32 km altitude) (figure prepared by Lena A. Brinkhoff, IUP Bremen).

none of them had a VEI high enough to reach this altitude region. However, the apparent increase in the stratospheric aerosol load between 2006 and 2007 might be caused by the two preceeding volcanic eruptions (Soufrière Hills and Tavurvur) in the tropics since tropical eruptions are assumed to have a significant impact on the global stratospheric aerosol load by injecting sulfur in the tropical reservoir. In the southern hemisphere around 40°S the aerosol extinction at 20 hPa also shows an apparent QBO signature.

The bottom panel of Figure 9.3 shows the 10 hPa pressure level, corresponding to approximately 32 km altitude. As to be expected, no PSC signatures are visible in this altitude region. The most prominent feature is a biennal signal in the tropics with a sharp edge at around 20° in both hemispheres. This finding is on first view consistent with the finding by Trepte and Hitchman (1992) that the aerosols in the tropical reservoir are lofted into and lowered out of this pressure level depending on the shear of the QBO (see Section 1.2.1). As for the two pressure levels below, the physical connections leading to this pattern have to be clarified in more detail by future studies.

Summarized, these pictures demonstrate that the aerosol retrieval is able to qualitatively capture the processes in the stratosphere and open up manifold possibilities for further investigations.

10 Summary and conclusion

In this work, an algorithm was presented for retrieving stratospheric aerosol extinction profiles between 12 and 35 km from SCIAMACHY limb-scatter observations. The retrieval algorithm followed Bourassa et al. (2007) who derived stratospheric aerosol extinction profiles from OSIRIS/Odin limb radiance spectra with a similar method. However, significant modifications were made to adapt the algorithm to the requirements of the specific observation geometry of the instrument SCIAMACHY. The algorithm was based on a color-index approach combining the limb radiance profiles at two wavelengths in the visible range, 470 and 750 nm. The stratospheric aerosols were assumed to consist of sulfate particles with a particle size distribution characteristic for background aerosol conditions. The retrieval was performed using a non-linear inverse method similar to the optimal estimation method described by Rodgers (2000), driving the sophisticated multiple scattering radiative transfer model and retrieval code SCIATRAN 3.1.

For the first retrieval version V1.0, as a common approximation a Henyey-Greenstein parameterized aerosol phase function was implemented. In a detailed investigation of the retrieval behaviour it was discovered that this approximation was not appropriate for SCIAMACHY geometries with high scattering angles in the southern hemisphere. The quality of the algorithm was significantly improved in version V1.1 by implementing a phase function calculated with a standard Mie code assuming a common particle size distribution for stratospheric background aerosols derived from mid-latitude in-situ measurements.

For both retrieval versions, sensitivity studies were carried out in order to investigate the impact of uncertainties in the knowledge of several atmospheric, surface, and geometrical parameters such as the ozone profile, neutral density profile, a priori aerosol extinction profile, ground albedo, tropospheric clouds, and tangent height registration. For both versions, the sensitivity of the retrieval to errors in all parameters was quite different on the two hemispheres of the Earth. For retrieval version V1.0, in the northern hemisphere the error in the aerosol extinction was below 10 % in all altitudes for realistic errors in the tested parameters. In contrast, in the southern hemisphere clouds can lead to errors in the aerosol extinction of up to 30 %, uncertainties in ground albedo and in neutral density up to 20 %. After implementing the Mie phase function in the retrieval version V1.1, the sensitivity of the statospheric aerosol extinction to the same errors as in version V1.0 approximately halved. The largest error (15 %) was produced by a 3 % uncertainty in the neutral density in 15 km altitude at 75°S. Errors in all other altitudes and latitudes were well below 10 %. Thus, the sensitivity of the retrieval could be reduced significantly in version V1.1.

Afterwards the SCIAMACHY stratospheric aerosol extinction profile retrievals were compared to all co-located SAGE II solar occultation measurements between January 2003 and the end of the SAGE II mission in August 2005. First, version 6.2 of the SAGE II aerosol extinction data set was used for the comparison as it constitutes a standard reference for the validation of stratospheric aerosol extinction data sets since 2003. The results of retrieval version V1.0 showed a good agreement with SAGE II V6.2 data in the global average, the difference was within 20 % above 15 km and even within 10 % between 16 and 30 km. However, the comparison in 20° latitude bins displayed the presence of systematic interhemispheric differences with values of in general around 20 % to up to 50 % with a different sign in the northern and southern hemisphere. While in the northern hemisphere our retrieval

algorithm V1.0 underestimated the aerosol extinction compared to SAGE II V6.2 by approximately 20 % on average, we found an overestimation of typically 30–40 % in the southern hemisphere, with a maximum of 60 % in 20 km altitude at southern mid-latitudes. Applying retrieval version V1.1 reduced the interhemispheric difference significantly. Between 15 and 33 km altitude, the previously large difference in the southern hemisphere was reduced to values of typically 0–15 % while a low bias remained in the northern hemisphere in comparison with SAGE II V6.2 measurements. Using version 7.0 of SAGE II aerosol extinction data published a few months before the completion of this thesis as a new validation data set further improved the quality of the retrieval. Reducing the already small difference in the southern hemisphere further to <10 % between 15 and 33 km and the difference in the northern hemisphere to <25 % at all altitudes led to a very good agreement of the global average within approximately 10 % above 15 km.

Finally, first results on the global morphology of stratospheric aerosols retrieved from SCIAMACHY with retrieval version V1.1 were presented. The morphologies from 2002–2012 at 70 hPa, 20 hPa, and 10 hPa pressure levels showed patterns that were consistent with the current knowledge of the dynamics in the stratosphere. Furthermore, the global aerosol extinction morphology at 70 hPa showed clear evidence for a stratospheric impact of multiple volcanic eruptions and a pyroconvective event between 2005 and 2011.

In summary, these results allow the conclusion that our retrieval is capable of providing stratospheric aerosol extinction profiles from SCIAMACHY limb radiances with a near-global coverage on a daily basis and with high vertical resolution. The SCIAMACHY stratospheric aerosol data set has the potential to greatly improve our understanding of spatial and temporal variability of stratospheric aerosols, and will be highly relevant for comparisons to model simulations.

Outlook

The work presented in this thesis showed that the knowledge of the phase function is critical for the quality of the retrieval. The implementation of a Mie phase function derived from a realistic particle size distribution improved the retrieval drastically, but could not account for the spatial, particularly vertical differences in particle size. Thus, understanding the aerosol microphsysical properties bears a large potential for the retrieval of stratospheric aerosol properties. In the color-index step in the retrieval algorithm, information on the aerosol particle size distribution contained in the limb radiance spectrum gets lost. Retrieving the aerosol extinction at multiple single wavelengths of the broadband spectrum of SCIAMACHY could provide the possibility to keep this information and enable a simultaneous retrieval of the Mie phase function which can then be used instead of a fixed phase function for all altitudes and latitudes.

A simultaneous cloud detection mechanism during the retrieval could reduce the error induced by tropospheric clouds as well as PSCs which are interpreted as stratospheric aerosols in the current retrieval version V1.1.

Retrieving the effective ground albedo directly from the SCIAMACHY data instead of using a static data base offers the opportunity to reduce the albedo-induced error in the retrieved aerosol extinction.

The discussion of the dynamical processes in the stratosphere started in Chapter 9 on the basis of morphologies at different pressure levels needs to be continued in more detail and fortified with model results, followed by a climatological interpretation. Vertical sections could provide the opportunity to investigate volcanic eruptions with focus on the vertical and horizontal propagation of the volcanic plume in the stratosphere.

Appendix

Abbreviations

a. u.	arbitrary units
DOM	Discrete Ordinate Method
DU	Dobson Unit
ECMWF	European Centre for Medium-Range Weather Forecasts
EM	electromagnetic
FOV	field of view
FWHM	full width at half maximum
HG	Henyey-Greenstein approximation
LOS	line-of-sight
LOS@TP	line-of-sight angle at the tangent point
MS	multiple scattering
NLC	Noctilucent Cloud
N/S	noise-to-signal value, the inverse of S/N
PSC	Polar Stratospheric Cloud
PSD	particle size distribution
QBO	quasi-biennial oscillation
SAA	solar azimuth angle
SAA@TP	solar azimuth angle at the tangent point
S/N	signal-to-noise ratio

SS	single scattering
SSA	single scattering angle
SWIR	short-wavelength infrared
SZA	solar zenith angle
SZA@TP	solar zenith angle at the tangent point
TCFoV	Total Clear Field of View
TP	tangent point
UV	ultraviolet
V1.0	SCIAMACHY retrieval version 1.0 (HG phase function)
V1.1	SCIAMACHY retrieval version 1.1 (Mie phase function)
VEI	Volcanic Explosivity Index

List of Figures

List of Tables

Bibliography

Ackerman, M., Lippens, C., and Muller, C.: Stratospheric aerosols properties from Earth limb photography, *Nature*, 292(5824), 587–591, doi:10.1038/292587a0, 1981.

Aitken, J.: The remarkable sunsets, *Proceedings of the Royal Society of Edinburgh*, 12, 448–450/647–660, 1884.

Arnold, F., Stilp, T., Busen, R., and Schumann, U.: Jet Engine Exhaust Chemiion Measurements: Implications for Gaseous SO_3 and H_2SO_4, *Atmos. Environ.*, 32, 3073–3077, 1998.

Bertaux, J. L., Mégie, G., Widemann, T., Chassefière, E., Pellinen, R., Kyrölä, E., Korpela, S., and Simon, P.: Monitoring of ozone trend by stellar occultations: the GOMOS instrument, *Adv. Space Res.*, 11(3), 237–242, doi: 10.1016/0273-1177(91)90426-K, 1991.

Bishop, S. E.: Letters to the Editor: The remarkable sunsets, *Nature*, 29, 259–260, doi:10.1038/029259b0, 1884.

Bohren, C. F. and Huffman, D. R.: Absorption and Scattering of Light by Small Particles, John Wiley & Sons, New York, 1983.

Bourassa, A. E., Degenstein, D. A., Gattinger, R. L., and Llewellyn, E. J.: Stratospheric aerosol retrieval with optical spectrograph and infrared imaging system limb scatter measurements, *J. Geophys. Res.*, 112(D10), 1–15, doi:10.1029/2006JD008079, 2007.

Bourassa, A. E., Degenstein, D. A., and Llewellyn, E. J.: Retrieval of stratospheric aerosol size information from OSIRIS limb scattered sunlight spectra, *Atmos. Chem. Phys.*, 8(21), 6375–6380, doi:10.5194/acp-8-6375-2008, 2008.

Bourassa, A. E., Degenstein, D. A., Elash, B. J., and Llewellyn, E. J.: Evolution of the stratospheric aerosol enhancement following the eruptions of Okmok and Kasatochi: Odin-OSIRIS measurements, *J. Geophys. Res.*, 115, D00L03, doi: 10.1029/2009JD013274, 2010.

Bourassa, A. E., Robock, A., Randel, W. J., Deshler, T., Rieger, L. A., Lloyd, N. D., Llewellyn, E. J., and Degenstein, D. A.: Large volcanic aerosol load in the stratosphere linked to Asian monsoon transport, *Science*, 337(6090), 78–81, doi:10.1126/science.1219371, 2012.

Bovensmann, H., Burrows, J. P., Buchwitz, M., Frerick, J., Noël, S., Rozanov, V. V., Chance, K. V., and Goede, A. P. H.: SCIAMACHY: Mission Objectives and Measurement Modes, *J. Atmos. Sci.*, 56(2), 127–150, doi:10.1175/1520-0469(1999)056<0127:SMOAMM>2.0.CO;2, 1999.

Brock, C. A., Hamill, P., Wilson, J. C., Jonsson, H. H., and Chan, K. R.: Particle Formation in the Upper Tropical Troposphere: A Source of Nuclei for the Stratospheric Aerosol, *Science*, 270(5242), 1650–1653, doi:10.1126/science.270.5242.1650, 1995.

Brogniez, C. and Lenoble, J.: Size distribution of stratospheric aerosol from SAGE II multiwavelength extinction, in Hobbs, V. and McCormick, A., eds., *Aerosol and Climate*, pp. 305–311, A. Deepak Pub., Hampton, Va., USA, 1988.

Brogniez, C., Santer, R., Diallo, B. S., Herman, M., Lenoble, J., and Jäger, H.: Comparative observations of stratospheric aerosols by ground-based lidar, balloon-borne polarimeter, and satellite solar occultation, *J. Geophys. Res.*, 97(D18), 20805–20823, doi:10.1029/92JD01919, 1992.

Burrows, J. P., Hölzle, E., Goede, A. P. H., Visser, H., and Fricke, W.: SCIAMACHY – scanning imaging absorption spectrometer for atmospheric chartography, *Acta Astronaut.*, 35(7), 445–451, doi:10.1016/0094-5765(94)00278-T, 1995.

Carslaw, K. S. and Kärcher, B.: Stratospheric Aerosol Processes, in Thomason, L. and Peter, T., eds., *SPARC assessment of stratospheric aerosol properties, WCRP-124, WMO/TD-No. 1295, SPARC Report No. 4*, chapter 1, 2006.

Chagnon, C. W. and Junge, C. E.: The vertical distribution of sub-micron particles in the stratosphere, *J. Meteor.*, 18(6), 746–752, doi:10.1175/1520-0469(1961)018<0746:TVDOSM>2.0.CO;2, 1961.

Charlson, R. J., Schwartz, S. E., Hales, J. M., Cess, R. D., Coakley, J. A., Hansen, J. E., and Hofmann, D. J.: Climate forcing by anthropogenic aerosols, *Science*, 255(5043), 423–430, doi:10.1126/science.255.5043.423, 1992.

Chatfield, R. B. and Crutzen, P. J.: Sulfur dioxide in remote oceanic air: Cloud transport of reactive precursors, *J. Geophys. Res.*, 89(D5), 7111–7132, doi:10.1029/JD089iD05p07111, 1984.

Chu, W. P., McCormick, M. P., Lenoble, J., Brogniez, C., and Pruvost, P.: SAGE II inversion algorithm, *J. Geophys. Res.*, 94(D6), 8339–8351, doi:10.1029/JD094iD06p08339, 1989.

Crutzen, P. J.: The influence of nitrogen oxides on the atmospheric ozone content, *Quart. J. Roy. Meteor. Soc.*, 96(408), 320–325, doi:10.1002/qj.49709640815, 1970.

Crutzen, P. J.: The possible importance of CSO for the sulfate layer of the stratosphere, *Geophys. Res. Lett.*, 3(2), 73–76, doi:10.1029/GL003i002p00073, 1976.

Crutzen, P. J.: Albedo enhancement by stratospheric sulfur injections: A contribution to resolve a policy dilemma?, *Clim. Change*, 77, 211–219, doi:10.1007/s10584-006-9101-y, 2006.

Cunnold, D. M., Gray, C. R., and Merritt, D. C.: Stratospheric aerosol layer detection, *J. Geophys. Res.*, 78(6), 920–931, doi:10.1029/JC078i006p00920, 1973.

Cziczo, D. J., Thomson, D. S., and Murphy, D. M.: Ablation, flux, and atmospheric implications of meteors inferred from stratospheric aerosol, *Science*, 291(5509), 1772–1775, doi:10.1126/science.1057737, 2001.

Damadeo, R. P., Zawodny, J. M., Thomason, L. W., and Iyer, N.: SAGE version 7.0 algorithm: application to SAGE II, *Atmos. Meas. Tech. Discuss.*, 6(3), 5101–5171, doi:10.5194/amtd-6-5101-2013, 2013.

Davies, C. N.: Size distribution of atmospheric particles, *J. Aerosol Sci.*, 5, 293–300, 1974.

Deshler, T.: Thirty years of in situ stratospheric aerosol size distribution measurements from Laramie, Wyoming (41°N), using balloon-borne instruments, *J. Geophys. Res.*, 108(D5), 1–13, doi:10.1029/2002JD002514, 2003.

Deshler, T.: A review of global stratospheric aerosol: Measurements, importance, life cycle, and local stratospheric aerosol, *Atmos. Res.*, 90(2-4), 223–232, doi:10.1016/j.atmosres.2008.03.016, 2008.

Deshler, T., Hofmann, D. J., Johnson, B. J., and Rozier, W. R.: Balloonborne measurements of the Pinatubo aerosol size distribution and volatility at Laramie, Wyoming during the summer of 1991, *Geophys. Res. Lett.*, 19(2), 199–202, doi:10.1029/91GL02787, 1992.

Deshler, T., Anderson-Sprecher, R., Jäger, H., Barnes, J., Hofmann, D. J., Clemesha, B., Simonich, D., Osborn, M., Grainger, R. G., and Godin-Beekmann, S.: Trends in

the nonvolcanic component of stratospheric aerosol over the period 1971-2004, *J. Geophys. Res.*, 111(D1), D01201, doi:10.1029/2005JD006089, 2006.

Dutton, E. G. and Christy, J. R.: Solar radiative forcing at selected locations and evidence for global lower tropospheric cooling following the eruptions of El Chichón and Pinatubo, *Geophys. Res. Lett.*, 19(23), 2313–2310, doi:10.1029/92GL02495, 1992.

Eckhardt, S., Stohl, A., Wernli, H., James, P., Forster, C., and Spichtinger, N.: A 15-Year Climatology of Warm Conveyor Belts, *J. Climate*, 17(1), 218–237, doi:10.1175/1520-0442(2004)017<0218:AYCOWC>2.0.CO;2, 2004.

Eichmann, K.-U., von Savigny, C., Reichl, P., Robert, C., Steinwagner, J., Bovensmann, H., and Burrows, J. P.: SCODA: SCIAMACHY ClOud Detection Algorithm from limb radiance measurements, Algorithm Theoretical Baseline Document (ATBD), University of Bremen, Bremen, Germany, 2009.

Erle, F., Grendel, A., Perner, D., Platt, U., and Pfeilsticker, K.: Evidence of heterogeneous bromine chemistry on cold stratospheric sulphate aerosols, *Geophys. Res. Lett.*, 25(23), 4329–4332, doi:10.1029/1998GL900087, 1998.

Fahey, D. W., Kawa, S. R., Woodbridge, E. L., Tin, P., Wilson, J. C., Jonsson, H. H., Dye, J. E., Baumgardner, D., Borrmann, S., Toohey, D. W., Avallone, L. M., Proffitt, M. H., Margitan, J., Loewenstein, M., Podolske, J. R., Salawitch, R. J., Wofsy, S. C., Ko, M. K. W., Anderson, D. E., Schoeber, M. R., and Chan, K. R.: In situ measurements constraining the role of sulphate aerosols in mid-latitude ozone depletion, *Nature*, 363(6429), 509–514, doi:10.1038/363509a0, 1993.

Ferrare, R. A., Melfi, S. H., Whiteman, D. N., Evans, K. D., and Leifer, R.: Raman lidar measurements of aerosol extinction and backscattering: 1. Methods and comparisons, *J. Geophys. Res.*, 103(D16), 19663–19689, doi:10.1029/98JD01646, 1998.

Flittner, D. E., Bhartia, P. K., and Herman, B. M.: O_3 profiles retrieved from limb scatter measurements: Theory, *Geophys. Res. Lett.*, 27(17), 2601–2604, doi:10.1029/1999GL011343, 2000.

Fromm, M., Alfred, J., Hoppel, K., Hornstein, J., Bevilacqua, R., Shettle, E., Servranckx, R., Li, Z., and Stocks, B.: Observations of boreal forest fire smoke in the stratosphere by POAM III, SAGE II, and lidar in 1998, *Geophys. Res. Lett.*, 27(9), 1407–1410, doi:10.1029/1999GL011200, 2000.

Fussen, D.: A volcanism dependent model for the extinction profile of stratospheric aerosols in the UV-visible range, *Geophys. Res. Lett.*, 26(6), 703–706, 1999.

Glaccum, W., Lucke, R. L., Bevilacqua, R. M., Shettle, E. P., Hornstein, J. S., Chen, D. T., Lumpe, J. D., Krigman, S. S., Debrestian, D. J., Fromm, M. D., Dalaudier, F., Chassefière, E., Deniel, C., Randall, C. E., Rusch, D. W., Olivero, J. J., Brogniez, C., Lenoble, J., and Kremer, R.: The Polar Ozone and Aerosol Measurement instrument, *J. Geophys. Res.*, 101(D9), 14479–14487, doi:10.1029/96JD00576, 1996.

Goodman, J., Snetsinger, K. G., Ferry, G. V., Farlow, N. H., Lem, H. Y., and Hayes, D. M.: Altitude variations in stratospheric aerosols of a tropical region, *Geophys. Res. Lett.*, 9(6), 609–612, doi:10.1029/GL009i006p00609, 1982.

Gottwald, M. and Bovensmann, H.: SCIAMACHY - Exploring the Changing Earth's Atmosphere, Springer, Dordrecht Heidelberg London New York, 2011.

Gruner, P. and Kleinert, H.: Die Dämmerungserscheinungen, *Probleme der Kosmischen Physik 10*, pp. 1–113, 1927.

Hamill, P., Jensen, E. J., Russell, P. B., and Bauman, J. J.: The Life Cycle of Stratospheric Aerosol Particles, *Bull. Amer. Meteor. Soc.*, 78(7), 1395–1410, doi:10.1175/1520-0477(1997)078<1395:TLCOSA>2.0.CO;2, 1997.

Hamill, P., Brogniez, C., Thomason, L. W., and Deshler, T.: Instrument Descriptions, in Thomason, L. and Peter, T., eds., *SPARC assessment of stratospheric aerosol properties, WCRP-124, WMO/TD-No. 1295, SPARC Report No. 4*, chapter 3, 2006.

Hansen, J. E. and Travis, L. D.: Light scattering in planetary atmospheres, *Space Sci. Rev.*, 16(1957), 527–610, 1974.

Hansen, J. E., Lacis, A., Ruedy, R., and Sato, M.: Potential climate impact of Mount Pinatubo eruption, *Geophys. Res. Lett.*, 19(2), 215–218, doi:10.1029/91GL02788, 1992.

Hanson, D. R. and Ravishankara, A. R.: Heterogeneous chemistry of bromine species in sulfuric acid under stratospheric conditions, *Geophys. Res. Lett.*, 22(4), 385–388, doi:10.1029/94GL03379, 1995.

Henyey, L. C. and Greenstein, J. L.: Diffuse radiation in the Galaxy, *Astrophys. J.*, 93, 70–83, doi:10.1086/144246, 1941.

Hess, M., Koepke, P., and Schult, I.: Optical Properties of Aerosols and Clouds: The Software Package OPAC, *Bull. Amer. Meteor. Soc.*, 79(5), 831–844, doi:10.1175/1520-0477(1998)079<0831:OPOAAC>2.0.CO;2, 1998.

Hofmann, D. J. and Rosen, J. M.: Measurement of the sulfuric acid weight percent in the stratospheric aerosol from the El Chichón eruption, *Geofisica Internacional*, 23, 309–320, 1984.

Hofmann, D. J., Rosen, J. M., Pepin, T. J., and Pinnick, R. G.: Stratospheric Aerosol Measurements I: Time Variations at Northern Midlatitudes, *J. Atmos. Sci.*, 32(7), 1446–1456, doi:10.1175/1520-0469(1975)032<1446:SAMITV>2.0.CO;2, 1975.

Hofmann, D. J., Barnes, J., O'Neill, M., Trudeau, M., and Neely, R.: Increase in background stratospheric aerosol observed with lidar at Mauna Loa Observatory and Boulder, Colorado, *Geophys. Res. Lett.*, 36, L15808, doi:10.1029/2009GL039008, 2009.

Holton, J. R., Haynes, P. H., McIntyre, M. E., Douglass, A. R., Rood, R. B., and Pfister, L.: Stratosphere-troposphere exchange, *Rev. Geophys.*, 33(4), 403–439, doi:10.1029/95RG02097, 1995.

Hoogen, R.: Mie theory outline & IUPMIE user's guide, Technical report, Institut für Umweltphysik, Universität Bremen, Bremen, Germany, 1995.

Hoogen, R., Rozanov, V. V., and Burrows, J. P.: Ozone profiles from GOME satellite data: Algorithm description and first validation, *J. Geophys. Res.*, 104(D7), 8263–8280, doi:10.1029/1998JD100093, 1999.

Hunten, D. M., Turco, R. P., and Toon, O. B.: Smoke and Dust Particles of Meteoric Origin in the Mesosphere and Stratosphere, *J. Atmos. Sci.*, 37(6), 1342–1357, doi:10.1175/1520-0469(1980)037<1342:SADPOM>2.0.CO;2, 1980.

IPCC: Climate Change 2007: The Physical Science Basis. Contribution of Working Group I to the Fourth Assessment Report of the Intergovernmental Panel on Climate Change (Solomon, S., Qin, D., Manning, M., Chen, Z., Marquis, M., Averyt, K. B., Tignor, M. and Miller, H. L., eds.), Cambridge Univ. Press, Cambridge, UK, and New York, NY, USA, 2007.

Johnston, P. V., McKenzie, R. L., Keys, J. G., and Matthews, W. A.: Observations of depleted stratospheric NO_2 following the Pinatubo volcanic eruption, *Geophys. Res. Lett.*, 19(2), 211–213, doi:10.1029/92GL00043, 1992.

Jonsson, H. H., Wilson, J. C., Brock, C. A., Knollenberg, R. G., Newton, T. R., Dye, J. E., Baumgardner, D., Borrmann, S., Ferry, G. V., Pueschel, R., Woods, D. C., and Pitts, M. C.: Performance of a Focused Cavity Aerosol Spectrometer for Measurements in the Stratosphere of Particle Size in the 0.06–2.0-μm-Diameter Range, *J. Atmos. Oceanic Technol.*, 12(1), 115–129, doi:10.1175/1520-0426(1995)012<0115:POAFCA>2.0.CO;2, 1995.

Junge, C. E. and Manson, J. E.: Stratospheric aerosol studies, *J. Geophys. Res.*, 66(7), 2163–2182, doi:10.1029/JZ066i007p02163, 1961.

Junge, C. E., Chagnon, C. W., and Manson, J. E.: Stratospheric Aerosols, *J. Meteor.*, 18(1), 81–108, doi:10.1175/1520-0469(1961)018<0081:SA>2.0.CO;2, 1961.

Kärcher, B.: Aviation-produced aerosols and contrails, *Surv. Geophys.*, 20, 113–167, 1999.

Kauss, J.: Aerosol-Parametrisierung für Strahlungstransport-Simulationen im ultravioletten bis nahinfraroten Spektralbereich, Diploma thesis, University of Bremen, Bremen, Germany, 1998.

Kettle, A. J., Kuhn, U., von Hobe, M., Kesselmeier, J., and Andreae, M. O.: Global budget of atmospheric carbonyl sulfide: Temporal and spatial variations of the dominant sources and sinks, *J. Geophys. Res.*, 107(D22), ACH25 1–16, doi: 10.1029/2002JD002187, 2002.

Khalil, M. A. K. and Rasmussen, R. A.: Global sources, lifetimes and mass balances of carbonyl sulfide (OCS) and carbon disulfide (CS_2) in the earth's atmosphere, *Atmos. Environ.*, 18(9), 1805–1813, doi:10.1016/0004-6981(84)90356-1, 1984.

Kjellstrom, E., Feichter, J., Sausen, R., and Hein, R.: The contribution of aircraft emissions to the atmospheric sulfur budget, *Atmos. Environ.*, 33, 3455–3465, doi:10.1016/S1352-2310(98)00368-9, 1999.

Klenk, K. F., Bhartia, P. K., Kaveeshwar, V. G., McPeters, R. D., Smith, P. M., and Fleig, A. J.: Total Ozone Determination from the Backscattered Ultraviolet (BUV) Experiment, *J. Climate Appl. Meteor.*, 21, 1672–1684, doi:10.1175/1520-0450(1982)021<1672:TODFTB>2.0.CO;2, 1982.

Kravitz, B., Robock, A., and Bourassa, A. E.: Negligible climatic effects from the 2008 Okmok and Kasatochi volcanic eruptions, *J. Geophys. Res.*, 115, 1–16, doi: 10.1029/2009JD013525, 2010.

Kyrölä, E., Tamminen, J., Leppelmeier, G. W., Sofieva, V., Hassinen, S., Bertaux, J. L., Hauchecorne, A., Dalaudier, F., Cot, C., Korablev, O., Fanton d'Andon, O., Barrot, G., Mangin, A., Théodore, B., Guirlet, M., Etanchaud, F., Snoeij, P., Koopman, R., Saavedra, L., Fraisse, R., Fussen, D., and Vanhellemont, F.: GOMOS on Envisat: an overview, *Adv. Space Res.*, 33(7), 1020–1028, doi:10.1016/S0273-1177(03)00590-8, 2004.

Labitzke, K. and McCormick, M. P.: Stratospheric temperature increases due to Pinatubo aerosols, *Geophys. Res. Lett.*, 19(2), 207–210, doi:10.1029/91GL02940, 1992.

Lacis, A., Hansen, J. E., and Sato, M.: Climate forcing by stratospheric aerosols, *Geophys. Res. Lett.*, 19(15), 1607–1610, doi:10.1029/92GL01620, 1992.

Le Treut, H., Forichon, M., Boucher, O., and Li, Z.-X.: Sulfate Aerosol Indirect Effect and CO_2 Greenhouse Forcing: EquilibriumResponse of the LMD GCM and Associated Cloud Feedbacks, *J. Climate*, 11(7), 1673–1684, doi:10.1175/1520-0442(1998)011<1673:SAIEAC>2.0.CO;2, 1998.

Lee, T. F., Nelson, C. S., Dills, P., Riishojgaard, L. P., Jones, A., Li, L., Miller, S., Flynn, L. E., Jedlovec, G., McCarty, W., Hoffman, C., and McWilliams, G.: NPOESS: Next-Generation Operational Global Earth Observations, *Bull. Amer. Meteor. Soc.*, 91(6), 727–740, doi:10.1175/2009BAMS2953.1, 2010.

Lenoble, J., Pruvost, P., and Brogniez, C.: SAGE satellite observations of stratospheric aerosols from Mount St. Helens eruption: A two-wavelength analysis, *J. Geophys. Res.*, 89(D7), 11666–11676, doi:10.1029/JD089iD07p11666, 1984.

Llewellyn, E. J., Lloyd, N. D., Degenstein, D. A., Gattinger, R. L., Petelina, S. V., Bourassa, A. E., Wiensz, J. T., Ivanov, E. V., McDade, I. C., Solheim, B. H., McConnell, J. C., Haley, C. S., von Savigny, C., Sioris, C. E., McLinden, C. A., Griffioen, E., Kaminski, J., Evans, W. F. J., Puckrin, E., Strong, K., Wehrle, V., Hum, R. H., Kendall, D. J. W., Matsushita, J., Murtagh, D. P., Brohede, S., Stegman, J., Witt, G., Barnes, G., Payne, W. F., Piché, L., Smith, K., Warshaw, G., Deslauniers, D. L., Marchand, P., Richardson, E. H., King, R. A., Wevers, I., McCreath, W., Kyrölä, E., Oikarinen, L., Leppelmeier, G. W., Auvinen, H., Mégie, G., Hauchecorne, A., Lefèvre, F., de La Nöe, J., Ricaud, P., Frisk, U., Sjoberg, F., von Schéele, F., and Nordh, L.: The OSIRIS instrument on the Odin spacecraft, *Can. J. Phys.*, 82(6), 411–422, doi:10.1139/p04-005, 2004.

Lucke, R. L., Korwan, D. R., Bevilacqua, R. M., Hornstein, J. S., Shettle, E. P., Chen, D. T., Daehler, M., Lumpe, J. D., Fromm, M. D., Debrestian, D., Neff, B., Squire, M., König-Langlo, G., and Davies, J.: The Polar Ozone and Aerosol Measurement (POAM) III instrument and early validation results, *J. Geophys. Res.*, 104(D15), 18785–18799, doi:10.1029/1999JD900235, 1999.

Lumpe, J. D.: POAM III retrieval algorithm and error analysis, *J. Geophys. Res.*, 107(D21), ACH5 1–31, doi:10.1029/2002JD002137, 2002.

Matthews, E.: Global Vegetation and Land Use: New High-Resolution Data Bases for Climate Studies, *J. Climate Appl. Meteor.*, 22(3), 474–487, doi:10.1175/1520-0450(1983)022<0474:GVALUN>2.0.CO;2, 1983.

McCormick, M. P., Hamill, P., Chu, W. P., Swissler, T. J., McMaster, L. R., and Pepin, T. J.: Satellite Studies of the Stratospheric Aerosol, *Bull. Amer. Meteor. Soc.*, 60(9), 1038–1046, doi:10.1175/1520-0477(1979)060<1038:SSOTSA>2.0.CO;2, 1979.

McCormick, M. P., Thomason, L. W., and Trepte, C. R.: Atmospheric effects of the Mt Pinatubo eruption, *Nature*, 373(6513), 399–404, doi:10.1038/373399a0, 1995.

McElroy, C. T., Nowlan, C. R., Drummond, J. R., Bernath, P. F., Barton, D. V., Dufour, D. G., Midwinter, C., Hall, R. B., Ogyu, A., Ullberg, A., Wardle, D. I., Kar, J., Zou, J., Nichitiu, F., Boone, C. D., Walker, K. A., and Rowlands, N.: The ACE-MAESTRO instrument on SCISAT: description, performance, and preliminary results, *Appl. Opt.*, 46(20), 4341–4356, doi:10.1364/AO.46.004341, 2007.

McLinden, C. A., McConnell, J. C., McElroy, C. T., and Griffioen, E.: Observations of Stratospheric Aerosol Using CPFM Polarized Limb Radiances, *J. Atmos. Sci.*, 56(2), 233–240, doi:10.1175/1520-0469(1999)056<0233:OOSAUC>2.0.CO;2, 1999.

Mie, G.: Beiträge zur Optik trüber Medien, speziell kolloidaler Metallösungen, *Ann. Phys.*, 330(3), 377–445, doi:10.1002/andp.19083300302, 1908.

Minnis, P., Harrison, E. F., Stowe, L. L., Gibson, G. G., Denn, F. M., Doelling, D. R., and Smith, W. L.: Radiative climate forcing by the mount pinatubo eruption, *Science*, 259(5100), 1411–1415, doi:10.1126/science.259.5100.1411, 1993.

Mozurkewich, M. and Calvert, J. G.: Reaction probability of N_2O_5 on aqueous aerosols, *J. Geophys. Res.*, 93(D12), 15889–15896, doi:10.1029/JD093iD12p15889, 1988.

Murphy, D. M.: In Situ Measurements of Organics, Meteoritic Material, Mercury, and Other Elements in Aerosols at 5 to 19 Kilometers, *Science*, 282(5394), 1664–1669, doi:10.1126/science.282.5394.1664, 1998.

Murtagh, D., Frisk, U., Merino, F., Ridal, M., Jonsson, A., Stegman, J., Witt, G., Eriksson, P., Jiménez, C., Megie, G., de la Noë, J., Ricaud, P., Baron, P., Pardo, J. R., Hauchcorne, A., Llewellyn, E. J., Degenstein, D. A., Gattinger, R. L., Lloyd, N. D., Evans, W. F., McDade, I. C., Haley, C. S., Sioris, C., von Savigny, C., Solheim, B. H., McConnell, J. C., Strong, K., Richardson, E. H., Leppelmeier, G. W., Kyrölä, E., Auvinen, H., and Oikarinen, L.: An overview of the Odin atmospheric mission, *Can. J. Phys.*, 80(4), 309–319, doi:10.1139/p01-157, 2002.

Newhall, C. G. and Self, S.: The volcanic explosivity index (VEI) an estimate of explosive magnitude for historical volcanism, *J. Geophys. Res.*, 87(C2), 1231–1238, doi:10.1029/JC087iC02p01231, 1982.

Noël, S., Bovensmann, H., Wuttke, M. W., Burrows, J. P., Gottwald, M., Krieg, E., Goede, A. P. H., and Muller, C.: Nadir, limb, and occultation measurements with SCIAMACHY, *Adv. Space Res.*, 29(11), 1819–1824, doi:10.1016/S0273-1177(02)00102-3, 2002.

Notholt, J. and Bingemer, H.: Precursor gas measurements, in Thomason, L. and Peter, T., eds., *SPARC assessment of stratospheric aerosol properties, WCRP-124, WMO/TD-No. 1295, SPARC Report No. 4*, chapter 2, 2006.

Ovigneur, B., Landgraf, J., Snel, R., and Aben, I.: Retrieval of stratospheric aerosol density profiles from SCIAMACHY limb radiance measurements in the O_2 A-band, *Atmos. Meas. Tech. Discuss.*, 4, 2359–2373, doi:10.5194/amtd-4-1795-2011, 2011.

Pepin, T. J., McCormick, M. P., Chu, W. P., Simon, F., Swissler, T. J., Adams, R. R., Crumbly, K. R., and Fuller Jr., W. H.: Stratospheric aerosol measurements, *NASA Spec. Publ.*, SP-421, 127–136, 1977.

Plumb, R. A.: A "tropical pipe" model of stratospheric transport, *J. Geophys. Res.*, 101(D2), 3957–3972, doi:10.1029/95JD03002, 1996.

Prather, M.: Catastrophic loss of stratospheric ozone in dense volcanic clouds, *J. Geophys. Res.*, 97(D9), 10187–10191, doi:10.1029/92JD00845, 1992.

Randel, W. J., Wu, F., and Gaffen, D. J.: Interannual variability of the tropical tropopause derived from radiosonde data and NCEP reanalyses, *J. Geophys. Res.*, 105(D12), 15509–15523, doi:10.1029/2000JD900155, 2000.

Robock, A.: The Mount St. Helens volcanic eruption of 18 may 1980: Minimal Climatic Effect, *Science*, 212(4501), 1383–1384, doi:10.1126/science.212.4501.1383, 1981.

Rodgers, C. D.: Inverse Methods for Atmospheric Sounding: Theory and Practice, World Scientific, Singapore, 2000.

Rosen, J. M.: The Boiling Point of Stratospheric Aerosols, *J. Appl. Meteor.*, 10(5), 1044–1046, doi:10.1175/1520-0450(1971)010<1044:TBPOSA>2.0.CO;2, 1971.

Rozanov, V. V. and Kokhanovsky, A. A.: Impact of single- and multi-layered cloudiness on ozone vertical column retrievals using nadir observations of backscattered solar radiation, in Kokhanovsky, A. A., ed., *Light Scattering Reviews 3*, pp. 133–189, Springer, Berlin, 2008.

Rozanov, V. V., Diebel, D., Spurr, R. J. D., and Burrows, J. P.: GOMETRAN: A radiative transfer model for the satellite project GOME, the plane-parallel version, *J. Geophys. Res.*, 102, 16683–16695, doi:10.1029/96JD01535, 1997.

Rozanov, V. V., Rozanov, A. V., Kokhanovsky, A. A., and Burrows, J. P.: Radiative transfer through terrestrial atmosphere and ocean: software package SCIATRAN, *submitted to J. Quant. Spectrosc. Radiat. Transfer*, 2013.

Russell, J. M., Gordley, L. L., Park, J. H., Drayson, S. R., Hesketh, W. D., Cicerone, R. J., Tuck, A. F., Frederick, J. E., Harries, J. E., and Crutzen, P. J.: The Halogen Occultation Experiment, *J. Geophys. Res.*, 98(D6), 10777–10797, doi:10.1029/93JD00799, 1993.

Russell, P. B. and McCormick, M. P.: SAGE II aerosol data validation and initial data use: An introduction and overview, *J. Geophys. Res.*, 94(D6), 8335–8338, doi:10.1029/JD094iD06p08335, 1989.

Sato, M., Hansen, J. E., McCormick, M. P., and Pollack, J. B.: Stratospheric aerosol optical depths, 1850–1990, *J. Geophys. Res.*, 98(D12), 22987–22994, doi:10.1029/93JD02553, 1993.

Self, S., Zhao, J.-X., Holasek, R. E., Torres, R. C., and King, A. J.: The Atmospheric Impact of the 1991 Mount Pinatubo Eruption, in Newhall, C. G. and Punongbayan, R. S., eds., *Fire and Mud: Eruptions and Lahars of Mount Pinatubo, Philippines*, University of Washington Press, Washington, 1997.

Sheridan, P. J., Schnell, R. C., Hofmann, D. J., and Deshler, T.: Electron microscope studies of Mt. Pinatubo aerosol layers over Laramie, Wyoming during summer 1991, *Geophys. Res. Lett.*, 19(2), 203–206, doi:10.1029/91GL02789, 1992.

Siddaway, J. M. and Petelina, S. V.: Transport and evolution of the 2009 Australian Black Saturday bushfire smoke in the lower stratosphere observed by OSIRIS on Odin, *J. Geophys. Res.*, 116(D6), 1–9, doi:10.1029/2010JD015162, 2011.

Solomon, S.: Stratospheric ozone depletion: A review of concepts and history, *Rev. Geophys.*, 37(3), 275–316, doi:10.1029/1999RG900008, 1999.

Solomon, S., Sanders, R. W., Garcia, R. R., and Keys, J. G.: Increased chlorine dioxide over Antarctica caused by volcanic aerosols from Mount Pinatubo, *Nature*, 363(6426), 245–248, doi:10.1038/363245a0, 1993.

Solomon, S., Portmann, R. W., Garcia, R. R., Thomason, L. W., Poole, L. R., and McCormick, M. P.: The role of aerosol variations in anthropogenic ozone depletion at northern midlatitudes, *J. Geophys. Res.*, 101(D3), 6713–6727, doi:10.1029/95JD03353, 1996.

Solomon, S., Daniel, J. S., Neely, R. R., Vernier, J.-P., Dutton, E. G., and Thomason, L. W.: The persistently variable "background" stratospheric aerosol layer and global

climate change, *Science*, 333(6044), 866–870, doi:10.1126/science.1206027, 2011.

Sonkaew, T., Rozanov, V. V., von Savigny, C., Rozanov, A., Bovensmann, H., , and Burrows, J. P.: Cloud sensitivity studies for stratospheric and lower mesospheric ozone profile retrievals from measurements of limb-scattered solar radiation, *Atmos. Meas. Tech.*, 2, 653–678, doi:10.5194/amt-2-653-2009, 2009.

Stamnes, K., Tsay, S.-C., Wiscombe, W., and Jayaweera, K.: Numerically stable algorithm for discrete-ordinate-method radiative transfer in multiple scattering and emitting layered media, *Appl. Opt.*, 27(12), 2502–2509, doi:10.1364/AO.27.002502, 1988.

Stothers, R. B.: Major optical depth perturbations to the stratosphere from volcanic eruptions: Pyrheliometric period, 1881–1960, *J. Geophys. Res.*, 101(D2), 3901–3920, doi:10.1029/95JD03237, 1996.

Stowe, L. L., Carey, R. M., and Pellegrino, P. P.: Monitoring the Mt. Pinatubo aerosol layer with NOAA/11 AVHRR data, *Geophys. Res. Lett.*, 19(2), 159–162, doi:10.1029/91GL02958, 1992.

Symons, G. J., Judd, J. W., Strachey, R., Wharton, W. J. L., Evans, F. J., Russell, F. A. R., Archibald, D., and Whipple, G. M.: The Eruption of Krakatoa and Subsequent Phenomena, Report of the Krakatoa Committee of the Royal Society, Trübner & Company, 1888.

Taha, G., Jaross, G., Fussen, D., Vanhellemont, F., Kyrölä, E., and McPeters, R. D.: Ozone profile retrieval from GOMOS limb scattering measurements, *J. Geophys. Res.*, 113(D23), D23307, doi:10.1029/2007JD009409, 2008.

Taha, G., Rault, D. F., Loughman, R. P., Bourassa, A. E., and von Savigny, C.: SCIAMACHY stratospheric aerosol extinction profile retrieval using the OMPS/LP algorithm, *Atmos. Meas. Tech.*, 4(3), 547–556, doi:10.5194/amt-4-547-2011, 2011.

Thomason, L. W. and Taha, G.: SAGE III aerosol extinction measurements: Initial results, *Geophys. Res. Lett.*, 30(12), 1631, doi:10.1029/2003GL017317, 2003.

Thomason, L. W., Peter, T., Carslaw, K. S., Kärcher, B., Notholt, J., Bingemer, H., Hamill, P., Brogniez, C., Deshler, T., Anderson-Sprecher, R., Weisenstein, D., and Bekki, S.: SPARC Assessment of Stratospheric Aerosol Particles, *World Climate Research Programme (WRCP) SPARC Project Report (4)*, pp. 1–320, 2006.

Thornton, D. C., Bandy, A. R., Blomquist, B. W., Driedger, A. R., and Wade, T. P.: Sulfur dioxide distribution over the Pacific Ocean 1991–1996, *J. Geophys. Res.*, 104(D5), 5845–5854, doi:10.1029/1998JD100048, 1999.

Trepte, C. R. and Hitchman, M. H.: Tropical stratospheric circulation deduced from satellite aerosol data, *Nature*, 355(6361), 626–628, doi:10.1038/355626a0, 1992.

Turco, R. P., Hamill, P., Toon, O. B., Whitten, R. C., and Kiang, C. S.: A One-Dimensional Model Describing Aerosol Formation and Evolution in the Stratosphere: I. Physical Processes and Mathematical Analogs, *J. Atmos. Sci.*, 36(4), 699–717, doi:10.1175/1520-0469(1979)036<0699:AODMDA>2.0.CO;2, 1979.

Valero, F. P. J. and Pilewskie, P.: Latitudinal survey of spectral optical depths of the Pinatubo volcanic cloud-derived particle sizes, columnar mass loadings, and effects on planetary albedo, *Geophys. Res. Lett.*, 19(2), 163–166, doi:10.1029/92GL00074, 1992.

Vanhellemont, F., Fussen, D., Bingen, C., Kyrölä, E., Tamminen, J., Sofieva, V., Hassinen, S., Verronen, P., Seppälä, A., Bertaux, J. L., Hauchecorne, A., Dalaudier, F., Fanton d'Andon, O., Barrot, G., Mangin, A., Theodore, B., Guirlet, M., Renard, J. B., Fraisse, R., Snoeij, P., Koopman, R., and Saavedra, L.: A 2003 stratospheric aerosol extinction and PSC climatology from GOMOS measurements on Envisat, *Atmos. Chem. Phys.*, 5(9), 2413–2417, doi:10.5194/acp-5-2413-2005, 2005.

Vernier, J. P., Pommereau, J. P., Garnier, A., Pelon, J., Larsen, N., Nielsen, J., Christensen, T., Cairo, F., Thomason, L. W., Leblanc, T., and McDermid, I. S.: Tropical stratospheric aerosol layer from CALIPSO lidar observations, *J. Geophys. Res.*, 114, 1–12, doi:10.1029/2009JD011946, 2009.

Vernier, J.-P., Thomason, L. W., Pommereau, J.-P., Bourassa, A. E., Pelon, J., Garnier, A., Hauchecorne, A., Blanot, L., Trepte, C., Degenstein, D., and Vargas, F.: Major influence of tropical volcanic eruptions on the stratospheric aerosol layer during the last decade, *Geophys. Res. Lett.*, 38(12), L12807, doi:10.1029/2011GL047563, 2011.

von Savigny, C.: Stratospheric ozone profiles retrieved from limb scattered sunlight radiance spectra measured by the OSIRIS instrument on the Odin satellite, *Geophys. Res. Lett.*, 30(14), 4–7, doi:10.1029/2002GL016401, 2003.

von Savigny, C., Kaiser, J. W., Bovensmann, H., Burrows, J. P., McDermid, I. S., and Leblanc, T.: Spatial and temporal characterization of SCIAMACHY limb pointing errors during the first three years of the mission, *Atmos. Chem. Phys.*, 5(10), 2593–2602, doi:10.5194/acp-5-2593-2005, 2005.

von Savigny, C., Bovensmann, H., Bramstedt, K., Dikty, S., Ebojie, F., Jones, A., Noël, S., Rozanov, A., and Sinnhuber, B.-M.: Indications for long-term trends and seasonal variations in the SCIAMACHY Level 1 version 6.03 tangent height information, *SCIAMACHY technical note, TN-IUP-scia-pointing-2009-01*, 2009.

Weisenstein, D. and Bekki, S.: Modeling of stratospheric aerosols, in Thomason, L. and Peter, T., eds., *SPARC assessment of stratospheric aerosol properties, WCRP-124, WMO/TD-No. 1295, SPARC Report No. 4*, chapter 6, 2006.

Winker, D. M., Hunt, W. H., and McGill, M. J.: Initial performance assessment of CALIOP, *Geophys. Res. Lett.*, 34(19), L19803, doi:10.1029/2007GL030135, 2007.

Wiscombe, W. J.: Improved Mie scattering algorithms, *Appl. Opt.*, 19(9), 1505–1509, doi:10.1364/AO.19.001505, 1980.

Yang, K., Liu, X., Bhartia, P. K., Krotkov, N. A., Carn, S. A., Hughes, E. J., Krueger, A. J., Spurr, R. J. D., and Trahan, S. G.: Direct retrieval of sulfur dioxide amount and altitude from spaceborne hyperspectral UV measurements: Theory and application, *J. Geophys. Res.*, 115, D00L09, doi:10.1029/2010JD013982, 2010.

Yue, G. K. and Deepak, A.: Latitudinal and altitudinal variation of size distribution of stratospheric aerosols inferred from SAGE aerosol extinction coefficient measurements at two wavelengths, *Geophys. Res. Lett.*, 11(10), 999–1002, doi:10.1029/GL011i010p00999, 1984.

Yue, G. K., Poole, L. R., Wang, P.-H., and Chiou, E. W.: Stratospheric aerosol acidity, density, and refractive index deduced from SAGE II and NMC temperature data, *J. Geophys. Res.*, 99(D2), 3727–3738, doi:10.1029/93JD02989, 1994.

Acknowledgements

This research could not have been undertaken and this thesis not completed without the support of many. I would like to thank the following people and institutions for their help and contributions.

First and foremost, I thank Christian von Savigny for his continuous support, feedback and encouragement during the last few years that made sure that I stayed on the right track with this thesis. Thank you for the numerous discussions that led to considerable improvements of my work. I truly appreciate that your support did not cease after you became professor on the other side of the country and had a lot of other stuff on your mind.

Professor John Burrows gave me the opportunity to work in his group and encouraged and motivated me on countless occasions, for which I am deeply grateful.

I would like to thank Professor Otto Schrems for dedicating his time to be second reviewer of this thesis.

Furthermore, I thank Alexei Rozanov for all kinds of technical and non-technical expertise and support. He and Valdimir Rozanov helped me a lot to gain insight into the world of SCIATRAN and the high art of inverse retrieval methods.

Thanks also to the NASA Langley Research Center (NASA-LaRC) and the NASA Langley Radiation and Aerosols Branch for providing the SAGE II data. I am also indebted to the European Space Agency (ESA) for providing the SCIAMACHY Level 1 data used in this thesis.

I would like to acknowledge the financial support from the ESA, the Deutsche Zentrum für Luft- und Raumfahrt (DLR), and the University of Bremen. For financial support for conference participation, I am additionally thankful to the Postgraduate International Physics Programme (PIP) and the European Geosciences Union (EGU).

Thanks to Kai-Uwe Eichmann for providing the cloud data and many useful tools.

I am thankful to Petra Horn, Anja Gatzka, Birgit Teuchert, Heiko Schellhorn and Heiko Schröter for their help in the jungle of administration and IT support.

Special thanks to Lena Brinkhoff, my companion on the long and stony road to a SCIAMACHY aerosol data set, for many serious and cheerful discussions on stratospheric aerosols and less important things.

Many thanks to the members of the limb group for fruitful discussions on aerosols and more in and outside the limb meeting and to the colleagues of the 4th floor and elsewhere, especially to my office mates Ralf Bauer and Felix Ebojie, who were always good for a relaxing chat in between and helped me to find scientific answers. For manyfold pleasant activities in and outside the IUP I would like to address many thanks to Thomas Krings, Max Reuter, Nabiz Rahpoe, Oliver Schneising, Katja Weigel, Kai-Uwe Eichmann, Lena Brinkhoff, Jens Heymann, Sebastian Dikty and Anja Schönhardt.

Vielen Dank an meine Familie und meine Freunde für den Rückhalt und die Ablenkung, die oft genug dringend notwendig waren und viel beigetragen haben zum Gelingen dieser Arbeit.

Finally, I especially thank Antje for her moral support and her patience, for cheering me up and providing motivation and distraction particularly during the stressful final stages of my PhD project.